SENSITIVITY OF THE LATE PERMIAN CLIMATE TO TECTONIC AND RADIATIVE FORCING CHANGES: IMPLICATIONS FOR THE MASS EXTINCTION

by

ANGELA P OSEN

Presented to the Faculty of the Graduate School of

The University of Texas at Arlington in Partial Fulfillment

of the Requirements

for the Degree of

DOCTOR OF PHILOSOPHY

THE UNIVERSITY OF TEXAS AT ARLINGTON

December 2014

Acknowledgements

I would like to acknowledge that all model simulations were done on NCAR computers, which are supported by the National Science Foundation. This research has been supported by NSF grant EAR #0745817, LSAMP Bridge to the Doctorate program NSF grant #HRD-1026806, NSF STEM support, and a UTA graduate dissertation fellowship.

On a more personal note, I would like to thank my family and friends who have helped me throughout my graduate career. In particular, I would like to thank my parents, Pat and Margie Kline, for their moral support and encouragement over the years. I would also like to thank Lisa Moran for her help and advice over these very long academic semesters, and who has managed to keep me on course. I would also like to extend a special thanks to my sons, Jake, Tanner, and Peyton, for their continuous support and belief in me throughout my time at the University of Texas at Arlington. Most of all, I would like to express my deepest heartfelt gratitude to my husband, Tom, who has supported and encouraged me throughout my personal and academic growth.

The completion of my degree could not have been possible without the support of the wonderful professors within the Earth and Environmental Science Department. I wish to extend a very grateful thanks to my committee members (past and present) Jorge Rodrigues, Chris Scotese, Galina Nestell, Merlynd Nestell, Harry Rowe, Cornelia Winguth, and an especially appreciative thanks to my Ph.D. advisor Arne Winguth, for giving me the opportunity, the support, and guidance to achieve my goals.

November 24, 2014

Abstract

SENSITIVITY OF THE LATE PERMIAN CLIMATE TO TECTONIC AND RADIATIVE FORCING CHANGES: IMPLICATIONS FOR THE MASS EXTINCTION

Angela Osen, PhD

The University of Texas at Arlington, 2014

Supervising Professor: Arne Winguth

The largest mass extinction occurred near the Permian-Triassic boundary (ca. 252 Ma). Significant carbon isotope shifts indicate that perturbations in the carbon cycle occurred during the Late Permian and persisted into the Early Triassic. The loss of biodiversity within the terrestrial and marine realms coincided with the eruption of the Siberian Flood Basalts and magma intrusion into coal beds, leading to the emission of greenhouse, sulfur, and other gases into the atmosphere.

In this study, climate model output from the Community Climate System Model Version 3 with improved topographic features, along with a prediction of patterns of oceanic water masses and terrestrial biomes is compared with climate-sensitive sediments and phytogeographic reconstructions. Incorporating these features into the model will help to better understand the environmental changes that may have led to the mass extinction.

The possible effects of a mid-ocean ridge and sills between the Paleo-Tethys and Panthalassa on water mass distribution and oxygen content have been investigated. Model results suggested that a mid-ocean ridge would not likely alter the global

distribution of water masses; however, the introduction of sills could lead to enhanced stratification in the Paleo-Tethys.

The response of climate-sensitive sediments and biomes to a carbon pulse of 4872 PgC into the atmosphere has been assessed to better understand the environmental changes that occurred during the Late Permian-Early Triassic transition. The analysis of climate simulations implied a poleward expansion of the Panthalassic temperate and tropical regions along with a transition of polar to temperate water masses. On the supercontinent of Pangea, an expansion of deserts within the inner continent is inferred. Extreme temperature increases coupled with changing precipitation patterns likely contributed to the mass extinction of much of the fauna and flora as suggested by the modeling results and phytogeographic patterns.

Table of Contents

List of Illustrations

List of Tables

Chapter 1

Introduction

1.1 The Permian-Triassic extinction

Near the Permian-Triassic boundary (PTB, 252.2 ± 0.5 Ma), the largest known mass extinction of the Phanerozoic occurred when more than 90% of marine and 70% of the terrestrial species became extinct (Erwin, 1994; Erwin, 2006; Retallack, 1995). Wide varieties of kill mechanisms have been proposed, but a consensus for any one particular mechanism has not been reached. The putative causes for the extensive biotic crisis include: (1) large-scale volcanic activity that generated the Siberian Traps (Renne and Basu, 1991; Campbell et al., 1992; Renne et al., 1995; Reichow et al., 2002; Kamo et al., 2003; Isozaki, 1997; Svensen et al., 2009), (2) copious anoxia events (Wignall and Hallam, 1992; Kajiwara, 1994; Isozaki, 1997; Wignall and Twitchett, 1996; Kato et al., 2002; Kidder and Worsley, 2004; Grice et al., 2005; Kump et al., 2005; Riccardi et al., 2006), (3) bolide impact (Basu et al., 2003; Becker et al., 2004), and (4) greenhouse gas emissions from the outgassing of the Siberian Traps (Wignall, 2001; Kidder and Worsley, 2004; Royer, 2006; Reichow et al., 2009; Svensen et al., 2009; Breecker et al., 2010), triggering global climate change (Kidder and Worsley, 2012; Algeo et al., 2011; Retallack et al., 2011). Besides the large change in biodiversity, additional evidence of a severe disruption in climate included the discovery of several forms of disaster taxa such as microbial mats (Baud et al., 1997; Payne et al., 2007; Castle, 2009; Yang et al., 2011) and small-sized molluscan fauna (Schubert and Bottjer, 1995; Fraiser, 2011), which flourished during the earliest Triassic. The Lilliput effect, defined by Urbanek (1993) as a quantifiable yet temporary decrease in the size of surviving species in the immediate aftermath of an extinction (Fraiser et al., 2011), was present in the earliest Triassic

benthic groups (Twitchett, 2007). Recovery from the mass extinction event was slow, taking until the Middle Triassic (~ 6 m.y.) for marine biota to rebound (Twitchett, 1999; Payne et al., 2006).

1.2 The Permian-Triassic boundary

Determination of the exact Permian-Triassic boundary has been contentious, as correlation of stratigraphic sections from one region to another has been challenging. Correlations of marine shelf facies with deep marine and with terrestrial facies are still uncertain. The International Union of Geological Sciences (IUGS) has ratified the Global Stratotype Section and Point (GSSP) of the Permian-Triassic Boundary (PTB) as being located at the *Hindeodus parvus* horizon at the base of Bed 27c of Meishan Section D, Changxing County, Zhejiang Province, South China (Yin et al., 2001; Yin et al., 2005). *Hindeodus parvus* is considered an exceptional index marker, as it is not facies-related or latitude-restricted. *H. parvus*, though generally considered to be a shallow-water conodont, has been discovered in both shallow water and pelagic deposits (Kozur, 1996; Lai, 1998; Yin et al., 2001). The temporal uncertainty of the first appearance of this organism has led to potential errors on the cause of the mass-extinction. Furthermore, usage of a marine organism does not assist with the establishment of terrestrial boundaries.

In recent years, it has been suggested that geochemical analysis regarding stable carbon isotopes in marine and non-marine records might serve as a viable alternative for correlating the Permian-Triassic boundary. Carbon isotope studies (Wang et al., 1994; Payne et al., 2007; Horacek et al., 2010; Korte and Kozur, 2010; Wang et al., 2012) demonstrate that a large negative shift in the stable carbon isotopes occurs within marine and non-marine records associated with the PTB. Global carbon-isotope

fluctuations would be reflected in marine carbonates and marine phytoplankton because they are derived from the same carbon pool of dissolved inorganic carbon (Korte and Kozur, 2010). Plants prefer the lighter isotopic carbon (^{12}C) to ^{13}C and therefore, the carbon-isotopic composition of organic matter is strongly depleted. The reported durations and amplitudes as well as the exact stratigraphic positions of $\delta^{13}C$ peaks are somewhat variable (declines of 2-7‰ for marine and as much as 24‰ for continental environments); however, they are recorded in a wide range of marine and terrestrial deposits (Korte and Kozur, 2010). The initial onset of the negative carbon anomaly predates the onset of the extinction event (Twitchett et al., 2001) by approximately 500,000 years (Korte and Kozur, 2010) and can therefore not be used as a definitive marker but can be useful for the correlation of stratigraphic units.

1.3 Possible causes of the Permian-Triassic extinction

Many hypotheses have been proposed to explain the Permian-Triassic extinction, but the exact triggering mechanisms are still controversial. One commonly discussed hypothesis is that outgassing from the Siberian Traps and associated greenhouse gas emissions (Wignall, 2001; Kidder and Worsley, 2004; Royer, 2006; Reichow et al., 2009; Svensen et al., 2009; Breecker et al., 2010) triggered a global climate change (Kidder and Worsley, 2012; Algeo et al., 2011; Retallack et al., 2011). One plausible consequence of CO_2-induced global warming is the possibility of enhanced ocean stratification that can lead to widespread hypercapnia and anoxia (Knoll et al., 1996; Clapham and Payne, 2011). The large emission of greenhouse gases into the atmosphere could also induce climatic changes such as extreme precipitation events, particularly in the polar and subtropical regions, and increased subtropical aridity within the interior of the continents causing a global shift in floral and faunal patterns (Solomon

et al., 2007; National Research Council, 2011). Additionally, anoxic conditions present in shelf environments may have stimulated the growth of sulfur-reducing bacteria, which in turn, may have dramatically increased the presence of sulfidic-rich deeper waters (Kump et al., 2005; Knoll et al., 2007). With the large continental mass of Pangea and no evidence of continental ice sheets during the latest Permian, it is hypothesized that weak ocean circulation patterns might have developed that would have been unable to supply enough oxygen to the deep sea in order to maintain oxic environments throughout the oceans (Knoll et al., 1996). Whereas deep-sea anoxia has been inferred from pelagic sediments originating from the Panthalassa Ocean (Isozaki, 1997), modeling and recent geochemical studies indicate that dysoxic to anoxic conditions occurred in the shallow marine areas and that there was an expanded oxygen minimum zone potentially due to increased nutrient inventories (Winguth and Maier-Reimer, 2005; Meyer et al., 2008; Algeo et al., 2010; Winguth and Winguth, 2012; Winguth et al., 2012). Geochemical data supports the existence of suboxic to anoxic water masses in the Tethys Ocean near the PTB (Newton et al., 2004; Grice et al., 2005; Cao, 2009).

The PTB extinction may have been triggered by a bolide impact (Basu et al., 2003; Becker et al., 2004) that could, together with massive volcanism, have contributed to an increased influx of isotopically light sulfur into the atmosphere (Kaiho et al., 2001). The possible location of such a large impact is still controversial. Becker et al. (2004) suggest that an impact crater may have been located between Australia and Antarctica and may have served as a trigger for the massive release of material from the Siberian Traps mantle plume. Another possibility is the Araguainha impact crater located in Brazil, which was recently dated by Tohver et al. (2012) as having been generated near the PTB. Although the Araguainha structure in the Paraná is estimated to be 40 km in

diameter, it is too small to likely be the sole cause of the extinction event but certainly could have contributed to local extinctions.

Despite the uncertainties of the exact triggering mechanism of the Permian-Triassic extinction, global warming has emerged as a common theme to many of the hypotheses. Extreme hot temperatures in the ocean and on land could not only have led to the extinction of many species but may also have impeded the recovery from such a large extinction event. Oxygen isotopic evidence suggests rapid warming of Late Permian seawater from 21ºC to 36ºC in less than 1 million years (Sun et al., 2012; Joachimski et al., 2012). Sea surface temperatures (SSTs) may have exceeded 40ºC by the Early Triassic (Sun et al., 2012). The lack of polar ice with accompanying warmer ocean temperatures likely resulted in the weakening of the thermal mode of circulation (Hotinski et al., 2001; Zhang et al., 2001; Kidder and Worsley, 2004) contributing to anoxic and euxinic conditions that are documented in the geological record. Warming would have increased the frequency and intensity of tropical cyclones, which with warmer deep waters, may have traveled into the higher paleolatitudes (Kidder and Worsley, 2004). Topography and bathymetry can influence circulation patterns within the atmosphere and oceans, thereby influencing climatic conditions on a regional and sometimes global scale. In this study, a fully coupled comprehensive climate model is used to evaluate climatic changes that transpired during the Late Permian and into the Early Triassic.

Chapter 2

Objectives

The overall purpose of this climate modeling study is to investigate the environmental changes in response to topographic and radiative forcing perturbations at the PTB. The results will help assess the relationships between the forced boundary conditions and climate change as inferred from the geologic record that may have contributed to the mass extinction. The research could also serve as an analogue for future climate change because of the massive carbon emissions to the atmosphere at the PTB (Payne et al., 2004; Joachimski et al., 2012; Sun et al., 2012) likely exceeding the expected release of fossil fuel of 5000 PgC by 2400 (Caldeira and Wicket, 2003). More specifically, the following questions are addressed with the use of comprehensive climate models and climate proxies from the Late Permian and into the Early Triassic.

- Could a mid-ocean ridge significantly alter water mass distribution and contribute to the decline in dissolved oxygen concentrations?

Mid-ocean ridges (MORs) can redirect flow via topographic steering, as well as act as barriers on deep oceanic currents (Gille et al., 2004; Katsman, 2006; Thurnherr et al., 2011). The presence of a ridge disrupts the normal deep-water flow resulting in internal waves that can lead to diapycnal mixing. Additional mixing can lead to horizontal density gradients, which can drive secondary flows (Thurnherr et al., 2011). Blockage of deep ocean basins may cause dense bottom waters to be redirected into downstream basins, leading to stratification (Thurnherr et al., 2011). Restriction of ocean circulation could conceivably alter the distribution of salinity, dissolved oxygen, as well as alter other geochemical aspects of the ocean water masses. Recent model simulations performed by Montenegro et al. (2011), which included possible mid-ocean ridge configurations for

the time near the PTB, suggested that an increase in meridional overturning circulation could have occurred due to the presence of MORs. Changes of bathymetry may have increased biological productivity due to additional mixing and upwelling of water masses.

- Would sills restricting flow between the Paleo-Tethys and the Panthalassa Oceans contribute to the onset of anoxic conditions that are indicated in the geological record?

Previous model simulations of the Late Permian have been performed with deep (> 3000 m) open passageways between the Tethys and Panthalassa Oceans that are capable of deep-water exchange (Kutzbach et al., 1990; Kutzbach and Ziegler, 1993; Hotinski et al., 2001; Zhang et al., 2001; Ziegler et al., 2003; Kiehl and Shields, 2005; Montenegro et al., 2011; Roscher et al., 2011). However, there is no consensus on the extent of the oceanic passageway between the North and South China blocks during the Late Permian (see section 4.1 for additional details). Knoll (1996) hypothesized that anoxia would develop within narrow ocean basins with the decrease of ocean circulation. Present-day examples of this phenomenon include the Cariaco Basin and the Black Sea. The Cariaco Basin, located off the northern coast of Venezuela, reaches a maximum depth of approximately 1400 m and is isolated as a result of a shallow sill (Li et al., 2008). Only the top 90-150 m of water from the Caribbean can enter the Cariaco Basin. Nutrient trapping in silled basins can lead to a loss of dissolved oxygen due to decomposition. Estuarine circulation can develop in stratified silled basins, such as the present-day Black Sea, which could increase biological productivity, thus increasing the oxygen demand in deeper waters.

- Are changes in climate zones, as inferred from climate-sensitive sediments, consistent to the rise in temperature as inferred from proxies across the PTB and are

the changes in agreement with the rise in the surface temperatures as inferred from stable oxygen isotopes and climate modeling?

Climate-sensitive sediments reveal the long-term trends in paleoclimatic conditions, which can assist with interpretation, and are often used in collaboration with modeling studies (Ziegler et al., 1998; Gibbs et al., 2002; Winguth et al., 2002). Climate-sensitive lithotypes have been used to reconstruct paleoclimatic conditions for past environments, as their distribution tends to occur along a narrow range of climatic settings on modern Earth (Ziegler et al., 1987; Ziegler et al., 2003; Tabor and Poulsen, 2008). The lithological markers can assist in identifying oceanic water mass distributions. Moreover, by modeling water masses, the location of economically relevant deposits such as halite, gypsum, phosphorites and oil source rocks can possibly be identified. Examples of climate-sensitive sediments used in past modeling studies as well as in this study include: carbonate buildups, coals, evaporites, eolian sands, oil source rocks and phosphorites. Lithological markers such as those previously listed suggest the Middle to Late Permian was a transitional time from a greenhouse into a hothouse climate. By using increased atmospheric CO_2 concentrations in the model to amplify surface temperatures, it is expected that the simulated climate zones would be in general agreement with climate-sensitive sediments found in the geological record. Conversely, the temperatures predicted by the model should be in relative agreement with temperature estimates determined by $\delta^{18}O$ isotope analysis.

- Were the global phytogeographic patterns significantly altered across the PTB due to the rise in temperatures caused by the increase in greenhouse gases?

Paleobotanical data can provide a means of interpreting terrestrial paleoclimate. Following an approach used by Rees et al. (1999; 2002), by integrating information on leaf morphologies with patterns of climate-sensitive sediment distributions, a series of

regional biomes can be reproduced, revealing information about climate gradations. The general description of a biome is a region that has similar climatic conditions and contains ecosystems of similar plants, animals, and other organisms. Walter (1985; 2002) defined a biome as a habitat that corresponds to a concrete uniform landscape. As global climate changes, biome zones should also correspond to the fluctuation in temperature and precipitation. Biomes, utilized for this research and previously defined by Walter (1985; 2002), are highly idealized and categorized into nine distinct zones. These nine zones are large, climatically similar environments that share similar rainfall and temperature characteristics. Precipitation is divided into three main categories based on annual averages: desert (< 250 mm yr^{-1}), temperate (250-2000 mm yr^{-1}), and tropical (> 2000 mm yr^{-1}), with temperature variations added to further divide the biomes (Walter and Breckle, 2002).

During the Permian period, lithological proxies indicate that the climate transitioned from an icehouse world to ice-free seas by the Middle Permian and continued to warm, culminating in hothouse conditions by the Early Triassic. Though the supercontinent had moved in a northward direction during this period, the drift of Pangea was not enough to account for the dramatic shift in climatic patterns. Using lithological proxies, paleobotanical evidence, and modeling parameters tied to temperature and precipitation rates, the model experiments should reflect a change in biomes corresponding to the shift in the paleobotanical patterns.

Overall, this study will give new insights as to how a transition into a hothouse climate may have affected the biogeochemical cycles and how the resulting environmental changes may have contributed to the mass extinction that occurred at the PTB.

Chapter 3

Climate System Model and Boundary Conditions

3.1 Model description: The Community Climate System Model version 3

A fully coupled comprehensive climate system model, the Community Climate System Model (CCSM3, Collins et al., 2006; http://www.cesm.ucar.edu/models/ccsm3.0/) was applied for the climate sensitivity experiments described in the following chapters. The CCSM3 contains four important components of the climate system (atmosphere, land, ocean, and sea-ice). Physical and geochemical fluxes, boundary conditions, and physical state information are exchanged between the different geophysical models and are linked by a coupler. Certain physical constants are shared by all of the components in the coupled modeling system and are presented in Appendix B.

The low-resolution T31_gx3v5 was used for the paleoclimate sensitivity experiments performed and described in the following chapters. The atmosphere and land models share an identical horizontal Gaussian grid with a truncation level in the spectral space of T31 (approximately 3.75 degree resolution) whereas the ocean and ice models similarly use the same nominal grid (gx3v5) with a North Pole and South Pole displacement to Pangea. The nominal gx3v5 grid features a longitudinal resolution of 3.6 degrees and a variable latitudinal resolution (approximately 0.9 degrees near the equator). The gx3v5 grid has 100 longitudes and 116 latitudes of horizontal grid cells.

CCSM3 utilizes primitive equations consisting of the conservation of momentum, vorticity, thermal energy, and continuity equations. The conservation of momentum consists of a form of the Navier-Stokes equations that describe hydrodynamical flow on the surface of a sphere. The thermal energy equation conveys the overall temperature of

the system to heat sources and sinks whereas the continuity equation is necessary for the conservation of mass. Brief descriptions of each of the four main components are summarized in the subsections below.

3.1.1 The Community Atmosphere Model

The atmospheric component, the Community Atmosphere Model version 3 (CAM 3), is the fifth generation of The National Center for Atmospheric Research's global three-dimensional atmospheric general circulation model (AGCM; Collins et al., 2006) with Eulerian spectral dynamics. Major improvements of the CAM 3.0 compared to the earlier version CAM 2 included new physics and dynamics. Examples include: a finite-volume dynamical core (Lin and Rood, 1996; Lin, 2004), new treatment of cloud and precipitation processes (Boville et al., 2006), new radiative parameterization including interactions of long- and short-wave radiation with cloud geometry and with water vapor (Collins et al., 2004), new aerosol data sets for detailed information about CAM 3.0, and new calculation of thermodynamic tendencies to insure conservation of energy (Boville and Bretherton, 2003).

The atmospheric model derives the primitive equations in a generalized terrain-following vertical coordinate (Collins et al., 2004). The total parameterization package is coupled into a semi-implicit Eulerian spectral transform dynamical core and consists of moist precipitation processes, clouds and radiation, a surface model, and turbulent mixing (Collins et al., 2004). The precipitation processes consist of dry adiabatic adjustment for the stratosphere, moist penetrative convection, shallow convection and large-scale stable condensation. This cloud parameterization is utilized for the radiation parameterization. Water vapor is considered a prognostic variable with new parameterizations for longwave absorptivity and emissivity that preserves the formulation

of the radiative transfer equation using the absorptivity/emissivity method (Collins et al., 2004). The surface model provides the surface fluxes obtained from the land, ocean and sea-ice models. The surface fluxes require the lower flux boundary conditions that consist of the planetary boundary layer parameterization, vertical diffusion, and gravity wave drag (Collins et al., 2004). The deep convection parameterization scheme was developed by Zhang and McFarlane (1995) and is based on a plume ensemble approach that convective scale updrafts and their associated saturated downdrafts may exist whenever the atmosphere is conditionally unstable within the lower troposphere. Original formulas can be found in Zhang and McFarlane (1995) whereas a summary of the formulation used in CAM3.0 can be found in chapter 4 of the CAM3.0 User's Guide (Collins et al., 2004) and at http://www.cesm.ucar.edu/models/ atm-cam/.

3.1.2 The Community Land Model

The Community Land Model version 3 consists of biogeophysical processes forced by atmospheric surface fluxes that in turn provide surface albedos, upward longwave radiation, sensible heat flux, latent heat flux, water vapor flux, as well as zonal and meridional surface stresses to the atmospheric model (Oleson et al., 2004). The aforementioned processes are partially regulated by several ecological and hydrological factors. The model can simulate processes such as leaf phenology as well as stomatal physiology, and can account for ecological differences among vegetation types. Hydrological and thermal differences in soil types are considered, which allows for multiple land cover types within a gird cell (Oleson et al., 2004).

The current state of the atmosphere (Appendix C) at a given time step is used to force the land model, which is provided by the atmospheric model when it is in coupled mode (Oleson et al., 2004). The CLM3.0 will calculate surface energy, constituent,

momentum and radiative fluxes using the snow and soil hydrologic states from the previous time step (Oleson et al., 2004). These fields are then given to the atmospheric model via the coupler. Detailed information regarding ecosystem composition and structure, surface albedos, radiative fluxes, momentum, sensible heat, latent heat fluxes, soil and snow temperatures, as well as hydrology can be found in Oleson et al. (2004; http://www.cgd.ucar.edu/tss/clm/distribution/clm3.0/).

3.1.3 The Parallel Ocean Program

The ocean component consists of the Parallel Ocean Program version 1.4.3 (POP), a level-coordinate ocean general circulation model, in which three-dimensional primitive equations for ocean dynamics and a dipole grid with a nominal horizontal resolution of ~3° and 25 vertical levels are used (Smith and Gent, 2004; Collins et al., 2006). The POP model is a descendant of the Bryan-Cox-Semtner models (Semtner, 1986), which has been improved by the Los Alamos National Laboratory (LANL) and NCAR (Smith and Gent, 2004). Detailed information on POP is documented in Collins et al. (2006), equations used can be reviewed in Smith and Gent (2004), and additional material can be obtained through http://www.cesm.ucar.edu/models/ccsm3.0/pop/.

The ocean dynamics used in the POP model are described by the 3-D primitive equations for a thin stratified fluid in spherical polar coordinates using hydrostatic and Boussinesq approximations (Smith and Gent, 2004) and are listed in Appendix D.

The passive tracer is defined as a tracer that does not impact the physical solution, yet it is carried along with the flow with some internal transformation that does not feed back into the prognostic tracer and/or variable (Smith et al., 2010). The ideal age passive tracer is used to estimate the ventilation timescales within the ocean (Thiele and Sarmiento, 1990; England, 1995; Smith et al., 2010) or more specifically, the time (years)

since a parcel of water has been transported away from the surface (Bryan et al., 2006; Kiehl, 2007). The ideal age passive tracer is suitable for the same tracer transport equation as potential temperature and salinity, (see equation 1.11 in Appendix C), but requires that the surface boundary conditions be set to zero with each time step (Smith et al., 2010).

The grid is a displaced-pole grid with approximately a 3.6º (gx3v5) horizontal resolution (Vertenstein et al., 2004). The poles are displaced over land using a dipole mesh grid. The vertical dimension is considered using a depth coordinate (z) with the levels extending to 4.75 km (Collins et al., 2006). The depths of each of the 25 levels vary in order to limit computational costs, yet are able to enhance the upper ocean resolutions; for example, the top layer is 8 m thick whereas the lowest layer is >300 m. No significant losses have been attributed to the increased vertical spacing below 300 m when the model was tested (Yeager et al., 2006).

3.1.4 The Community Sea Ice Model

For the sea-ice component, the Community Sea Ice Model version 5 (CSIM5; was used with the same horizontal and vertical resolution as the ocean general circulation model (POP v. 1.4.3). The CSIM is a dynamic-thermodynamic model that includes a subgrid-scale ice thickness distribution (Schramm et al., 2004) and uses the energy conserving thermodynamics of Bitz and Lipscomb (1999). The model features ice dynamics as well as sea-ice albedo and exchanges of salt between sea-ice and the surrounding ocean (Collins et al., 2006). Detailed information about the CSIM can be found in Briegleb et al. and Schramm et al. (2004) as well as at http://www.cesm.ucar.edu/models/ccsm3.0/csim/.

3.1.5 Ocean carbon cycle

The carbon component of the coupled marine climate-carbon cycle model is based on the Ocean Carbon-cycle Model Intercomparison Project (Najjar and Orr, 1999; Doney et al., 2006; Winguth and Winguth, 2012). The discrete transports of tracers through the ocean are determined by equations given by Smith and Gent (2004):

$$\frac{\partial}{\partial t}(1 + \xi)\varphi + \mathcal{L}_T(\varphi) = D_H(\varphi) + D_V(\varphi) + F_W(\varphi) + F_B(\varphi), \quad (3.1)$$

where φ is the concentration of the tracer. The tracer concentration is associated with changes in volume in the surface layer $(1 + \xi)$ due to undulations and ξ is given by

$$\xi = \frac{\delta k_1}{dz_1}\eta \quad , \quad (3.2)$$

where δk_1 is the Kronecker delta, equal to 1 for k = 1 and zero otherwise. η is the displacement of the free surface relative to $z = 0$ (Smith and Gent, 2004). $\mathcal{L}_T$ is the advection operator, $\mathcal{D}_H$ is the horizontal diffusion operator, $\mathcal{D}_V$ is the vertical diffusion operator, F_w is freshwater flux and F_B is biogeochemical processes (Smith and Gent, 2004; Winguth and Winguth, 2012).

Calculations for the transfer of gases between the ocean and atmosphere occurs as documented by Doney et al. (2006) and included in Winguth and Winguth (2012):

$$\Delta F = F_{ao} - F_{0a} = K_u((pCO_2)_a - \beta_T[CO_2])(1 - f_{ice}) \quad , \quad (3.3)$$

where $F_{ao} - F_{0a}$ is the CO_2 gas flux across the air-sea interface, K_u is the wind-dependent air-sea gas exchange coefficient (Wanninkhof, 1992), $(pCO_2)_a$ is the atmospheric partial pressure of CO_2. β_T is the solubility of CO_2 which is temperature dependent and $[CO_2]$ is the dissolved CO_2 concentration for the surface layer of the ocean where $((pCO_2)_a = \beta_T[CO_2])$. f_{ice} is the fractional sea-ice coverage where the CO_2 gas flux across the sea-air interface must be reduced in the presence of sea ice.

Air–sea fluxes of CO_2 and oxygen were estimated using the wind-dependent gas exchange coefficient across the air-sea interface, along with partial pressures of CO_2 in the lower two layers of the atmosphere and the top layer of the ocean (Doney et al., 2006). The solubility of CO_2 and oxygen is temperature-dependent. The model includes five prognostic variables: inorganic phosphate, semi-labile organic phosphorous, dissolved oxygen, dissolved inorganic carbon, and alkalinity (Doney et al., 2006; Najjar et al., 2007). The parameterization of biological uptake of nutrients and decay of organic material assumes a constant Redfield ratio of C:N:P:O_2 (117:16:1:-170; Anderson and Sarmiento, 1994) for particulate organic matter. Oxygen is linked to phosphorus by the constant of O_2:P = -170 (Anderson and Sarmiento, 1994; Najjar et al., 2007). The uptake of PO_4 is given by the turnover of biomass, modulated by surface solar irradiance, and temperature, with phosphate and iron as the limiting nutrients within the model. Phosphate, generally well correlated to nitrate in the present ocean (Millero, 2006), was chosen as a limiting nutrient to reduce the computational costs associated with the complexities of nitrogen fixation and denitrification (Najjar and Orr, 1998). As export production is phosphorus-based, P is converted to carbon units using the C:P ratio of 117 (Anderson and Sarmiento, 1994; Najjar et al., 2007). The model used a Martin power–law curve (a = − 0.9) to describe the vertical particulate organic phosphorus flux profile over the full water column. The flux is altered by scavenged Fe attached to the sinking matter throughout the water column (Doney et al., 2006).

3.1.6 Radiative forcing and land vegetation

Boundary conditions are similar to Kiehl and Shields (2005) and are summarized in Table 3-1. The solar constant for the Permian-Triassic boundary was adjusted to reflect a fainter sun and was set to 1338 W m^{-2}, representing a 2.12% decrease from the

modern value based upon calculations by Boothroyd (Caldeira and Kasting, 1992; Winguth et al., 2002). Eccentricity and the vernal equinox were set to zero, resulting in near equal receipt of solar insolation for both hemispheres (Gibbs et al., 2002). Earth's obliquity was set to 23.5°, equivalent to the modern value of the Earth's axial tilt. Greenhouse gas concentrations are taken from Kiehl and Shields (2005; see also Table 3-1) and are inferred from Kidder and Worsley (2004). The fixed land vegetation used in the experiments was adapted from the model simulation by Kiehl and Shields (2005) and based on the paleo-vegetation models of Rees et al. (1999).

Table 3-1 Boundary conditions for the Late Permian bathymetric simulations

	CO_2 (ppmv)	CH_4 (ppmv)	N_2O (ppmv)	S0 (Wm^{-2})	Eccentricity	Obliquity
Value	3550	0.700	0.275	1338	0	23.5°

Table adapted from Kiehl and Shields (2005); ppmv is parts per million by volume and S0 is solar insolation.

3.2 Land-sea distribution

Paleogeography and paleotopography for all sensitivity experiments were taken from Kiehl and Shields (2005; provided by D. Rowley, 2005, pers. comm.). As in the Kiehl and Shields (2005) simulation, the average depth of the ocean near the Permian–Triassic boundary is assumed to have been comparable with the mean depth of the present-day oceans and was therefore set to ~4 km. The flat-bottom floor simulation was set up to have a smoothed ocean floor configuration (Figure 3-1A), identical to that in Kiehl and Shields (2005), whereas the bathymetry was modified for the mid-ocean ridge and closed Tethys region experiments (Figure 3-1B and Figure 3-1C) hence referred to as the FB, MOR, and Tethys experiments, respectively.

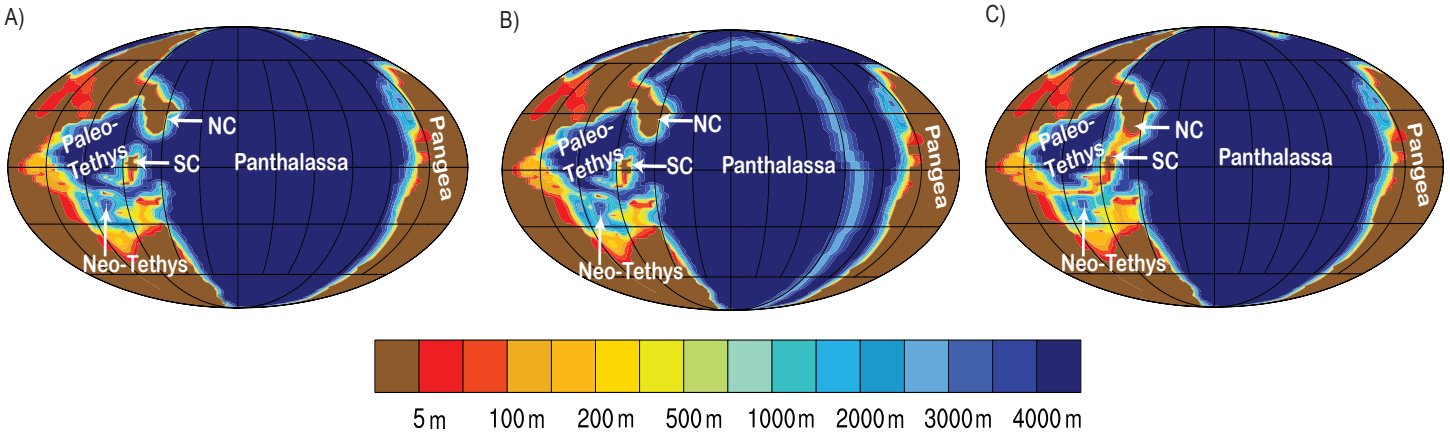

Figure 3-1 CCSM3 Late Permian continental and ocean floor configurations for: A) the flat-bottom floor (FB) experiment, with a flat bottom ocean and partially open exchange between the Panthalassa, Paleo-Tethys and Neo-Tethys oceans. B) The mid-ocean ridge (MOR) experiment, with a mid-ocean ridge located in the Panthalassa. C) The Tethys experiment, with the addition of sills up to a depth of 200 m located in the eastern region of the Paleo-Tethys between the North China Block (NC) and South China (SC) section, including the Yangtze and Hunan blocks, and also in the southern Paleo-Tethys, separating the Paleo-Tethys from the Neo-Tethys Ocean (Osen et al., 2013). Mountain range heights and valley depths are not illustrated in the above figures.

Chapter 4

Bathymetric Sensitivity Experiments

4.1 Introduction to Permian topography and bathymetry

The majority of the continents during the Late Permian/Early Triassic were connected as one supercontinent referred to as Pangea (Smith and Hallam, 1970; Lawver and Scotese, 1987; Lottes and Rowley, 1990; Scotese and Langford, 1995). The formation of Pangea was a result of the collision of two smaller landmasses referred to as Laurasia in the Northern Hemisphere and Gondwana in the Southern Hemisphere. The former continental mass of Laurasia contained what became the present-day regions of North America, Greenland, and Eurasia with Eurasia encompassing the areas of Iberia, Kazakhstania, and the Siberian Platform. Gondwana included what became the present-day expanses of South America, Arabia, Australia, Morocco, Madagascar, India, and Patagonia. Most of Africa, parts of New Zealand, East Antarctica and the Antarctic Peninsula were also part of Gondwana during the Permian. The largest ocean during the Late Permian, named Panthalassa, surrounded the entire supercontinent of Pangea. A smaller ocean known as the Paleo-Tethys separated the main continent of Pangea from a semi-circle of island-like landmasses (Figure 4-1). The eastern section terranes that separated the Paleo-Tethys Ocean from the Panthalassa are often referred to as the Cathaysian terranes and included Tarim, North China, South China and Indochina (Nie et al., 1990). The southern region separating the Paleo-Tethys Ocean from the smaller Neo-Tethys Ocean included the modern-day countries of Afghanistan, Burma, Iran, Malaysia, Tibet, and Turkey, which are collectively referred as the Cimmerian terranes (Şengör and Natal'in, 1996).

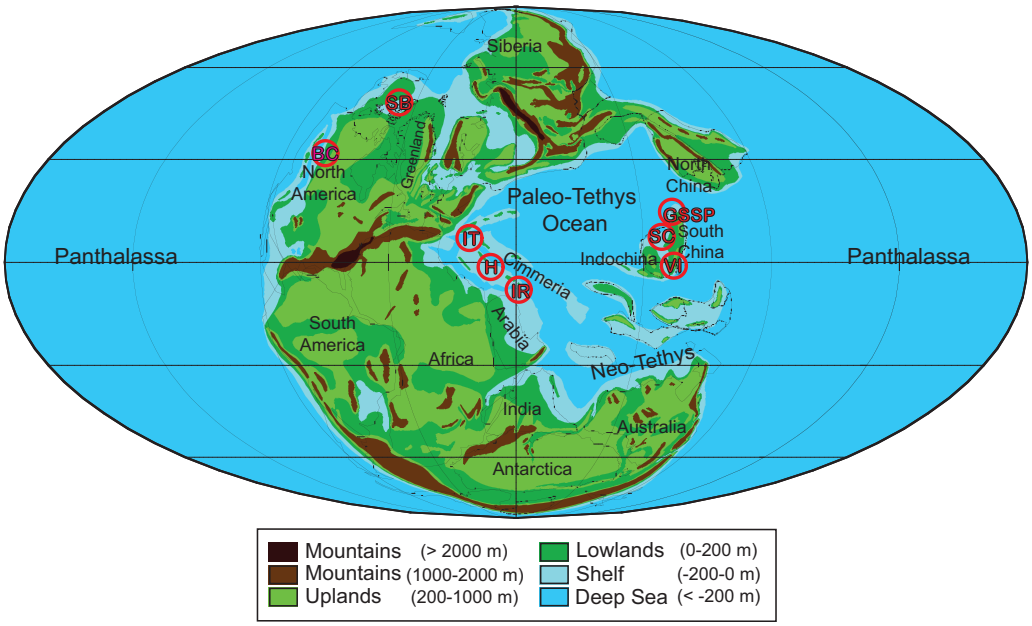

Figure 4-1 The supercontinent of Pangea reconstructed for the Late Permian with present-day country names superimposed onto the supercontinent (Ziegler et al., 1997) . The location abbreviations listed are as follows: Ursula Creek, British Columbia (BC), Meishan, China official Global Boundary Stratotype Section and Point (GSSP) for the PTB, Bálvány, Hungary (H), Jolfa, Iran (IR), Suisi, Northern Italy (IT), Buchanan Lake and West Blind Fiord, Sverdrup Basin, Canada (SB), Shangsi, South China (SC), and Nhi Tao, Northern Vietnam (VI).

Exact movements of the continents prior to the Jurassic (ca. 145-196 Ma) are unresolved because of subduction, deformation, and erosion, and thus have been reconstructed based on preserved structural similarities, paleomagnetic evidence, and sedimentary records, including fossils, and paleoclimate indicators (Erwin, 1993; Şengör and Atayman, 2009). Between the Early Permian (ca. 299 Ma) and Late Permian (ca. 252 Ma), the paleolatitudinal movement of Pangea was estimated to be approximately 15º northward, amounting to about one climate zone (Ziegler et al., 1997; Rees et al.,

2002). For the Late Permian reconstruction, paleogeographic and bathymetric uncertainties still existed in the Tethys region, in particular, the amount of separation between the North China and South China blocks.

Paleomagnetic and geochronological data have been studied by many authors (Lottes and Rowley, 1990; Scotese and Langford, 1995; Zhao et al., 1996; Ziegler et al., 1997; Şengör and Atayman, 2009), yet different paleogeographic interpretations of the Cathaysian and Cimmerian terranes exist in the literature and are presented in Figure 4-1 and Figure 4-2. One such paleo-reconstruction allows exchange between the Paleo-Tethys, Neo-Tethys and Panthalassa oceans by way of small, deep passageways between the North and South China blocks as well as the Cimmerian landmasses. The open Tethys arrangement has been used by Ziegler et al. (1997, 1998; see Figure 4-1) and Rees et al. (1999, 2002) as well as others. Moreover, Meng and Zhang (1999) proposed that a throughway to the Paleo-Tethyan Ocean between the North and South China blocks existed and that subduction in this region may not have occurred until the Early Triassic. In contrast, there are others (Scotese and Langford, 1995; Zhao et al., 1996; Şengör and Atayman, 2009) who suggest that the collision of North and South China began near the end of the Permian, but that these landmasses had not become completely sutured until the Mesozoic. Furthermore, Şengör et al. (1988), Scotese et al. (1995) and Golonka (2007) have suggested the presence of a continental shelf (0-200 m), and Şengör et al. (2009) explored the possibly of a land bridge connection in the region as illustrated in Figure 4-2. The Cathaysian bridge, as it is referred to in Şengör and Atayman (2009), would have included parts of Japan, South China and North China (Şengör and Natal'in, 1996; Şengör and Atayman, 2009). The hypothesis of a Cathaysian land bridge is based upon the presence of Cathaysian flora, foraminiferal fauna (e.g., *Neoschwagerina, Lepidolina*, and *Palaeofusulina*) and the migration of the mammal-like

reptile *Dicynodon*, which was able to travel to Indochina from Gondwana and then to eastern Laurasia (Battail, 1997; Battail, 2000; Şengör and Atayman, 2009). Additionally, the presence of extensive carbonate platforms (Grunt, 1995; Grunt and Shi, 1997; Chumakov and Zharkov, 2003) suggests that the Tethyan continental fragments were already joined by shallow seas by the beginning of the Late Permian.

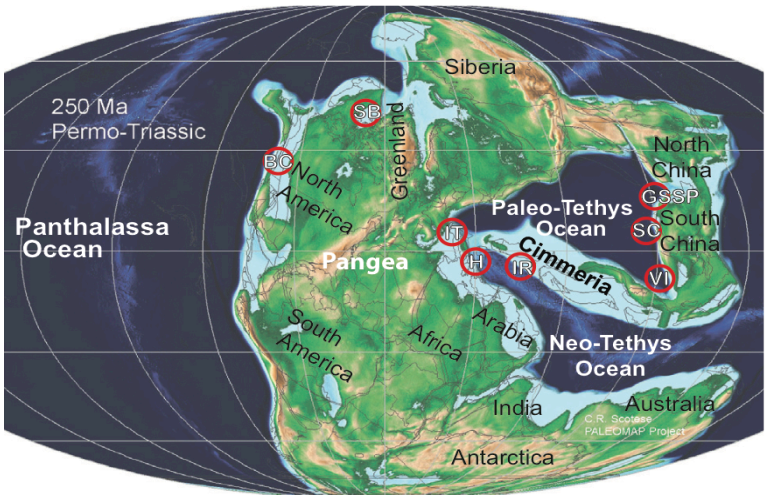

Figure 4-2 Reconstruction of the supercontinent Pangea with a Cathaysian bridge and shallow shelf (sills) separating the Paleo-Tethys Ocean from the Panthalassa and Neo-Tethys oceans (after C. Scotese, PALEOMAP project, 2014). Refer to Figure 4-1 for abbreviation definitions.

The isolation of the Paleo-Tethys by the Tethyan fragments may have contributed to the onset of oxygen-poor conditions in the region (Şengör and Atayman, 2009) due to restriction of current flow (Brandner, 1987). Establishing the extent of the passageway could be crucial because silled basins could have restricted the exchange of deep oxygenated waters between the Panthalassa and Tethys oceans causing dysoxic

(Tyson and Pearson, 1991; Wignall et al., 2010), anoxic (< 5 μmol L^{-1}) and/or euxinic conditions within the enclosed Tethys basins.

4.2 Previous modeling studies with Permian topography and bathymetry

Late Permian ocean circulation has been predicted by uncoupled ocean general circulation models (Hotinski et al., 2001; Zhang et al., 2001), models of intermediate complexity (Winguth et al., 2002; Montenegro et al., 2011), and fully coupled atmospheric and oceanic general circulation in comprehensive climate models (Kiehl and Shields, 2005). Models of intermediate complexity simulated coupled heat fluxes between the energy balance model and the oceanic general circulation, whereas freshwater and/or momentum fluxes are prescribed as forced boundary conditions. In contrast, comprehensive climate models consider a two-way coupling to the atmosphere, land, sea-ice, and ocean and thus are able to simulate feedbacks between the different components of the climate system. The Kiehl and Shields (2005) simulation was recently extended with a marine carbon cycle model to explore the decline of deep-sea dissolved oxygen concentration in response to increased nutrient input into the ocean, which would have enhanced the biological carbon pump (Winguth and Winguth, 2012). All previous studies, with the exception of Montenegro et al. (2011), assumed a flat ocean bottom configuration with an at least partially open deep-water (>2000 m) connection into the Tethys region. In order to determine the possible extent of anoxic conditions near the PTB, the paleobathymetric influences and continental positions should be considered. Isolation of basins by mid-ocean ridges, sills and/or shallow seas may restrict exchange of water masses; however, enhanced mixing also occurs due to obstacles, particularly with the flow over rough topography (St. Laurent and Garrett, 2002; Jayne et al., 2003).

4.3 Experimental design

In order to observe the possible influences of bathymetry during the Late Permian, two sensitivity experiments were completed. Both experiments considered atmospheric pCO_2 concentrations equivalent to 12.7 times the pre-industrial level (3550 ppmv). The first simulation featured a flat-bottom (hereafter referred to as the FB experiment) ocean floor configuration (Figure 3-1A) matching the previous model of Kiehl and Shields (2005). The second experiment, the MOR experiment, is used to assess the role of a possible mid-ocean ridge that may have extended across the Panthalassa in a general north–south direction (Figure 3-1B) and is discussed in further detail in Osen et al. (2013). The position of the mid-ocean ridge was based on the assumption that the active subduction zones along the western margin of Pangea were supplied by a spreading center analogous to the East Pacific Rise. Like the modern East Pacific Rise, the ancient Panthalassic spreading center may have been oriented parallel to the subducting margins that surrounded Pangea. The fact that mid-ocean ridges tend to be aligned parallel to convergent boundaries has been noted by several authors (Forsyth and Uyeda, 1975; Scotese and Rowley, 1985). The mid-ocean ridge was assumed to be at least 21 million years old and to have a fast spreading rate of 10 cm yr^{-1}, which is comparable to the spreading rate of the present East Pacific Rise. While the abyssal plain was assumed to have a depth of ~4000 m in the model, the depth of the ocean at the crest of the ridge was ~2800 m, based on the approach of Stein and Stein (1992).

An additional experiment was conducted to determine the possible influence of a closed Tethys region on the Permian oceans. The simulation, referred to as the Tethys experiment, included the addition of sills between the Paleo-Tethys and Panthalassa oceans as well as the Paleo-Tethys and Neo-Tethys (without a mid-ocean ridge; Figure 3-1C). The shallow sills effectively separated the Paleo-Tethys Ocean from the

Panthalassa, restricting the water exchange between the two oceans below a depth of 200 m, whereas a deep passage between these oceans was present in the FB and the MOR experiments. The modifications are based upon configurations from Scotese and Langford (1995) and topographic schemes by Ziegler et al. (1997; 1998).

4.4 Results from the influence of a mid-ocean ridge and sills on Late Permian oceans

The physical and geochemical results of the MOR and Tethys experiments as compared to the FB experiment are presented in the following sections. After 3000 years of model integration, 100-year mean global averages were computed for all three sensitivity experiments. Similarities between the three experiments were observed such as the average sea surface (~23ºC) and deep-sea (~5ºC) temperatures (Table 4-1). Sea surface temperatures (SST) in the equatorial region were in the range of 26ºC to 32ºC for all experiments, whereas high-latitude (75º-90º) SSTs ranged from 6ºC to approximately 9ºC. Ocean salinity concentrations were slightly higher than present-day ocean concentrations (~35 psu) when computed on a global scale with Late Permian mean totals simulated near 35.2 ± 0.7 psu (Table 4-2).

Table 4-1 Globally averaged ocean temperatures (ºC). Table adapted from Osen et al., 2013.

Experiment	Surface	200 m	600 m	1100 m	1900 m	2800 m	3800 m
FB	22.66	16.52	10.89	7.16	5.72	5.11	4.85
MOR	22.65	16.47	10.90	7.26	5.82	5.20	4.89
Tethys	22.59	16.36	11.04	7.54	6.10	5.48	5.12

Table 4-2 Globally averaged ocean salinities (psu)

Experiment	Surface	200 m	600 m	1100 m	1900 m	2800 m	3800 m
FB	35.20	35.49	35.30	35.00	34.89	34.86	34.85
MOR	35.20	35.50	35.31	35.00	34.89	34.84	34.82
Tethys	35.12	35.46	35.28	35.01	34.91	34.87	34.84

Major simulated sources of Late Permian deep-water masses were located at ~30º and in the polar regions in both hemispheres (Figure 4-3). Polar water masses were characterized by low temperatures (4-6ºC) and salinity concentrations (34.6-34.8 psu), whereas the subtropical water masses could be distinguished by warmer, more saline characteristics with temperatures ranging from 14 to16ºC and salinities of 35.3-35.5 psu.

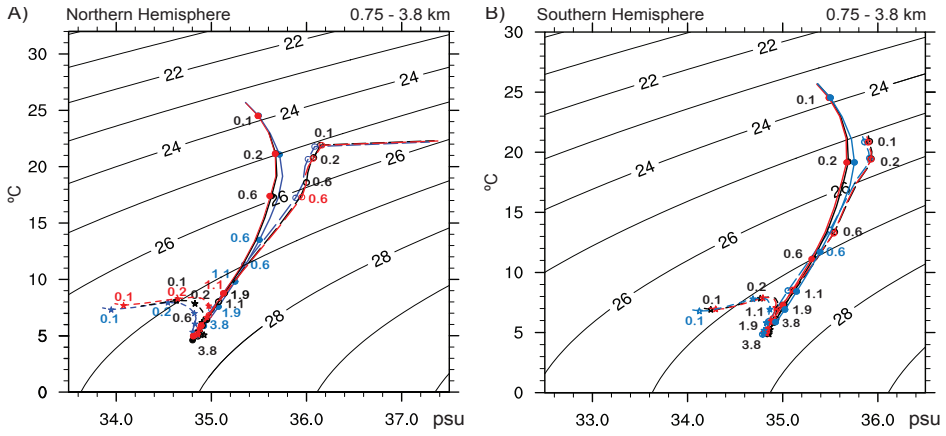

Figure 4-3 Temperature-salinity diagram for Late Permian sensitivity experiments. Temperature (ºC)-salinity (psu) profile about the equator (solid line), 30º (long dashes), and 60º (short dashes) for the FB (in black), MOR (in red), and Tethys (in blue) experiments for A) Northern Hemisphere and B) Southern Hemisphere. Dots denote the depth in km (adapted from Osen et al., 2013)

Subtropical water masses were comparable with present-day arid marginal seas such as the Mediterranean or Red seas. Ocean circulation was largely symmetrical about the equator with a transport of approximately 8-10 Sv near 30º with a weak meridional overturning circulation in deep water masses suggestive of stratification (Figure 4-4A).

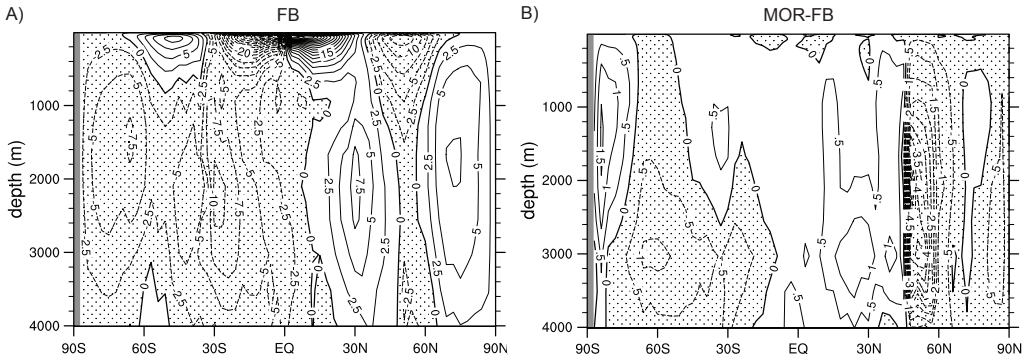

Figure 4-4 Meridional overturning circulation (MOC) in Sv (10^6 m^3 s^{-1}) of A) the FB sensitivity experiment, shaded areas with negative values represent regions of downwelling, and areas in white are regions of upwelling. B) Change in the MOC between MOR and FB experiments. Increased downwelling was simulated between 45°N and 60°N due to the addition of the mid-ocean ridge. The remaining ocean showed either no change or a slight decrease in overturning circulation.

4.5 Mid-ocean ridge influences on Late Permian ocean circulation and water mass distribution

Differences in global large-scale ocean circulation patterns between the MOR and the FB experiments were small (Figure 4-4) but regional changes did occur. For example, near 45ºN, deep-water transport increased by more than 4 Sv (Figure4-4B). The mid-ocean ridge induced topographic steering of the currents resulted in enhanced

vertical mixing altering regional oceanic temperatures and salinity concentrations. Regional anomalies in temperature of < 2 °C and in salinity of < 0.3 psu occurred in the shallow-to-intermediate water masses north and east of the ridge (Figure 4-5). However, changes in deep-sea temperatures (<0.5ºC; Figure 4-6A) and salinities (<0.1 psu; Figure 4-6B) were globally insignificant and confined to the region east of the mid-ocean ridge.

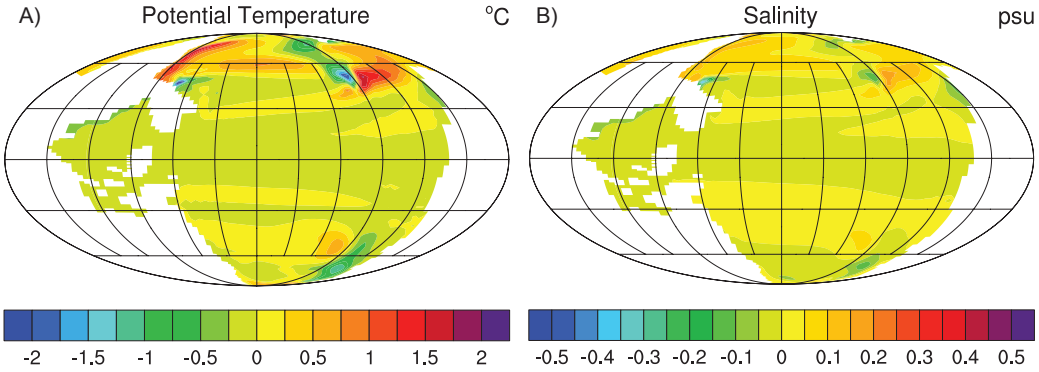

Figure 4-5 Differences in A) potential temperature (ºC) and B) salinity (psu) between MOR and FB experiments at a depth of 600 m.

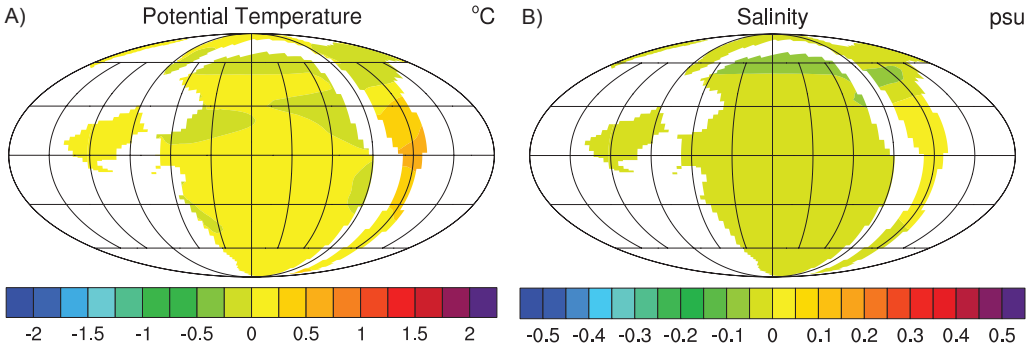

Figure 4-6 Differences between MOR and FB experiments for A) potential temperature (ºC) and B) salinity (psu) at 3800 m.

Below 2000 m, vertical velocities increased (Figure 4-7) due to topographic steering of the currents and increased mixing of the deep-sea water masses caused by the mid-ocean ridge. The increased mixing reduced the ideal age of water masses and increased dissolved oxygen concentrations (Figure 4-8A and Figure 4-8B) due to a slightly higher influence of warm and saline subtropical water masses in areas located east of the ridge. Similar to the FB experiment, anoxic conditions were simulated in the tropics off the west coast of Pangea in agreement with the Ursula Creek, British Columbia geological sediments that indicated the presence of anoxic water masses (BC, Figure 4-9A) during the latest Permian. In contrast, the deeper water masses remained well ventilated (Figure 4-9B). Neither the FB or MOR experiments simulated dysoxic nor anoxic conditions in the Tethys region where a majority of the lithologies indicate the presence of severely reduced dissolved oxygen content of the water masses during the latest Permian (Figure 4-9).

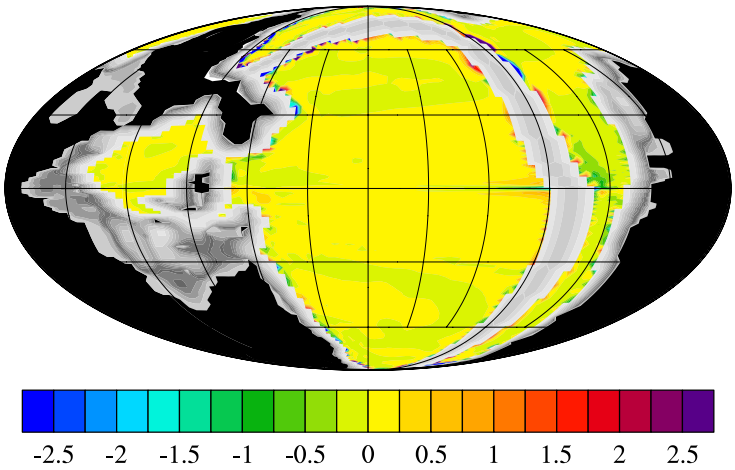

Figure 4-7 Differences in vertical velocities (10^{-6}m s^{-1}) between MOR and FB experiments. Changes in vertical velocities were primarily simulated along the mid-ocean ridge and to a lesser degree along the coastal areas in the eastern Tethys region.

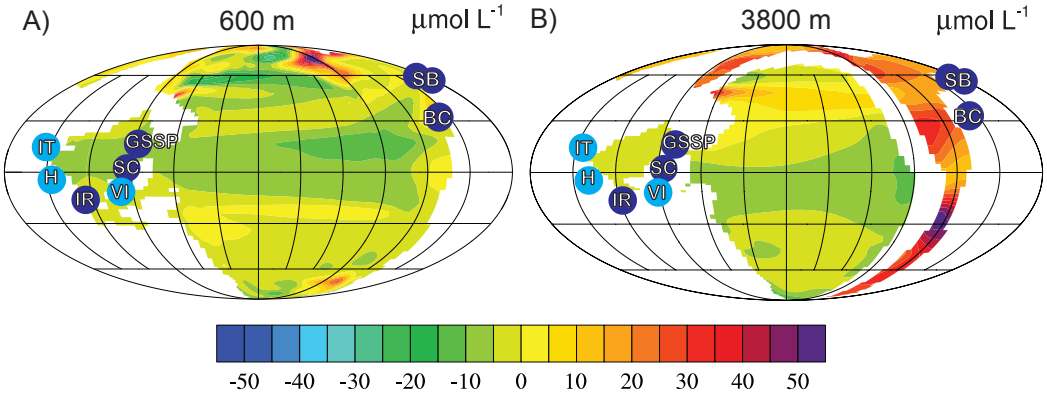

Figure 4-8 Change in dissolved oxygen concentrations (µmol L^{-1}) between the MOR and FB experiments for A) 600 m and B) 3800 m. Light blue circles depict where sediments indicate dysoxic to anoxic or euxinic intervals, dark blue circles signify locations containing largely anoxic or euxinic lithologies. Refer to Figure 4-1 for abbreviation definitions.

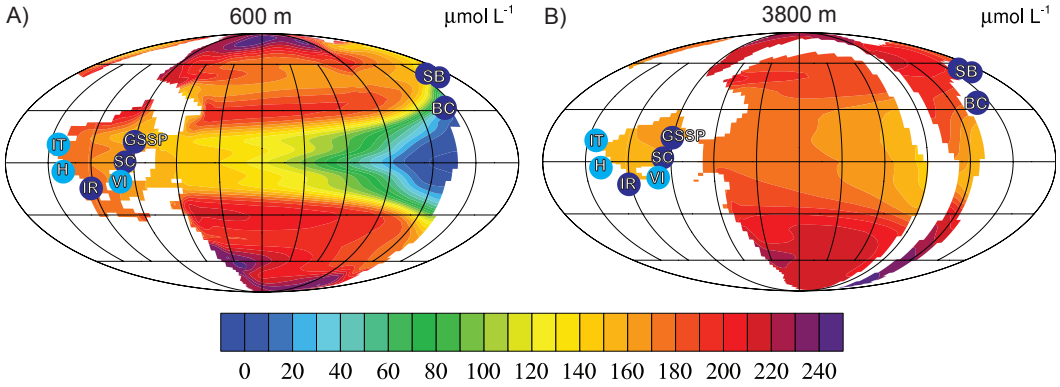

Figure 4-9 Absolute dissolved oxygen concentrations (µmol L^{-1}) for the MOR experiment for depths of A) 600 m and B) 3800 m. Light blue circles depict where sediments indicate

dysoxic to anoxic or euxinic intervals, dark blue circles signify locations containing largely anoxic or euxinic lithologies. Refer to Figure 4-1 for abbreviation definitions.

4.6 Influence of sill height on the ventilation of the Tethys

The exchange between Panthalassa and the Paleo-Tethys was disrupted by the reduction of the passage depth to 200 m that prevented the inflow of cooler deep-sea water masses from the Panthalassa to the Paleo-Tethys Ocean. Globally, the distribution of water masses and the meridional overturning circulation in the Permian oceans were not significantly affected by the sills (Figure 4-10); however, changes within the Paleo-Tethys region did develop. Due to the stronger influence of subtropical deep-water formation near Northern China, the temperature and salinity of intermediate water masses below 1000 m near the equator increased by up to 6°C (Figure 4-11A) and 0.9 psu (Figure 4-11B) respectively.

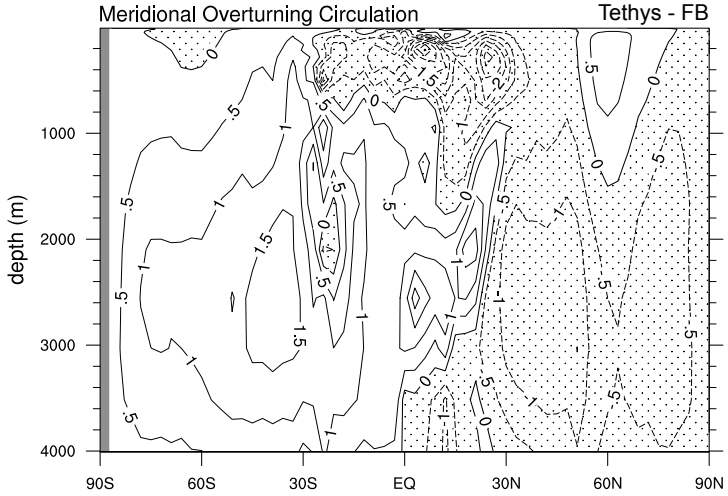

Figure 4-10 Change in meridional overturning circulation (Sv) between the Tethys and FB sensitivity experiments, shaded areas with negative values represent regions of downwelling, and areas in white are regions of upwelling.

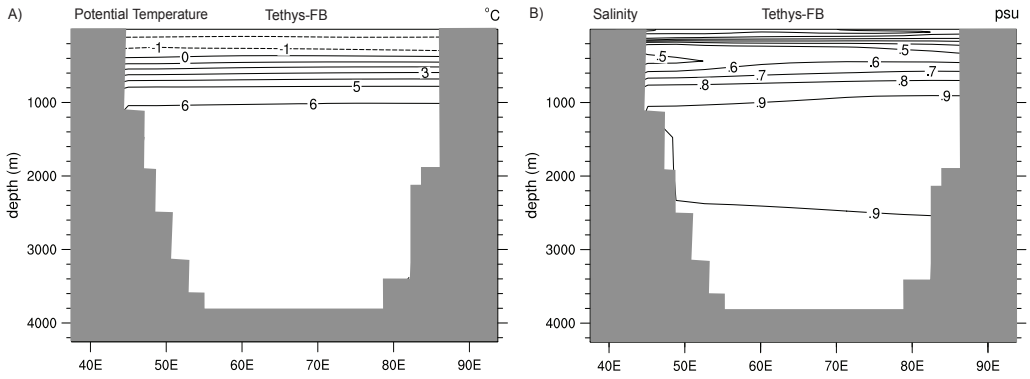

Figure 4-11 Change in temperature and salinity between Tethys and FB experiments Longitudinal sections of the difference between the Tethys and FB experiments about the equatorial Tethys region for A) potential temperature (ºC) and B) salinity (psu)

The isolation of the Paleo-Tethys region in the Tethys sensitivity experiment by the addition of sills increased stratification of water masses within the basin, comparable to the present-day Black Sea. Stratification can be identified by an increase in the value of an ideal age tracer in the deep-sea. The ideal age tracer implies a well-mixed environment with low age values and sluggish circulation with longer residence times. Deep-sea water masses within the Paleo-Tethys for the FB experiment suggested an age variance of 1200-1400 years (Figure 4-12A). In contrast, the Tethys experiment inferred an ideal age of greater than 3000 years because of isolation of the Paleo-Tethys Basin (Figure 4-12B) indicative of enhanced stratification. Water masses that are not well ventilated increase the likelihood of reduced or depletion of dissolved oxygen within the masses. Much of the sedimentary evidence from the Late Permian within the Paleo-Tethys ocean basin indicates that low to no oxygen environments were prevalent. The FB experiment suggests that circulation in the deep sea was weak yet may have been strong enough to maintain ventilation (Figure 4-12A); nevertheless, the ideal age of 1200 to

1500 years in the deep water masses suggested the likelihood of stratification. In contrast, the Tethys experiment simulated a remarkably sluggish circulation pattern with an ideal age exceeding 3000 years, suggestive of highly stratified water masses with very little ventilation (Figure 4-12B). The extreme ideal age of the deep sea would likely be in agreement with sedimentary evidence in the Paleo-Tethys ocean basin indicating the presence of dysoxic to anoxic or euxinic water masses.

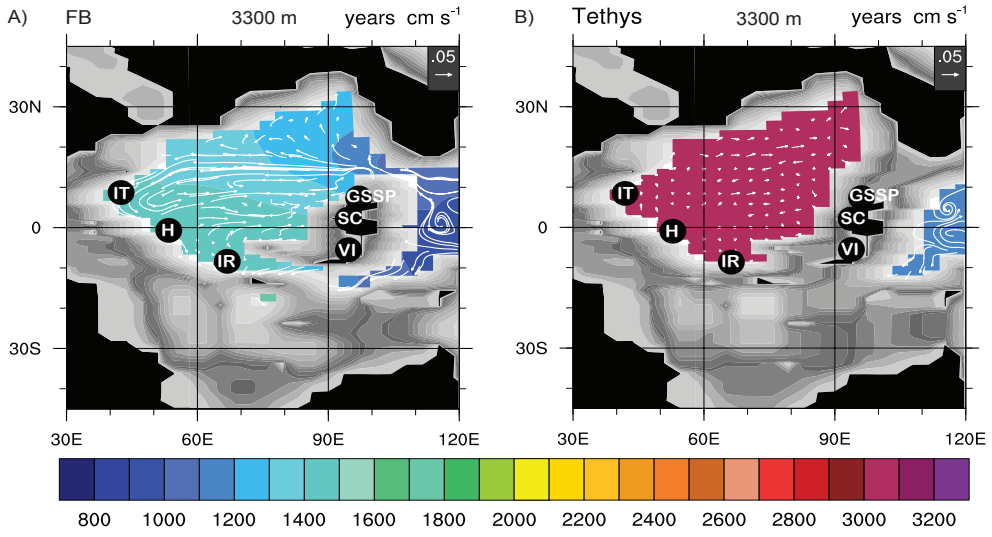

Figure 4-12 Comparison of ideal age of water masses for the FB and Tethys experiments. The absolute ideal age in years of water masses and horizontal velocities (cm s^{-1}) at a depth of 3300 m for A) FB experiment and B) the Tethys experiment. Refer to Figure 4-1 for abbreviation definitions.

Distribution of dissolved oxygen concentrations generally follows the distribution of the idealized age tracer, but oxygen concentrations are also dependent on local productivity. Productivity in the model was determined by the simulated export production

and depended upon macro- and micro-nutrient availability, temperature, and light availability (see section 3.1.5). Significant nutrient uptake will occur in areas of upwelling and deep mixed layers. Overall, global export production decreased by 3.1% in the Tethys experiment when compared to the simulated FB experiment (Table 4-3 and Figure 4-13A). However, the addition of the sills increased upwelling along coastal regions resulting in enhanced productivity in the southeast interior of the Paleo-Tethys basin (Figure 4-13B).

Table 4-3 Global Particulate Organic Carbon Export Production

Experiment Name	100 year average (Pg C yr^{-1})	Percent Change
FB	8.03	----
MOR	8.43	4.98
Tethys	7.78	-3.11
Present Day	6.73	-16.19

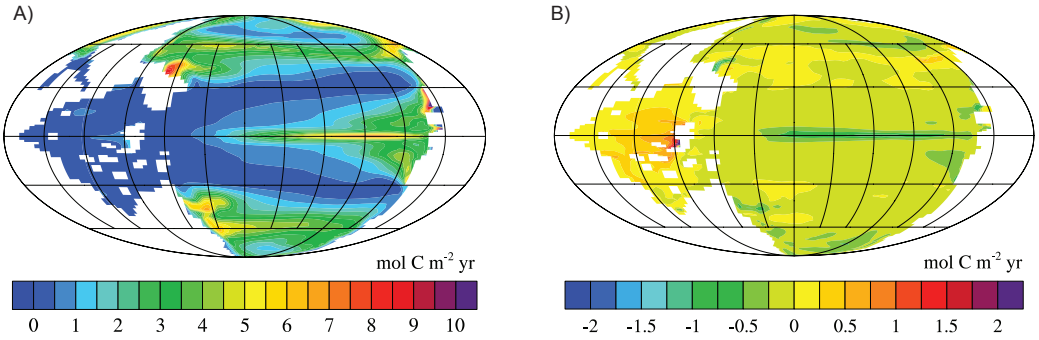

Figure 4-13 Particulate organic carbon (POC) production

Productivity simulated using POC export production in mol C m^{-2} yr^{-1} for A) FB experiment and B) the change in productivity between the Tethys and FB experiments.

Differences in the dissolved oxygen concentrations between the Tethys and FB experiments were also related to a warming anomaly, its associated stratification and the positive productivity fluctuation along the equatorial region of the southeastern Paleo-Tethys. At an intermediate depth of 500 m, dissolved oxygen gradients increased remarkably with the closure of the Paleo-Tethys. The developed oxygen minimum zone was located near a depth of 500 m rather than at 600 m as in the FB and MOR experiments. The results implied that dissolved oxygen concentrations as low as 25 µmol L^{-1} may have been located along the eastern interior shores of the Paleo-Tethys Ocean and are in general agreement with sediments found in Nhi Tao, Vietnam (VI in Figure 4-14A) in contrast to what was simulated in the FB experiment (Figure 4-14B).

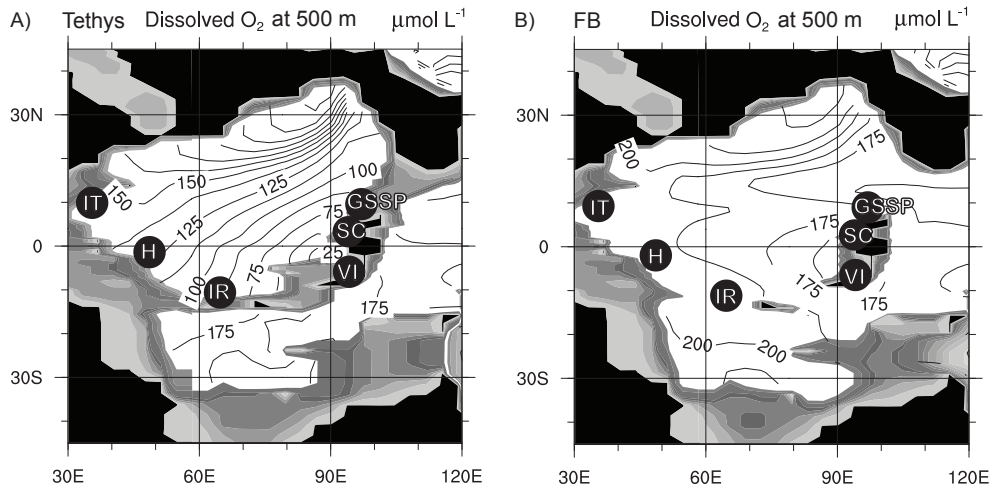

Figure 4-14 Absolute dissolved oxygen concentrations simulated for the Tethys region (includes the Paleo- and Neo-Tethys oceans) at 500 m for the A) Tethys experiment and B) FB experiment. The circles depict where sediments indicate dysoxic to anoxic or euxinic intervals, see Figure 4-1 for abbreviation definitions.

The enhanced stratification coupled with increased productivity (Figure 4-13) led to a decline in dissolved oxygen concentrations within the Paleo-Tethys Basin. Neither the FB or MOR experiments indicated anoxic conditions and are therefore in general disagreement with a majority of the sedimentary evidence. However, dysoxic conditions did develop in the deepest water masses (Figure 4-15). The presence of these deep water dysoxic conditions would be somewhat in agreement with the lithologies found for the Late Permian in Nhi Tao, Vietnam (VI), Bálvány, Hungary (H), and Jolfa, Iran (IR) that suggest at least intermittent periods of oxic-dysoxic to anoxic/euxinic conditions during the latest Permian.

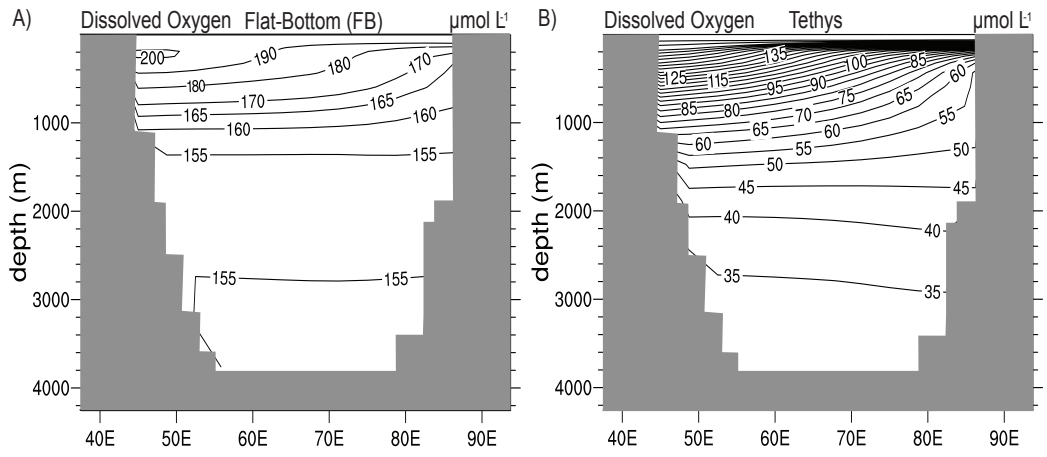

Figure 4-15 Simulated dissolved oxygen concentrations

Dissolved oxygen concentrations (µmol L^{-1}) for a longitudinal section of the Tethys region about the equator for A) FB experiment and B) Tethys experiment (from Osen et al., 2013).

4.7 Discussion

The addition of the mid-ocean ridge did not significantly change the global meridional overturning circulation. The ridge did alter regional water masses as it acted as a barrier preventing the northern Panthalassa bottom water masses from mixing with warmer waters located in the subtropics. A strong cell of upwelling located near the ridge curve at 80ºN (Figure 4-7) increased the meridional overturning circulation at depths between 1000 m and 2000 m promoting a downward mixing of subtropical warm and saline intermediate water masses that is implied by the change in temperature and salinity in Figure 4-5 and Figure 4-6. This increased mixing allowed for increased dissolved oxygen concentrations in areas located east of the ridge.

Both experiments suggested development of anoxic conditions within the oxygen minimum zone located off the west coast of Pangea. Results in Figure 4-9 are in general agreement with sedimentary evidence located in the Ursula Creek region of British Columbia (BC). The Ursula Creek region has been interpreted as having a progressive deterioration of oxygen levels during the Late Permian (Wignall and Newton, 2003). However, the Fantasque Formation of Ursula Creek is considered to be a distal, deep-water basinal setting (Wang et al., 1994), which would mean that the dark laminated shales were a result of anoxic bottom waters and not a continental shelf oxygen minimum zone as suggested by the FB and MOR experiments.

The FB and MOR experiments did not simulate anoxic conditions in the Tethys region (Figure 4-15) where the majority of euxinic to anoxic sedimentary evidence from the PTB has been identified (Yin et al., 2001; Newton et al., 2004; Erwin, 2006; Riccardi et al., 2006; Şengör and Atayman, 2009). Furthermore, deep-sea anoxia was not simulated in the Panthalassa or Tethys oceans with the present-day nutrient inventory, contrary to suggestions by Hotinski et al. (2001) and by Kiehl and Shields (2005) who

inferred anoxia from higher-than-present-day water mass stratification suggested by the ideal age tracer used in CCSM3.

The findings of this study propose that the deep Panthalassa and Tethys oceans were not anoxic as dissolved oxygen concentrations remained >120 μmol L^{-1}. These results are consistent with Winguth and Maier-Reimer (2005) and Montenegro et al. (2011) who conducted sensitivity experiments using climate models of intermediate complexity. The later study featured two mid-ocean ridge configurations in which one was a straight ridge placed directly through the middle of the Panthalassa Ocean in a north-south direction and a second wherein the mid-ocean ridge traverses the Paleo-Tethys and becomes a U-shaped ridge within the Panthalassa. Additionally, Meyer and Kump (2008), Meyer et al. (2008) and Winguth and Winguth (2012) suggested a high sensitivity of the deep-sea oxygen concentration to changes in the nutrient inventory and an enhanced biological pump.

The closure of the Paleo-Tethys region in the Tethys sensitivity experiment generated stratified water masses within the basin. These changes were associated with an increase in the ideal age of deep-water masses and led to a decline in dissolved oxygen concentrations within the Paleo-Tethys Basin suggesting the existence of dysoxic conditions (Figure 4-14 and Figure 4-15). Sengör and Atayman (2009) suggested that a combination of atmospheric, lithospheric and biospheric changes in the Paleo-Tethys contributed to the anoxic conditions in the latest Permian. Dysoxic conditions were present along the eastern inner shores of the Tethys region within the oxygen minimum zone and are supported by evidence of Chlorobiaceae (green sulfur bacteria), a biomarker indicator of anoxygenic photosynthesis, in the Meishan section located in South China (GSSP, Figure 4-14; Grice et al., 2005; Cao, 2009). Evidence of oxic-dysoxic to euxinic episodes in the Dong Dang Formation of Nhi Tao, Vietnam (VI, Figure

4-14), a shallow-marine environment in the Late Permian (Algeo et al., 2007), is consistent with the Tethys experiment. Indicators of an oxygen-restricted environment are also present in Northern Xinjang, China (Cao et al., 2008) and Shangsi, China (SC, Figure 4-14; Riccardi et al., 2006). Permian–Triassic sections in South China suggest an increase in salinity that may have been induced by rising temperatures and evaporation rates (Chai et al., 1992), which is in agreement with the Tethys sensitivity experiment (Figure 4-11B).

Dysoxic conditions were not modeled for the western shores of the Paleo-Tethys region, conflicting with geological evidence inferring anoxic-euxinic conditions in the Bálvány section of Hungary (Kaiho et al., 2006; Gorjan et al., 2007), Siusi section of Northern Italy (Twitchett and Wignall, 1996; Newton et al., 2004) and the dysoxic-euxinic intervals present in the Bulla section (Gorjan et al., 2007) also located in Northern Italy (H and IT; Figure 4-14A). However, dissolved oxygen concentrations were significantly reduced when compared with the FB experiment, thus insinuating that a closed Paleo-Tethys Basin could have been a significant factor in the declining marine conditions. The difference could be related to the coarse resolution of the model rendering it unable to resolve coastal process, or due to uncertainties in the prediction of coastal winds influencing the buoyancy forcing and Ekman-upwelling.

Though dysoxic conditions were simulated within the deep sea of the Paleo-Tethys Ocean, much of the geological evidence supports anoxic/euxinic conditions during the latest Permian. Limiting factors that may have contributed to the model's inability to predict anoxic bottom waters within the Paleo-Tethys Basin include the low resolution that limits the representation of bathymetric features such as seamounts, small islands or trenches which could further influence oceanic circulation. The sulfur cycle was not included in any of the simulations. With the long-term eruptions of the Siberian Traps

during the Late Permian, large amounts of sulfur dioxide would have been released into the atmosphere (Reichow et al., 2002; Heydari et al., 2008; Saunders and Reichow, 2009) that would have been converted to sulfuric acid and increased weathering and erosion rates. Conversely, large amounts of sulfur would have been added to the oceans likely disrupting biogeochemical cycles. Sediment and silicate cycles were not included in the experiments, which may have influenced productivity and ocean chemistry. Geological evidence suggests that an increase in erosion may have played a role in the deterioration of oceanic conditions (Algeo et al., 2007; Wang and Visscher, 2007). Though there are limitations to the modeling study, it is clear that an increase in greenhouse gases alone cannot be the sole factor in the degradation of oceanic waters near the PTB. This study does suggest the likelihood of a closed Paleo-Tethys Basin that restricted circulation and contributed to the onset of anoxic conditions, which is prevalent throughout the geological record. In contrast, the study also implies that ocean anoxia was likely limited to continental shelf areas rather than extending into the deepest water masses in the Panthalassa Ocean.

4.8 Conclusion

The placement of a mid-ocean ridge within Panthalassa had only a minor impact on the global water mass distribution and oceanic conditions. Thus, the flat-bottom approach in ocean models for the Late Permian remains a valid approximation. Increased upwelling near the ridge due to topographic steering redirected flows about the ridge but did not significantly change temperature and salinity distributions within the Panthalassa.

The introduction of a sill between the North and South China blocks induced a decrease of circulation and enhanced stratification within the Paleo-Tethys, which led to the development of dysoxic conditions in the region. Global currents and meridional

overturning circulation were impacted to a much smaller extent. For an isolated Paleo-Tethys, deteriorated environmental conditions with warm temperatures and low oxygen would have contributed to the regional extinction of species; however, these changes would probably not have been sufficient to explain the global marine mass extinction.

Chapter 5

Climate-Sensitive Sediments and Water Masses

5.1 Introduction: Relationship of water masses and climate-sensitive sediments

Permian water masses had been inferred from climate-sensitive sediments that have been highly correlated to present-day distribution of water masses (Ziegler et al., 1998); however, the incompleteness of the stratigraphic record limited the analysis to nine stages during the Permian and may have introduced sampling biases (Vaughan, 2007). The lithological markers can validate climate simulations and thus improve the understanding of climate mean state and variance as illustrated in studies of the transition of Early Permian ice-house from the Sakmarian (Early Permian) conditions to the Wordian (Middle Permian) near-ice free environment (Gibbs et al., 2002; Winguth et al., 2002). A further transition occurred from the greenhouse world at the Changhsingian (Late Permian) to a hothouse world in the Smithian (Early Triassic; Sun et al, 2012), culminating with the Permian-Triassic mass extinction, which likely occurred in less than 60 kyr (Rampino et al., 2000; Twitchett et al., 2001; Kamo et al., 2003; Kidder and Worsley, 2010). Due to the rapid release of greenhouse gases by the Siberian Traps, the climatic changes that transpired near the PTB could serve as an ancient analog for the future (Payne and Clapham, 2012), as present-day anthropogenic greenhouse gases emitted to the atmosphere increase at a rapid rate (Keeling et al., 2005). The geological records of climate-sensitive sediment types are broadly similar to their environments of formation today, with their distribution largely controlled by atmospheric and oceanic circulations (Ziegler et al., 2003). Thus, sensitivity experiments featuring lithological markers and oceanic water mass identification enhance our understanding of rapid climate change at the Permian-Triassic transition.

Ziegler et al. (1998) defined the climate-sensitive sediments equivalent of the terrestrial biome. Sedimentary deposits influenced by climate, referred to as climate-sensitive sediments, were correlated with water masses, which are categorized by certain sea surface temperature and salinity ranges (Helland-Hansen, 1916). Climate-sensitive sediments of nine Permian stages have been summarized in paleogeographic maps (Ziegler et al., 1998) with eight climatic zones based on a modern analog in which recent sedimentary deposits were compared with present-day oceanic water masses.

Table 5-1 General surface water mass classification based on present-day conditions and climate-sensitive sediments. Temperature range for Glacial and Cold Temperate was adjusted from -1.8ºC to -1.4ºC to account for lower salinity present near the poles. Table modified from Ziegler et al. (1998) and Winguth et al. (2002).

Climate zone	Water mass description	Climate-sensitive sediments	Temperature range (ºC)	Salinity range (psu)	Present-day example
Glacial	Marine till	Surface permanently frozen	< -1.4	–	Ronne Ice Shelf
Cold Temperate	Winter ice floes	Dropstones, rhythmites	-1.4 - 0	–	Labrador Current
Wet Temperate	Brackish surface waters	Temperate peats, organic-rich shales, clastics	0 - 20	< 32	Baltic Sea
Temperate	Mixed water column	Clastics	0 - 20	32 - 37	Kuroshio Current
Cool Subtropical	Upwelling currents	Organic-rich shales, phosphorites, cherts	–	–	Humboldt Current
Dry Subtropical	High evaporation	Gypsum, halite, sabkha facies	–	> 37	Persian Gulf
Tropical	Deep light penetration	Carbonates, bauxites, oolites, coral, and algal reefs	> 20	32 - 37	Bahamian Platform
Wet Tropical	High continental runoff	Peats, muddy sediments	> 20	< 32	Indonesian Seaway

A brief description of climate-sensitive sediments used by Ziegler et al. (1998) is discussed below:

Carbonate buildups: Carbonate platforms such as reefs, mud mounds containing large amounts of micrite, and oolites are included in this group. Evidence of carbonate buildups served as an indicator of tropical climates where sunlight is able to penetrate into deeper waters.

Coals: Formed from peat accumulations in environments that tend to be highly productive and where oxidation of vegetation is reduced. Peat accumulation can be found in humid regions with a high water table and where precipitation is usually greater than 100 cm yr^{-1} (Ziegler, 1990; Ziegler et al., 2003; Tabor and Poulsen, 2008).

Evaporites: This type of sediment encompasses salts such as halite, anhydrite, sylvite and gypsum, which form when evaporation exceeds precipitation in regions previously covered by shallow marine or lake waters.

Eolian sands: The build-up of sands caused by wind activity where vegetation tends to be sparse and there is an abundance of unconsolidated sediments results in eolian sands being found in arid regions.

Oil source rocks: These include shale and limestone rich in organic matter. Shale and limestone rich in hydrocarbons are often formed in restricted basins under anoxic conditions and can have marine or lacustrine origins. Oil source rocks are also an indicator for high surface productivity (Ziegler et al., 1997) and could be the result of estuarine circulation pattern (Gibbs et al., 2002).

Phosphorites: These are considered indicative of ocean upwelling where nutrients are brought from the deep sea towards the surface by strong currents. Regions of upwelling are productive because of the continuing supply of nutrients. Phosphorite deposits are also known to be found in estuarine environments where nutrients are supplied by rivers.

Table 5.1 summarizes the present-day relation between climate-sensitive sediments and water mass distribution. The following marine climatic conditions can be inferred from these sedimentary deposits:

Wet Tropical: Water masses in the wet tropical zones that have temperatures above 20ºC with salinities below 32 psu are considered brackish. High run-off is received from the surrounding land and high turbidity is common. Modern-day examples would be major deltas such as the Amazon or a shallow, narrow seaway located near the equator such as found near Indonesia. Sediments are typically muddy and tropical peats may form. Over time, organic-rich shale may form, especially if the basin is restricted. The restriction of the basin coupled with high rainfall result in productive estuarine waters.

Tropical: Tropical water masses have temperatures above 20ºC with an average salinity range (32 – 37 psu). The water is typically clear and light penetration can reach the bottom due to the zenith angle of the sun in low latitudes. Carbonate build-ups are common in areas with good circulation due to calcareous secreting algae and corals. A modern-day example would include the Bahamian Platform, as tropical water masses are ideal conditions for reefs. Algal mats and oolite shoals may also be present in tropical water masses.

Dry Subtropical: Evaporation exceeds precipitation and waters are characterized by salinities exceeding 37 psu. Dry Subtropical zones can be identified by the presence of evaporites. Modern day examples include the Mediterranean and Savannah climates.

Cool Subtropical: Ziegler et al. (1998) reserved this category for upwelling zones, which are usually limited to subtropical areas where winds are strong enough to drive Ekman transport. The upwelling of nutrient-rich deep waters promotes productivity. The decay due to the high productivity in these regions consumes oxygen and tends to preserve the organic matter on the ocean floor. Sediments common to these regions include organic-

rich muds and phosphorites. Modern-day examples include areas along the eastern currents of both the Atlantic and Pacific Oceans.

Temperate: Temperature ranges from 0º to 20ºC with normal salinity. Peats are common in the temperate zone but they are not exclusive to this region. Typically the modern-day peats of the temperate zone form in the mid to high latitudes due to low evaporation rates.

Wet Temperate: Brackish waters occur with salinities below 32 psu and temperatures between 0º and 20ºC. Conditions are ideal for the formation of organic-rich muds and peats, and estuarine circulation often occurs. Modern-day examples are the Baltic and Black seas where the combination of high rainfall and restricted basins induces fresh water cap conditions.

Cold Temperate: Temperatures are typically near 0ºC and sea ice can be present during the winter season. Diamictites, dropstones and rhythmites are indicators of this environment. Modern-day cold temperate zones are not symmetrical due to high-pressure cells that tend to drive poleward currents such as the Norwegian Current on the west side of continents as well as the equatorward currents (Labrador Current) on the east sides (Ziegler et al., 1998).

Glacial (Polar): Glacial zones are typified by year-round ice floes and waters are consistently below 0º due to salinity content. Modern-day examples can be found in the Arctic Ocean as well as the Ronne and Weddell Ice shelves surrounding Antarctica. Tills can be found associated with glaciers and can be utilized as a climatic marker.

Besides the climate-sensitive sediments used by Ziegler et al. (1998) and Winguth et al. (2002), bauxite was added as an additional climate-sensitive sediment to extent the interpretation of climatic changes in tropical to subtropical zones (Boucot et al., 2013). Formations of bauxite, an aluminum ore, typically result from lateritic weathering

and are suggestive of tropical climates. Bauxite consists mostly of the minerals gibbsite, boehmite, and diaspore that are often mixed with the iron oxides of goethite and hematite, as well as the clay mineral kaolinite.

5.2 Sensitivity to greenhouse gas levels

The concentration of carbon dioxide in the atmosphere near the PTB is controversial; atmospheric pCO_2 concentrations are estimated to have risen from a background level of about four to five times the preindustrial atmospheric concentration of 280 ppmv (Berner, 2002) to as much as eight times preindustrial concentrations or more (Gibbs et al., 2002; Rees et al., 2002; Montañez et al., 2007). In this study, an atmospheric pCO_2 equivalent of 12.7 times the preindustrial level is assumed (Kidder and Worsley, 2004; Kiehl and Shields, 2005). The rapid increase of the tropical sea surface temperatures from ~25ºC to ~40ºC in the Early Triassic (Sun et al., 2012; Joachimski et al., 2012) suggests a massive increase in radiative forcing that was likely caused by a rise in greenhouse gas emissions into the atmosphere (Kidder and Worsley, 2004). Sensitivity studies with climate models of intermediate complexity (Gibbs et al., 2002; Winguth et al., 2002) and analyses of sedimentary geochemical records (Montañez et al., 2007) have postulated that the climate change during the Permian may have been linked to a rise in the greenhouse gas concentration in the atmosphere. In the following, we investigated the impact of the carbon perturbation on the climate zones by comparing the simulation with a pre-PTB atmospheric CO_2 concentration of 4 × CO_2 with the one disrupted by an additional 4872 PgC (or increase of atmospheric pCO_2 to 12.7 × CO_2; Kiehl and Shields, 2005) and compared the findings with climate-sensitive sediments inferred from Ziegler et al. (1998).

5.3 Water mass reconstruction for the Middle Permian

Water mass reconstruction was performed by correlating surface sediment types (Table 5-1) with sea surface temperature, salinity, and upwelling. These sediment types are rarely confined to just one water mass category, as they tend to be deposited along seaways and coastal regions with geographic or bathymetric limitations (Ziegler et al., 1998). As inferred by Gibbs et al. (2002), Early-to-Middle Permian simulated climate trends that resulted from changes in paleogeography, orbital cycles, and greenhouse gas concentrations, are generally in agreement with the changes in climate-sensitive deposits such coal, evaporite, or organic-rich shale. Winguth et al. (2002) used the water mass classification of Ziegler et al. (1998) with a 4 × CO_2 baseline experiment to analyze Middle Permian (Guadalupian) conditions and found them to be in general agreement with the paleoclimatic data; however, the 8 × CO_2 experiment simulated conditions that appeared to be too warm in the high latitudes compared to the geological record.

5.4 Comparison of present-day simulated climate with climate-sensitive sediments

The prediction of present-day water masses using the Ziegler et al. (1998) classification scheme was validated with observations to assess potential error sources for the reconstruction of past climate zones. The observed water mass distribution was computed from objectively analyzed datasets from the World Ocean Atlas (WOA) 2009, which contained in-situ measurements of temperature (Locarnini et al., 2010), salinity (Antonov et al., 2010), dissolved oxygen (Garcia et al., 2010), as well as other climatological fields. Measurements were taken at standard depth levels for annual, seasonal and monthly periods. The WOA 2009 is a product of the Ocean Climate Laboratory of the National Oceanic Data Center (http://www.nodc.noaa.gov/OC5/indprod.html). Water masses were determined using the temperature and precipitation

parameters listed in Table 5.1. Figure 5-1 illustrates how the temperature, precipitation and upwelling data are characterized by type of water mass.

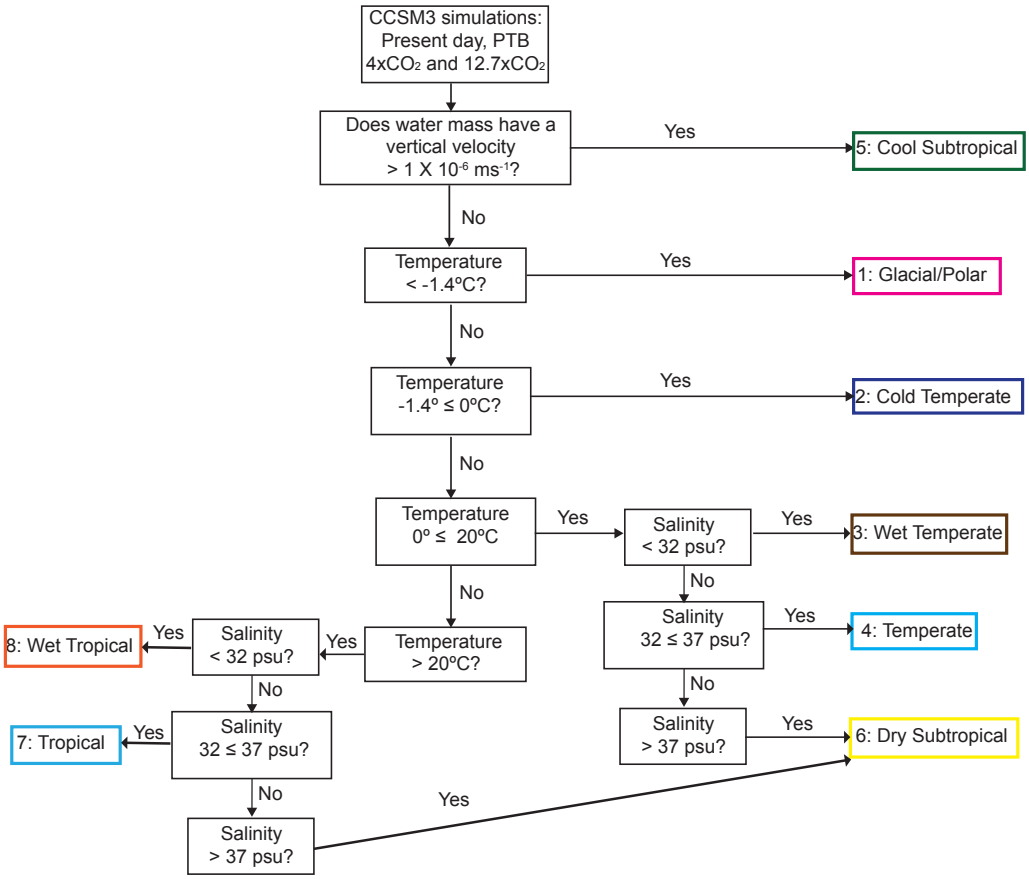

Figure 5-1 Flowchart demonstrating how water masses are determined from simulated data. For additional information on CCSM3 simulation parameters see Table 5.1.

Present-day temperature and salinity observations from WOA 2009 on a 1º × 1º grid are interpolated to the CCSM3 model grid, described in section 3.1, to assess the model-data bias. The CCSM3 present-day simulation is in general agreement with the

observations; however, model-data differences exist for the North Atlantic including the Greenland and Norwegian seas (denoted as area a) due to cool simulated Siberian temperatures (section 6.3) as well as for the Atlantic sector of the Southern Ocean and the Ross Sea (represented by the letter j in Figure 5-2 and Figure 5-3). These discrepancies can be linked to biases in areas of deep-water formation and Antarctic temperatures. Lower than observed salinity concentrations of 1-2 psu were simulated by the CCSM3 model from the Gulf of Alaska to the tip of the northern coast of California (area b in Figure 5-2 and Figure 5-3), in the Labrador Sea and down the coastal regions to Boston, MA (area c in Figure 5-2 and Figure 5-3), as well as in the Bering Sea, Sea of Okhotsk, and along the Kuroshio Current (Bering Sea region indicated by the letter d in Figure 5-2 and Figure 5-3). The underestimation of salinity in these regions caused wet temperate zones to be exaggerated. The model-data bias is partially linked to a precipitation bias (Figure 5-4C) and a coarse resolution impediment in CCSM3's ability to resolve complex precipitation patterns within small mountain ranges and mountainous areas located near the coast. These precipitation model-data differences in the simulation (Figure 5-4) also contributed to the bias of wet tropical zones from the coasts of French Guiana to São Luis, Brazil (area g in Figure 5-2 and Figure 5-3). The salinity bias of 2-6 psu between the observations and CCSM3 along the southwestern coastline of Africa from the Gulf of Guinea to Angola (represented by the region marked as h in Figure 5-2 and Figure 5-3) and the 1-10 psu discrepancy near the Indonesian Throughflow (region i in Figure 5-2 and Figure 5-3) resulted in an overestimation of wet tropical zones related to coastal processes not resolved in CCSM3, excessive freshwater flux, and a precipitation bias that had been documented in previous studies (Yeager et al., 2006).

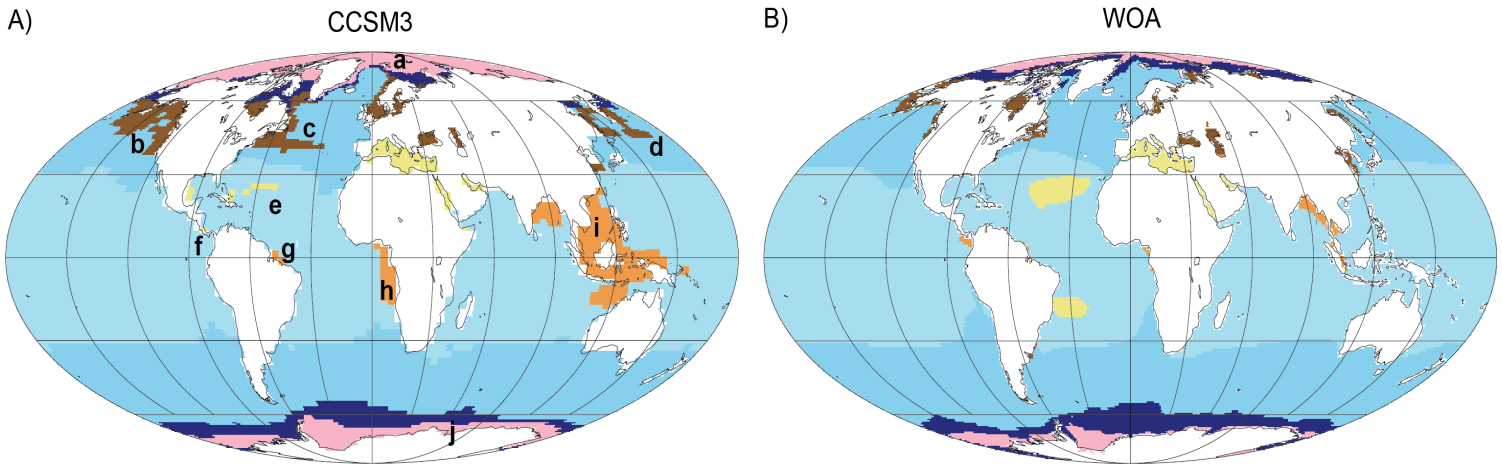

Figure 5-2 Comparison of water mass classifications for modern-day climate for A) CCSM3 simulation (T31x3 or ~3.75º × 3.75º) and B) data from the World Ocean Atlas (WOA, 1 × 1 degree grid). Lower case letters a-j signify regional disagreements between CCSM3 and WOA water mass projections at Greenland and Norwegian seas (a), Gulf of Alaska (b), Labrador Sea (c), Bering Sea (d), Atlantic Ocean (e), NW Columbia coast (f), NE Brazilian coast (g), Gulf of Guinea (h), Indonesian Throughflow (i), and the Southern Ocean (j). Details regarding discrepancies are explained in section 5.4 and correlate with maps in Figure 5-3A and Figure 5-3C.

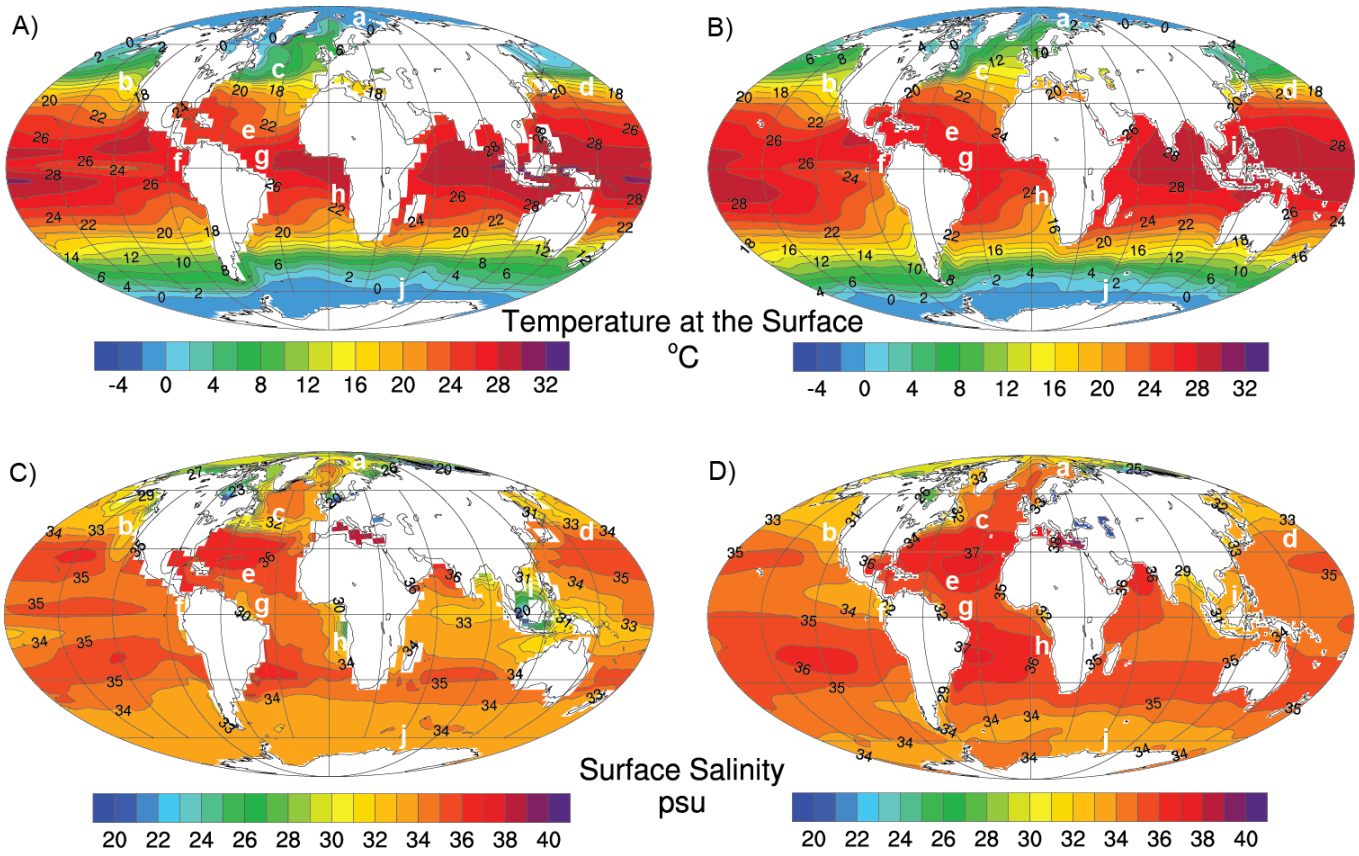

Figure 5-3 Comparison of ocean temperatures for A) CCSM3 and B) WOA 2009 data analysis, and for ocean surface salinity for C) CCSM3 and D) WOA 2009 data analysis. Lowercase letters a through j mark regions of disagreement between CCSM3 simulation and WOA data that are discussed in section 5.4. Regional letter identification is listed in Figure 5-2.

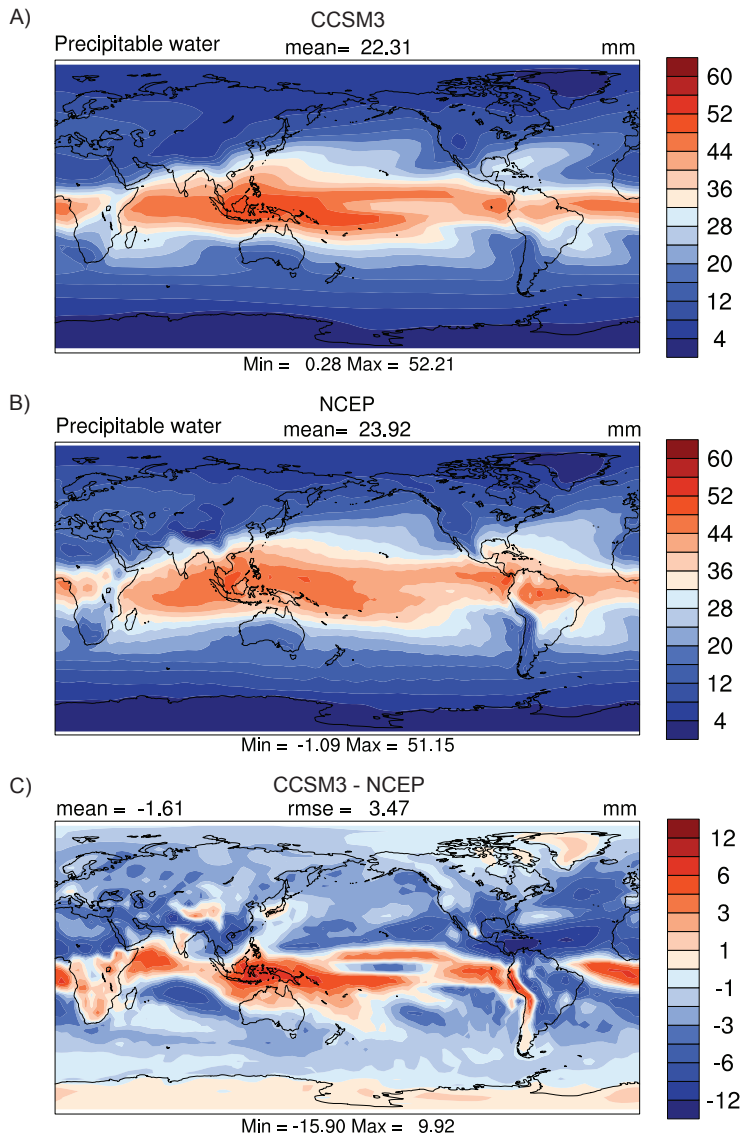

Figure 5-4 Comparison of the annual mean modern-day precipitable water (mm) for A) CCSM3 T31x3 simulation B) NCEP reanalysis and C) the differences between the CCSM3 simulation and NCEP reanalysis.

The salinity bias between the observations and CCSM3 in the tropics (regions of the Atlantic Ocean depicted in e and the Indonesian Throughflow marked with i in Figure 5-2 and Figure 5-3) is related to a precipitation error in CCSM3 (Collins et al., 2006; Large and Danabasoglu, 2006) that led to a double Intertropical Convergence Zone (ITCZ; Figure 5-4 with extensive rainfall being simulated over the tropical Atlantic and Pacific due to warm sea surface temperature (SST) biases that develop off the southwest region of Africa (Yeager et al., 2006) depicted in Figure 5-3A and Figure 5-3B. Anomalously cool SSTs in the southern Indian Ocean also reduced the southern ITCZ during the South Asian monsoon season (Meehl et al., 2006). These anomalies are associated with the parameterized cloud processes, as these biases are seen in the radiation budget at the top of the atmosphere and correlate with the precipitation fields (Yeager et al., 2006). Weak, long-shore surface wind stress portrayed in the model is expected to produce less coastal upwelling and likely contributed to even warmer surface temperatures (Yeager et al., 2006). Both the observed data and the CCSM3 simulation suggest cool temperate conditions in the mid-latitude regions and cold temperate conditions to exist around the 0º isotherm.

5.5 Late Permian water mass analyses

Two sensitivity experiments containing identical topographic and bathymetric configurations (see Figure 3-1B, Table 3-1, and subsection 3.1.6) were conducted with different atmospheric CO_2 concentrations. The 4 × CO_2 experiment (Winguth et al., 2013) used radiative forcing comparable to previous studies (Rees et al., 1999; 2002; Gibbs et al., 2002; Winguth et al., 2002) for the pre-PTB conditions. The 12.7 × CO_2 (3550 ppmv) experiment for the PTB is analogous to the study of Kiehl and Shields (2005), but was integrated further to 8,000 years and included a biogeochemical module (Winguth and

Winguth, 2013). The amount in the carbon perturbation relative to pre-PTB conditions is in agreement with previous studies (Kidder and Worsley, 2004). These climate simulations were compared to climate-sensitive sediments from the Middle and Late Permian following the same approach as listed in section 5.4.

Globally averaged air surface temperature and precipitation totals are summarized for each experiment in Table 5-2. Temperature increased with the rise of atmospheric pCO_2. The 4.0ºC difference in global surface temperature between the 12.7 × CO_2 and 4 × CO_2 experiments was related to a net change in radiative forcing i.e. increase in atmospheric pCO_2, which follows a natural logarithmic relationship (Berner and Barron, 1984; Kiehl and Dickinson, 1987; Gibbs et al., 2002; Winguth et al., 2002).

Table 5-2 Global annual averages of temperature, precipitation, and the difference between 12.7 × CO_2 and 4 × CO_2 experiments.

	Temperature (ºC)			Precipitation (mm day^{-1})		
Experiment	Land	Ocean	Global	Land	Ocean	Global
4 × CO_2	15.1	19.3	18.2	1.8	3.2	2.8
12.7 × CO_2	20.6	22.7	22.2	2.0	3.4	3.1
Difference between 12.7 × CO_2 – 4 × CO_2	5.5	3.4	4.0	0.2	0.2	0.2

Zonal sea surface temperatures averaged for annual (Figure 5-5A), boreal winter (Figure 5-5B), and boreal summer (Figure 5-5C) suggest an overall increase (3.4ºC or 3.4 K) in temperatures with pronounced warming (> 4.5 K) in latitudes greater than 35º in both

hemispheres (Figure 5-6). Warming of the sea surface in the Northern Hemisphere was greatest near 50ºN where the annual average increased by 5.2ºC (5.2 K Figure 5-6A) with a peak average of 5.9ºC (5.9 K) during the summer months (Figure 5-6C). Winter months were also significantly warmer with a 4.6 K increase in temperature at 50ºN and a 4.5ºC or 4.5 K warming near the poles (Figure 5-6B). In the Southern Hemisphere, warming was most significant near 40ºS during the boreal winter with an average temperature of 4.8ºC (4.8 K; Figure 5-6B) and at 55ºS during the boreal summer (Figure 5-6C) with the mean temperature reaching 6.4ºC (6.4 K). The Southern Hemisphere higher latitudes experienced a larger increase of warming due to increase in pCO_2; results were similar to those of Gibbs et al. (2002) when they compared the increase in atmospheric carbon dioxide concentration from Sakmarian to Wordian from 4 x CO_2 to 8 x CO_2. However, unlike Gibbs et al. (2002), the southern section of the Panthalassa did not remain cold enough to support permanent ice sheets.

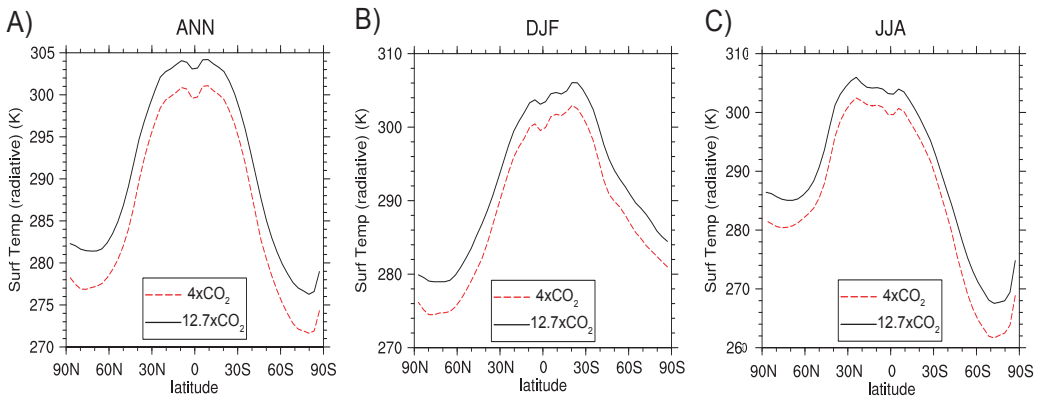

Figure 5-5 The zonally averaged surface air temperatures (K) for the 12.7 × CO_2 (Late Permian) and 4 × CO_2 (Middle Permian) CCSM3 simulations A) Annual, B) boreal winter, and C) boreal summer.

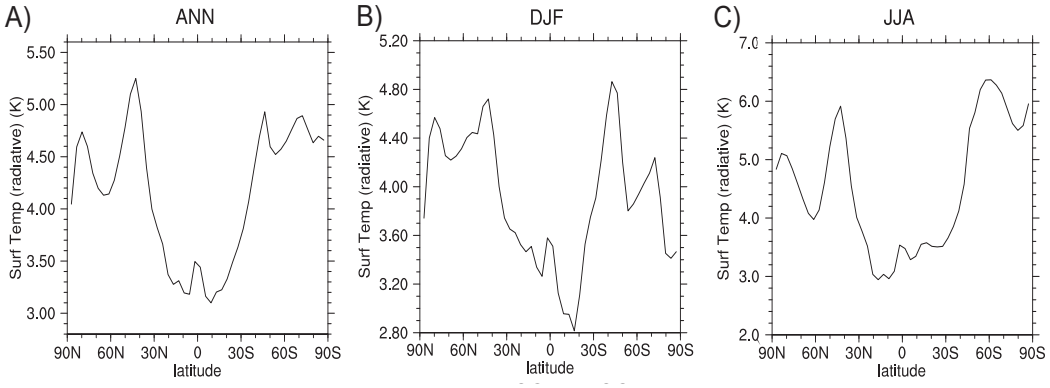

Figure 5-6 The difference between the zonal averages of surface air temperatures (K) between 12.7 × CO_2 (Late Permian) and 4 × CO_2 (Middle Permian) simulations with CCSM3 for A) annual, B) boreal winter, and C) boreal summer.

On the land, the comparison of the 12.7 × CO_2 to the 4 × CO_2 experiments yielded a zonally averaged temperature increase by 5.4ºC (5.4 K) for the higher CO_2 scenario, significantly more than the 3.4ºC gain inferred by the ocean data. Surface temperatures were more seasonally pronounced in the high latitudes above 60º with the greatest overall increase in the Southern Hemisphere (Figure 5-7A and Figure 5-8A). Zonal surface temperatures for the 12.7 × CO_2 experiment remained above 0ºC (273.15 K) throughout the year with the exception of the boreal summer months in the southern latitudes greater than 60º (Figure 5-5 and Figure 5-7). The greatest difference in temperatures between the two experiments occurred during the boreal summer months near 60ºS in which there was an increase of 10.5ºC (10.5 K Figure 5-8C) in response to CO_2 radiative forcing. Zonally averaged temperatures in the tropics increased by 3ºC (3 K) relative to the 4 × CO_2 experiment. In the Southern Hemisphere, the cooling bias compared to climate-sensitive sediments is comparable to Gibbs et al. (2002); however,

simulated temperatures in the 12.7 × CO_2 experiment exceeded 0ºC during the boreal winter months.

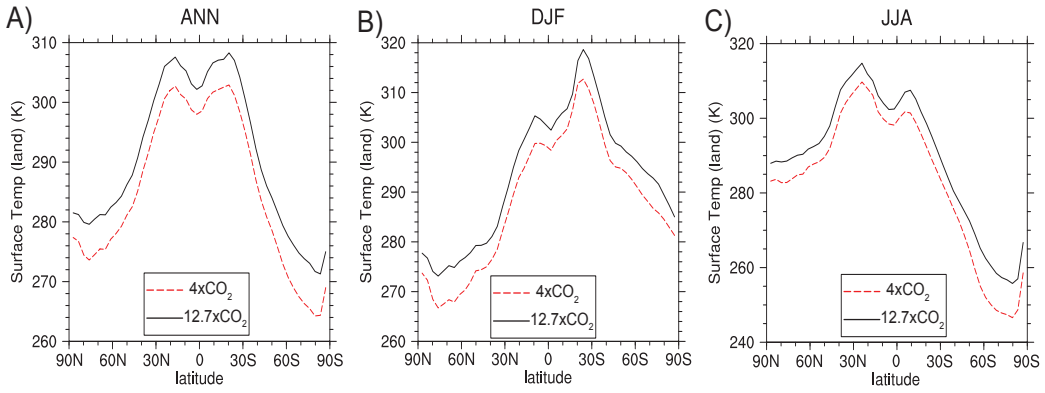

Figure 5-7 Zonally averaged surface temperatures (K) on land for A) annual, B) boreal winter, and C) boreal summer for the 12.7 × CO_2 (Late Permian) and 4 × CO_2 (Middle Permian) CCSM3 simulations.

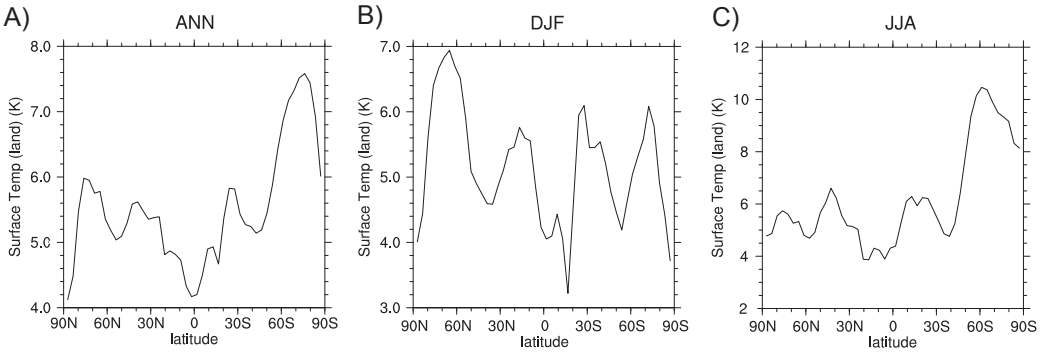

Figure 5-8 The A) Annual, B) boreal winter, and C) boreal summer zonal averages of the difference of surface temperatures (K) on land between the 12.7 × CO_2 and 4 × CO_2 simulations with CCSM3.

Globally, the average precipitation rate increased by 0.2 mm day^{-1} (Table 5-2). The zonally averaged precipitation rate increased with the rise in atmospheric CO_2 levels from 4 × CO_2 to 12.7 × CO_2 relative to preindustrial levels, particularly in the high latitudes and tropics (Figure 5-10A) due to an increase in the intensity of the hydrologic cycle for both evaporation and precipitation. The exception to the general trend of increasing precipitation occurred near 12ºS where the precipitation rate decreased by a zonal annual average of 0.25 mm day^{-1} (Figure 5-11A). The tendency for increased precipitation may be linked to the increased poleward transport of moisture as atmospheric CO_2 concentrations and temperatures increase, as noted in climate change studies (Manabe and Stouffer, 1980; Flato et al., 2013; Zhang et al., 2013).

Similar to the global trend, the zonally averaged precipitation rates over terrestrial regions increased by an annual average of 0.2 mm day^{-1} (Table 5-2). The precipitation rate increase was greatest in the higher latitudes poleward of 60º for both the Northern and Southern hemispheres (Figure 5-11). Continental precipitation rates increased significantly in the high latitudes (> 60ºN) and in the tropics (Figure 5-12). Intensification of the monsoonal cycles is evident by a seasonal increase in precipitation near 30ºN during the boreal summer and 30ºS during the austral summer (Figure 5-12B). The 4 × CO_2 experiment was in disagreement with previous model sensitivity experiments by Gibbs et al. (2002) that suggested a decrease in overall precipitation within the tropical region. This decrease did not occur with the fully coupled CCSM3 experiment, most likely due to the increased sensitivity of the CCSM3 compared to GENESIS 2. Seasonal differences were significant and are discussed in further detail in section 5.6.

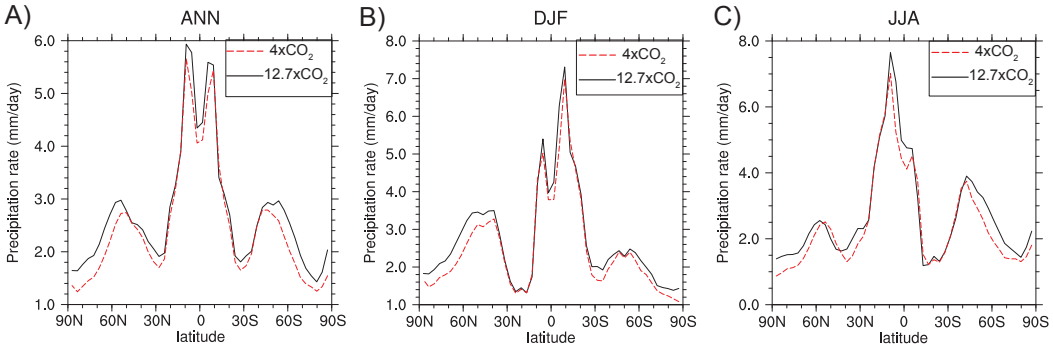

Figure 5-9 Overall zonal-averaged precipitation rates (mm day^{-1}) for A) annual, B) boreal winter, and C) boreal summer simulated by the 12.7 × CO_2 and 4 × CO_2 experiments.

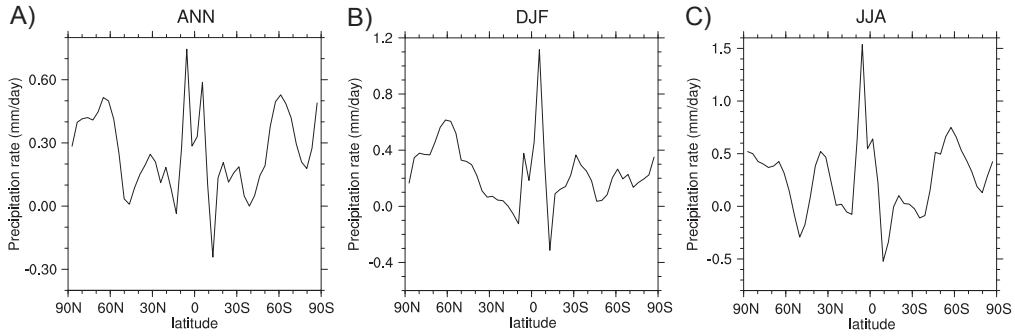

Figure 5-10 The difference in zonal-averaged precipitation rates (mm day^{-1}) between 12.7 × CO_2 and 4 × CO_2 experiments for A) annual, B) boreal winter, and C) boreal summer.

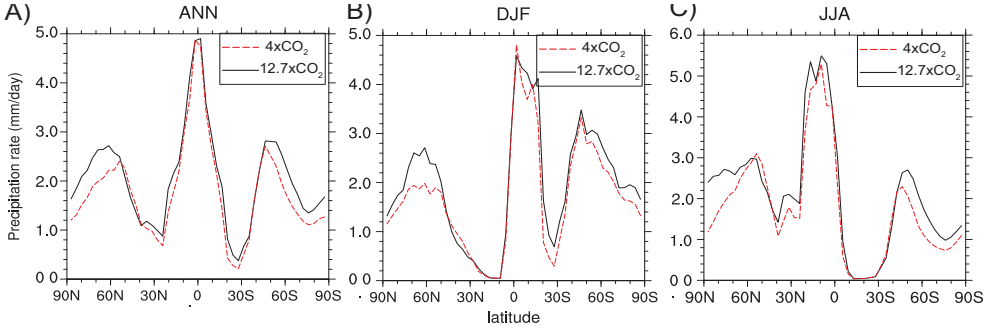

Figure 5-11 Zonal-averaged precipitation rates (mm day^{-1}) over land for A) annual, B) boreal winter, and C) boreal summer.

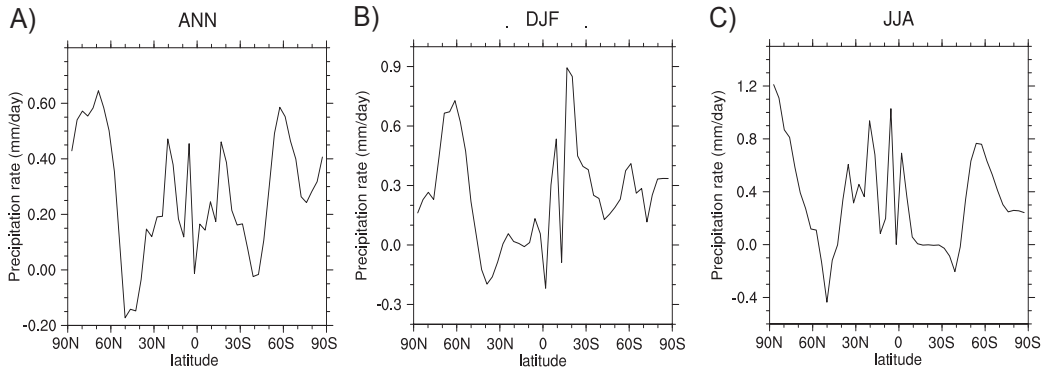

Figure 5-12 The difference in precipitation (mm day^{-1}) between 12.7 × CO_2 and 4 × CO_2 experiments for the land-based zonal averages for A) annual, B) boreal winter, and C) boreal summer.

Simulated water masses using the criteria of Table 5-1 (section 5.1) were compared with climate-sensitive sediments of the Middle Permian for the 4 × CO_2 scenario (Figure 5-13A) and Late Permian climate-sensitive sediments for the 12.7 × CO_2 scenario (Figure 5-13B). The global warming associated with a carbon pulse equivalent to ~4872 Pg C led to the poleward expansion of tropical water masses as illustrated by the change in the tropical zone between Figure 5-13A and Figure 5-13B and as suggested by the temperature contours (Figure 5-13). For the 4 × CO_2 and 12.7 × CO_2 experiments, annual sea surface temperatures are greater than 0ºC (Figure 5-13A and Figure 5-13B, respectively), thus neither polar nor cold temperate conditions are simulated; however, seasonal extremes did occur and those results are discussed in the following subsection (5.5.1). The lack of annual sea-ice cover in the 4 × CO_2 experiment is in conflict with experiments performed by Gibbs et al. (2002) which suggested ice-cover would remain in the highest southern latitudes, yet the CCSM3 sensitivity experiment correlated with the sedimentary record of coal deposit formation in the region.

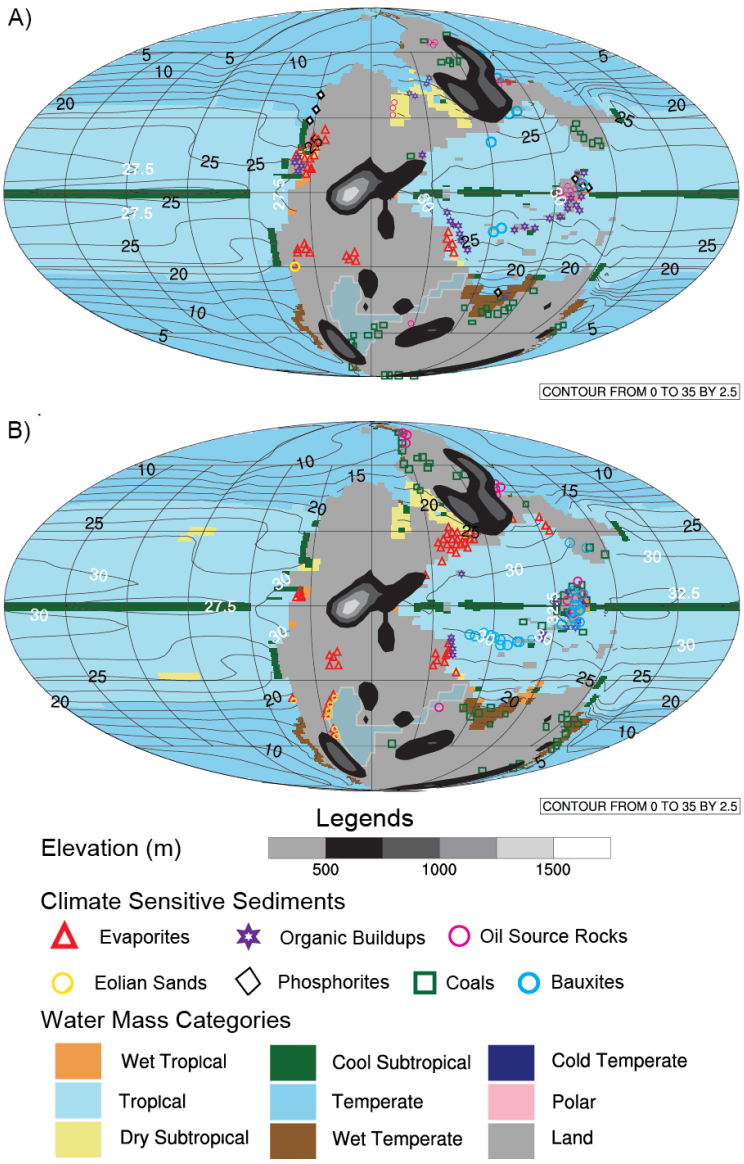

Figure 5-13 Simulated water masses, climate-sensitive sediments and temperatures (contours are in ºC with temperatures that exceed 25ºC highlighted in white) for A) 4 × CO_2 with Middle Permian climate-sensitive sediment markers and B) 12.7 × CO_2 with Late Permian climate-sensitive sediment markers. Circled regions correlate with changes in upwelling from the 4 × CO_2 experiment with blue representing a decrease and red marking an increase.

In order to determine the significance of the changes between the 4 × CO_2 and 12.7 × CO_2 experiments, a t-test was performed to compute whether the means of the two cases were significantly different from each other at each grid point. The t-test was computed using 100 years of averaged model data from each case and the significance level was set at 0.05. T-tests were completed for SST, precipitable water and evaporation minus precipitation rate with regions with 95% confidence level highlighted in the individual figures detailed below.

The simulated annual minimum mean sea surface temperature (SST) for the 12.7 × CO_2 experiment was 3.3ºC, an increase over the minimum temperature of 0.4ºC for the 4 × CO_2 experiment (Figure 5-14A and Figure 5-14B, respectively). Similarly, the

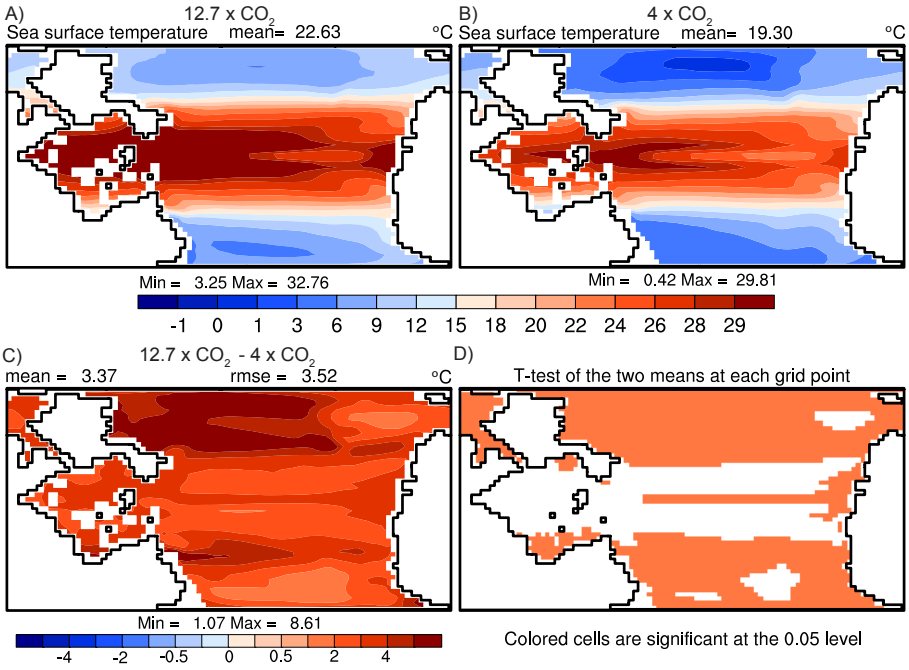

Figure 5-14 Annual mean surface temperatures (ºC) as simulated for A) 12.7 × CO_2 experiment, B) 4 × CO_2 experiment, C) the difference between the 12.7 × CO_2 and 4 × CO_2 experiments and D) t-test signficance between 12.7 × CO_2 and 4 × CO_2 simulations.

simulated annual maximum SST of 32.8ºC for the 12.7 × CO_2 experiment (Figure 5-14A) was a 3.0ºC increase compared to a maximum SST of 29.8ºC in the 4 × CO_2 experiment (Figure 5-14B). Though the mean difference between the two experiments resulted in a 3.4ºC difference, the high northern latitudes experience a greater overall increase in temperatures as illustrated by the dark red shading in Figure 5-14 that suggested temperature increases exceeded 5ºC with a maximum SST increase of 8.6ºC.

In the high latitudes, the simulated extent of wet temperate water masses (Figure 5-13 increased in response to polar warming (Figure 5-15) and lowered surface salinity.

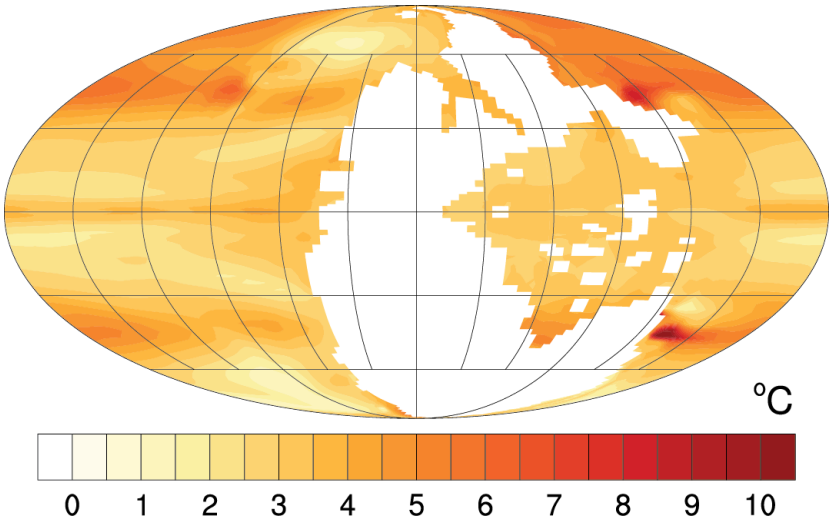

Figure 5-15 Change in potential sea surface temperature between 12.7 × CO_2 and 4 × CO_2. Overall, average temperature increased with a maximum increase exceeding 11ºC.

The decrease in surface salinity is linked to enhanced precipitation (Figure 5-16) and river-associated run-off. Precipitable water (Figure 5-17) increased in the 12.7 × CO_2 experiment (Figure 5-17A) compared to the 4 × CO_2 experiment (Figure 5-17B) particularly within the Tethys region (Figure 5-17C), where monthly rainfall increased by 9

mm to nearly 20 mm. The difference in precipitable water within the atmosphere was globally significant (Figure 5-17D). Simulated dry subtropical regions simulated near 30ºN and 30ºS (Figure 5-13) are highly correlated with Middle to Late Permian evaporitic deposits, particularly within the Tethys Ocean. Comparison of the evaporation rate minus the precipitation rate (Figure 5-18) suggests that the greatest increase in evaporation occurred in the subtropical regions (Figure 5-18C) despite the increase in precipitable water (Figure 5-17).

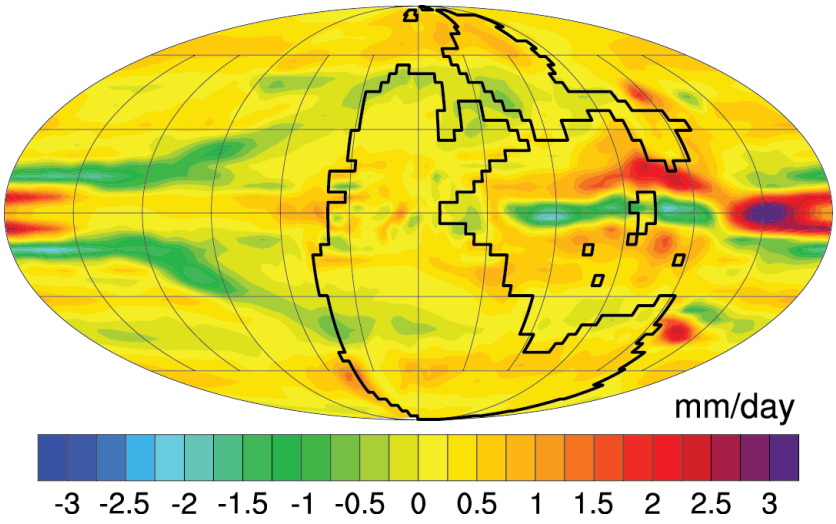

Figure 5-16 Differences in the precipitation rates (mm day^{-1}) between 12.7 × CO_2 and 4 × CO_2 experiments.

Slight changes in upwelling were noted by the cool subtropical water mass marker as tropical regions expanded and temperate zones moved towards the higher latitude polar regions (Figure 5-13). Upwelling was decreased (Figure 5-13B) due to a greater than 1 × 10^{-6} m s^{-1} decline in vertical velocity in five regions between the equator and 30º latitudes (Figure 5-19). Conversely, two regions near 40ºN and 40ºS in latitude

increased in the measured upwelling for the 12.7 × CO_2 experiment (Figure 5-13B) as a result of an Figure 5-19).

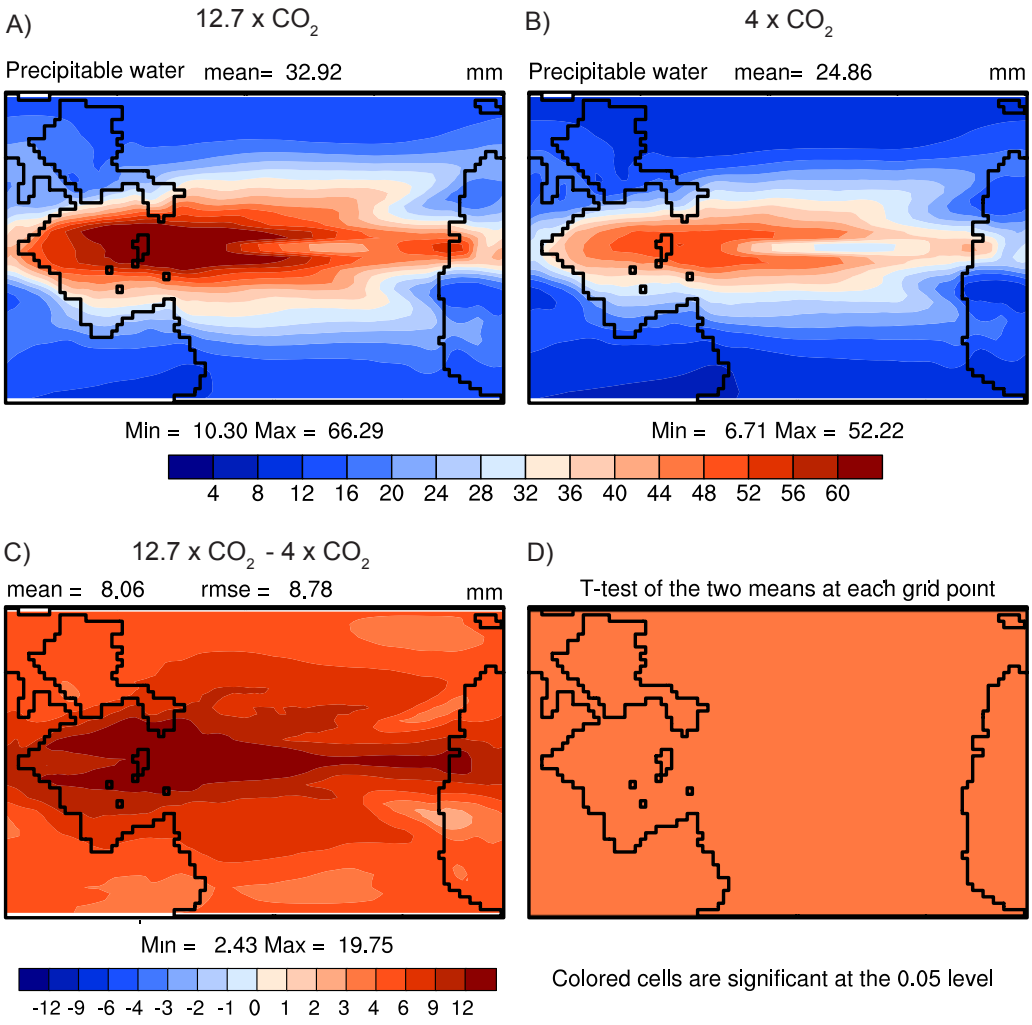

Figure 5-17 Annual mean precipitable water (mm) as simulated for A) 12.7 × CO_2 experiment, B) the 4 × CO_2 experiment, C) the difference between the 12.7 × CO_2 and 4 × CO_2 experiments and D) the areas of significance between 12.7 × CO_2 and 4 × CO_2 simulations as performed by a t test.

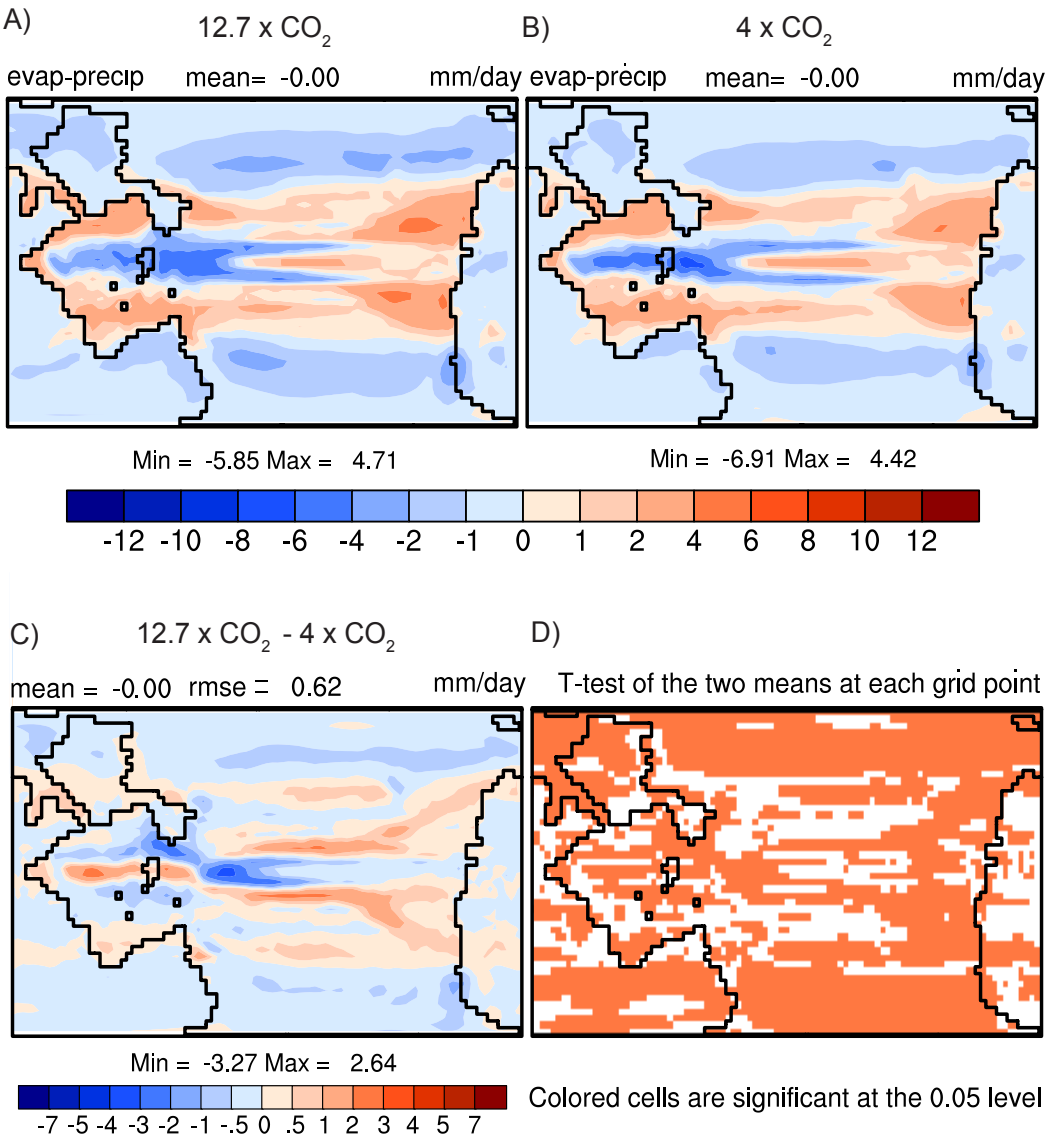

Figure 5-18 Annual mean differences in evaporation rate (mm day^{-1}) minus precipitation rate (mm day^{-1}) as simulated for A) the 12.7 × CO_2 experiment, B) the 4 × CO_2 experiment, C) the difference between the 12.7 × CO_2 and 4 × CO_2 experiments and D) the areas of significance between 12.7 × CO_2 and 4 × CO_2 simulations as performed by a t-test.

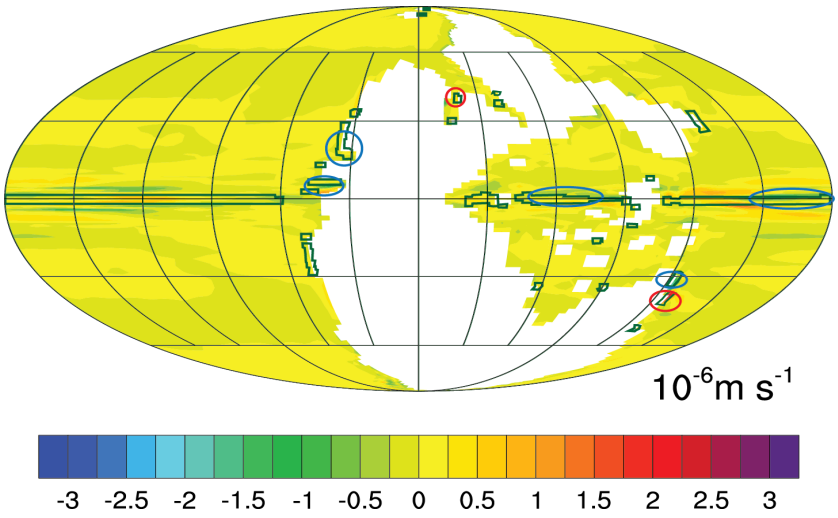

Figure 5-19 The difference in surface vertical velocities between 12.7 × CO_2 and 4 × CO_2 experiments. Regions circled correspond to simulated change in the upwelling reflected in Figure 5-13B (upwelling regions outlined in dark green). Blue circles correspond to decreased vertical velocity whereas areas circled in red reflect an increased in vertical velocity. Circled regions correlate with their corresponding area in Figure 5-13.

The differences in Ekman-induced upwelling (w_E) patterns were primarily linked to changes in surface wind stress (τ):

$$w_E = \text{rot}\ \tau\ /(f\ \rho) \qquad \text{Eq. 5-1}$$

where ρ denotes the density and f =2 Ω sin φ is the Coriolis parameter with Earth rotation rate Ω = 7.29 10^{-5} radians s^{-1} as function of latitude φ.

5.6 Seasonal variation of water masses

Seasonal fluctuations between the 12.7 × CO_2 and 4 × CO_2 simulations revealed a greater variation in water masses. The 4 × CO_2 experiment suggested the presence of

cold temperate conditions within the northern high latitudes during the boreal winter months (Figure 5-20A) that were not present in the 12.7 × CO_2 experiment (Figure 5-20B). A polar region surrounded by a small cold temperate water mass developed during the austral winter months off the south-eastern shorelines of Pangea between 45ºS and the southern pole (Figure 5-21A), whereas only a small area of cold temperate water masses formed near 60ºS in the 12.7 × CO_2 experiment (Figure 5-21B). The simulated boreal winter minimum mean sea surface temperature (SST) for the 12.7 × CO_2 experiment was 4.3ºC, an increase over the minimum temperature of -0.9ºC for the 4 × CO_2 experiment (Figure 5-22A and Figure 5-22B, respectively). Likewise, the simulated annual maximum SST of 34.0ºC for the 12.7 × CO_2 experiment (Figure 5-22A) indicated a 3.2ºC increase from the maximum SST of 30.8ºC in the 4 × CO_2 experiment (Figure 5-22B). Although the mean difference in SST between the two experiments resulted in a 3.4ºC difference, the high northern latitudes sustained a greater overall increase in SST in both the boreal winter and summer seasons, as illustrated by the dark red shading in Figure 5-22C and 5-23C. The change between the lower to the higher CO_2 scenerios highlighted by the dark shading in Figure 5-22C inferred the increased SST >5ºC was primarily confined to the Northern Hemisphere near the poles and in the mid-latitudes. Where the SST increased >5ºC between the 12.7 × CO_2 and 4 × CO_2 experiments, there was also an increase in the development of evaporites recorded in the climate-sensitve sediments between the Middle and Late Permian along the eastern mid-latitudes coastal regions of Pangea. Though the seasonal SST comparisons between the 12.7 × CO_2 and 4 × CO_2 experiment yielded an overall increase in temperatures, the increases demonstrated within the equatorial regions were not statistically significant (Figure 5-22D and Figure 5-23D).

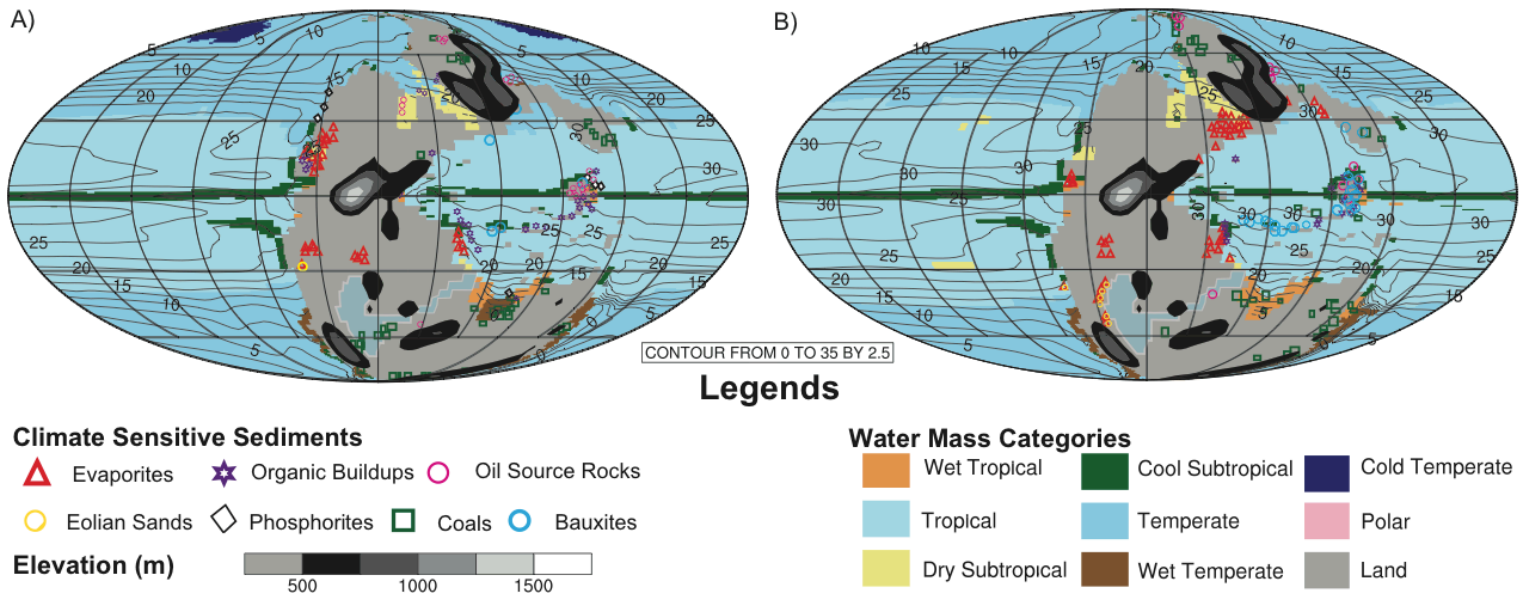

Figure 5-20 Simulated water masses, climate-sensitive sediments and temperatures (temperature contours are in ºC) during the boreal winter months of December, January and February for the A) 4 × CO_2 with Middle Permian climate-sensitive sediment markers and B) 12.7 × CO_2 with Late Permian climate-sensitive sediment markers.

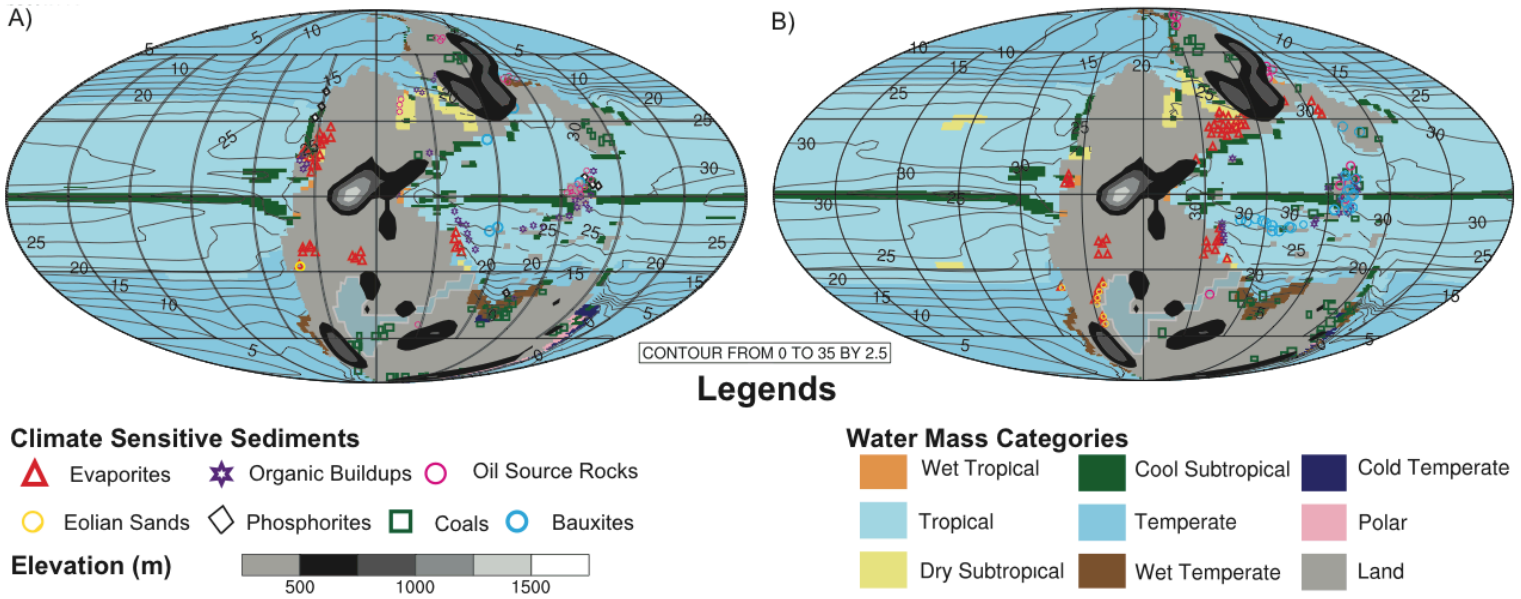

Figure 5-21 Simulated water masses, climate-sensitive sediments and temperatures (temperature contours are in ºC) during the boreal summer months of June, July and August for the A) 4 × CO_2 with Middle Permian climate-sensitive sediment markers and B) 12.7 × CO_2 with Late Permian climate-sensitive sediment markers.

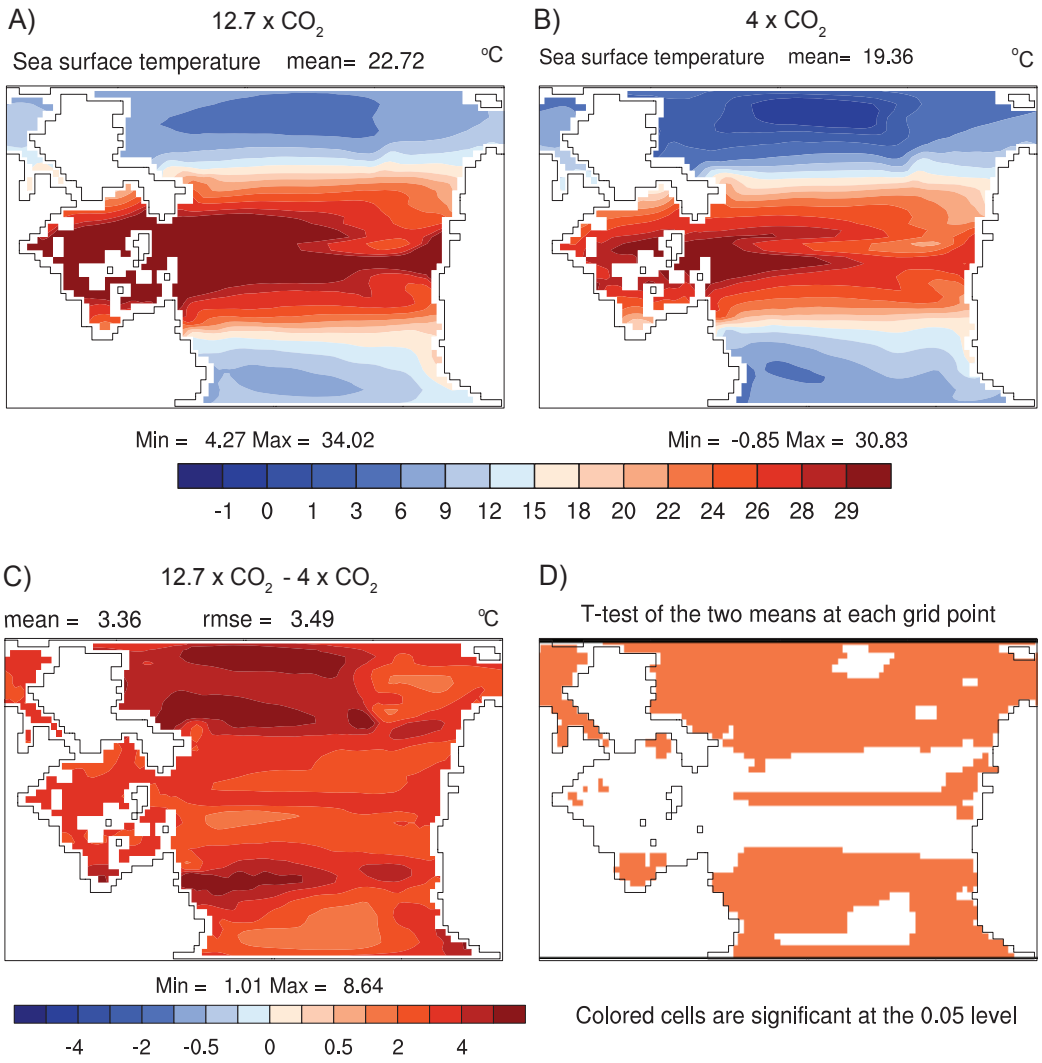

Figure 5-22 Boreal winter mean surface temperatures (ºC) as simulated for A) 12.7 × CO_2 experiment, B) 4 × CO_2 experiment, C) the difference between the 12.7 × CO_2 and 4 × CO_2 experiments and D) the areas of significance between 12.7 × CO_2 and 4 × CO_2 simulations as performed by a t-test with a 95% confidence interval.

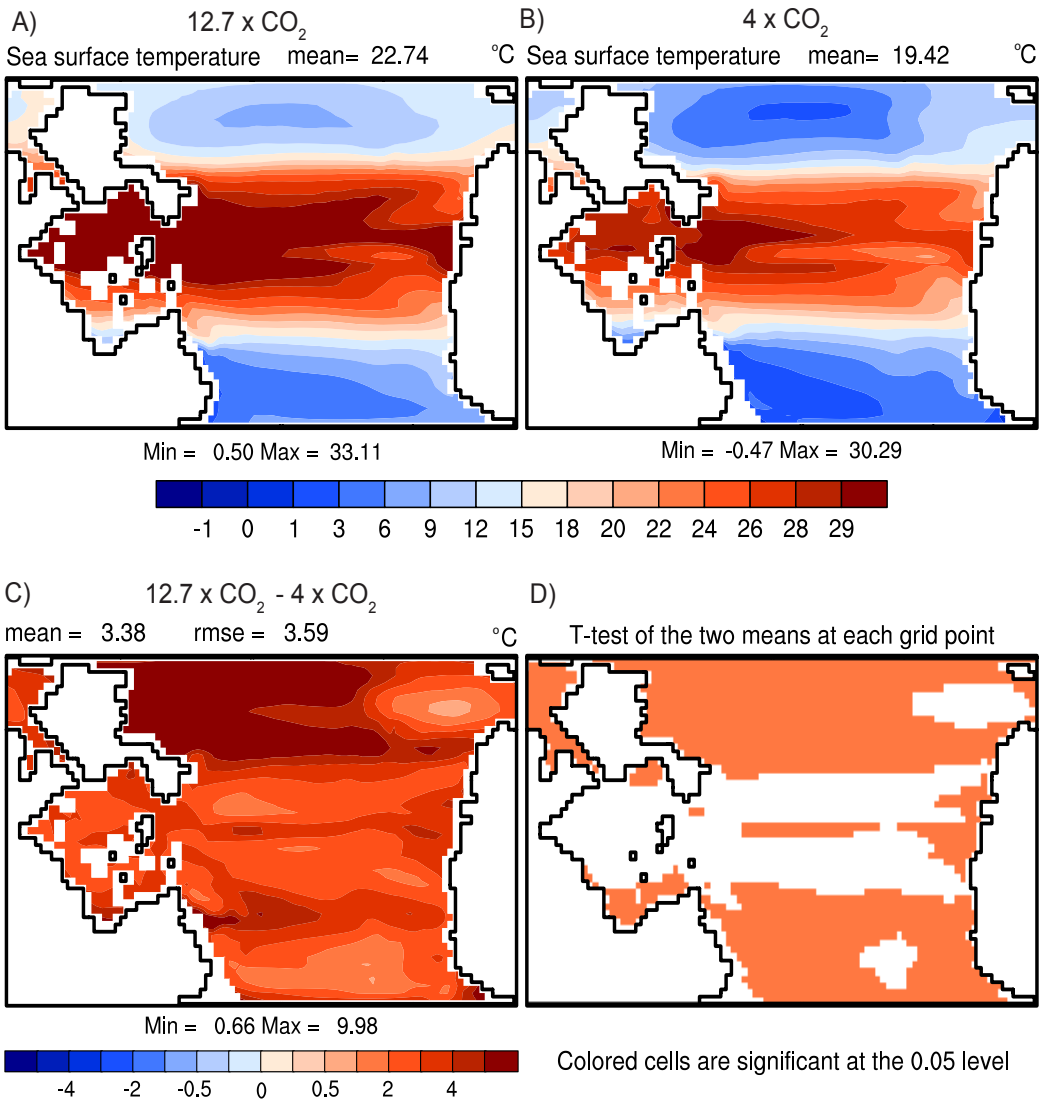

Figure 5-23 Austral winter mean surface temperatures (ºC) as simulated for A) 12.7 × CO_2 experiment, B) 4 × CO_2 experiment, C) the difference between the 12.7 × CO_2 and 4 × CO_2 experiments and D) the areas of significance between 12.7 × CO_2 and 4 × CO_2 simulations as performed by a t-test with a 95% confidence interval.

Ekman-induced upwelling or downwelling (eq. 5-1) alters the nutrient supply and thus the pattern of primary productivity. The mean Ekman transport within the surface layer of the ocean (< 200 m in depth) is 90º towards the right of the wind direction in the Northern Hemisphere and 90º to the left in the Southern Hemisphere. Seasonal upwelling patterns illustrated in Figure 5-20 and Figure 5-21 (i.e., cool subtropical water masses) were primarily affected by the change in the magnitude of surface stress between the 12.7 × CO_2 and 4 × CO_2 experiments (Figure 5-24 and Figure 5-25). Surface stress patterns were strongest in the northern latitudes above 45º, with an isolated region of high surface stress (>0.2 N m^{-2}) located off the northern coastal region within the Paleo-Tethys Basin (Figure 5-24A and Figure 5-24B), which correlated well with the cool subtropical zones depicted in Figure 5-20 for the boreal winter months. A weakening of the polar easterly winds resulted in the strong core of the westerly winds to be located farther north in latitude in the 12.7 × CO_2 experiment, modifying wind surface stress (Figure 5-24C). The simulation suggests that the movement of the main core of the westerly winds caused a northward shift in upwelling patterns when compared to the 4 × CO_2 experiment (Figure 5-20B). A comparison of the 12.7 × CO_2 and 4× CO_2 experiments revealed a similar pattern in the Northern Hemisphere as well as the Southern Hemisphere during the austral winter months (Figure 5-25A and Figure 5-25B). The high latitudes in both hemispheres had increases exceeding 0.06 N m^{-2}. A decrease in surface stress did occur at the mid-latitudes that was particularly prominent in the Southern Hemisphere between 30º - 60ºS, with a reduction of force exceeding 0.10 N m^{-2} (Figure 5-25C). An increase of 0.02 N m^{-2} in surface stress (Figure 5-25C) correlated well with the increase of upwelling within the northern Paleo-Tethys region depicted by the cool subtropical zone in Figure 5-21B.

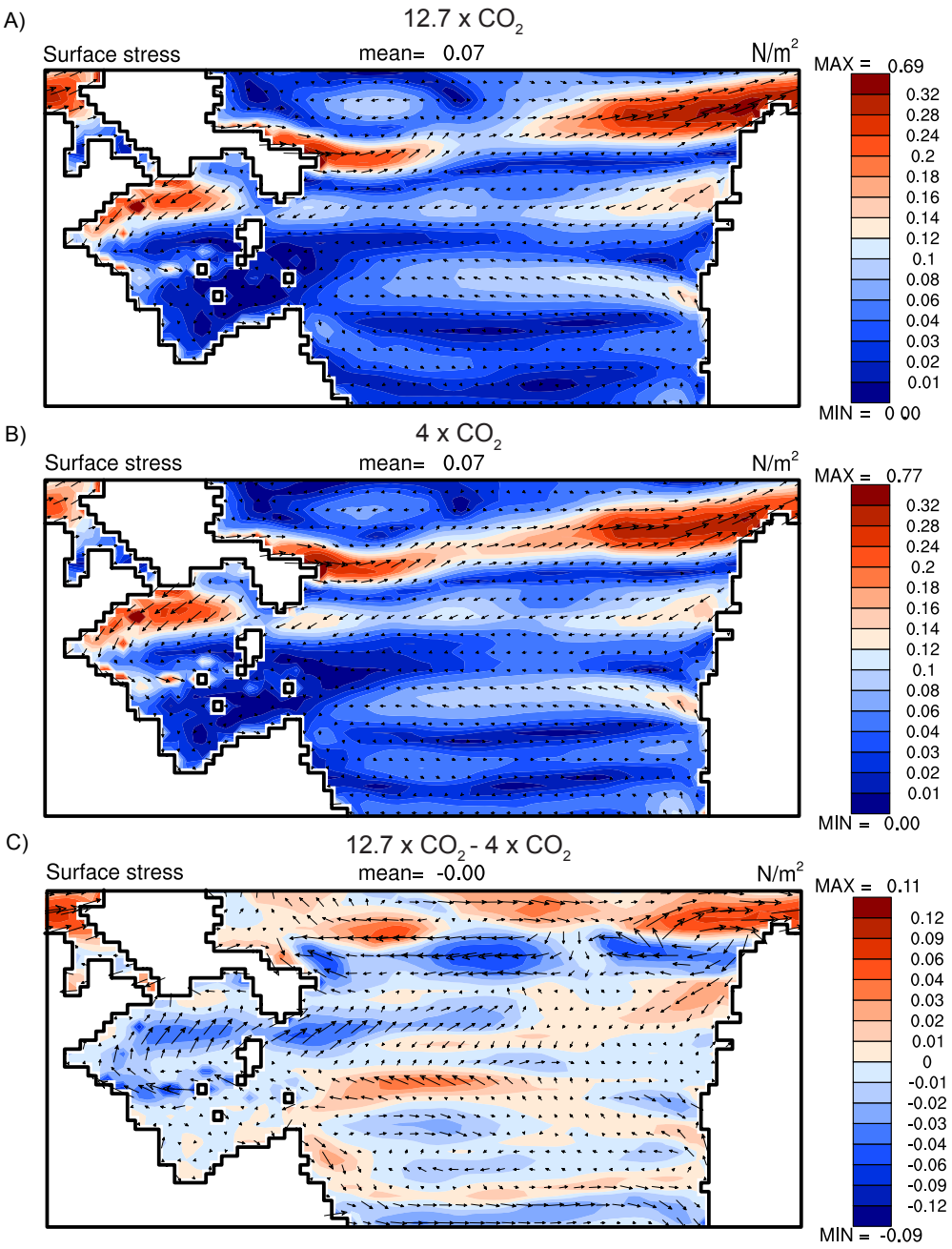

Figure 5-24 Boreal winter surface stress (N m^{-2}) for A) 12.7 × CO_2 experiment, B) 4 × CO_2 experiment and C) difference between 12.7 × CO_2 and 4 × CO_2 experiments.

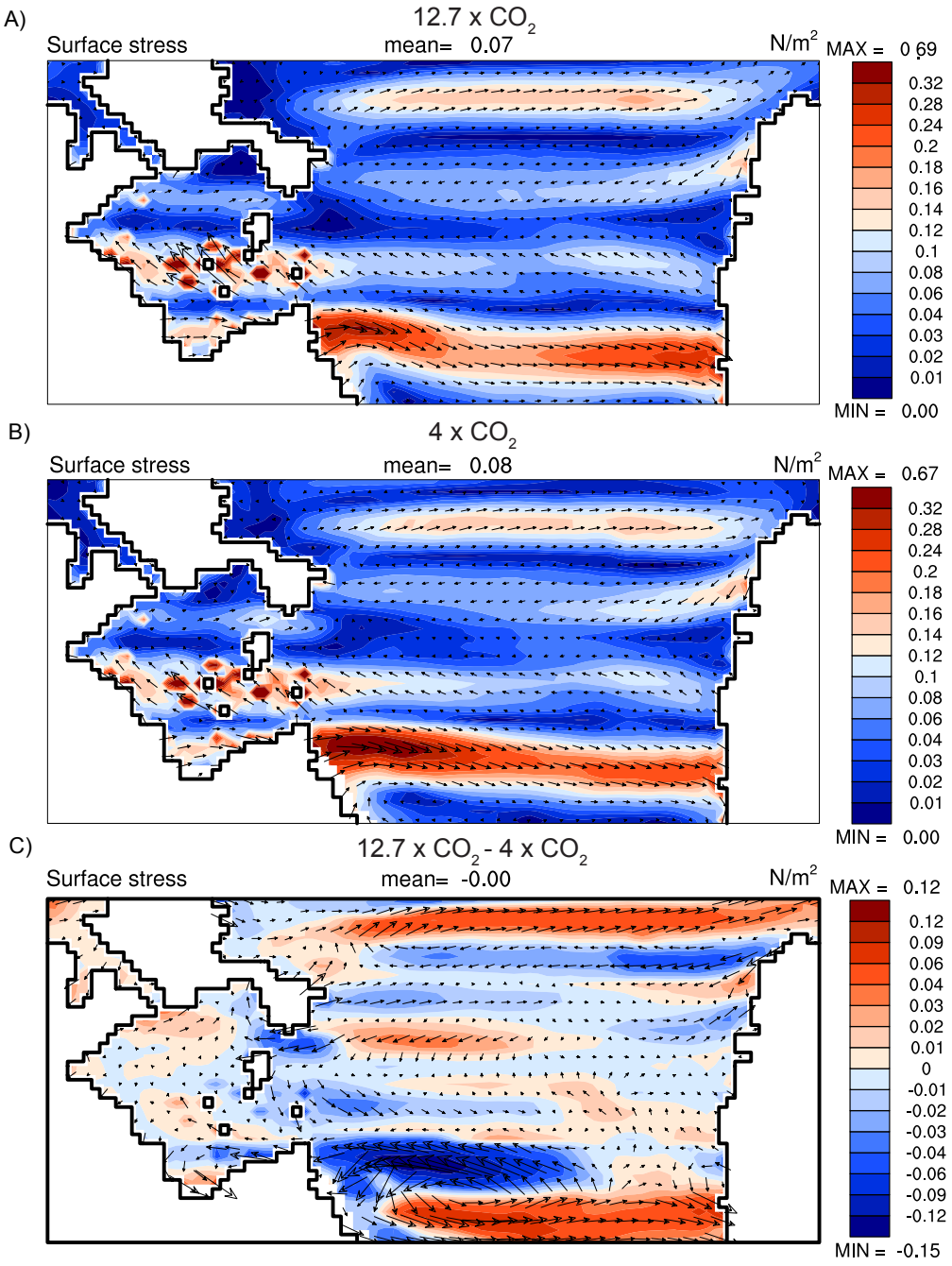

Figure 5-25 Austral winter surface stress (N m^{-2}) for A) 12.7 × CO_2 experiment, B) 4 × CO_2 experiment and C) difference between 12.7 × CO_2 and 4 × CO_2 experiments.

5.7 Discussion

The climate patterns of the fully coupled atmosphere ocean GCM 4 x CO_2 experiment of this study, albeit small differences in the radiative forcing, were comparable to previous simulations with atmospheric GCMs (Kutzbach and Ziegler, 1993; Gibbs et al., 2002; Winguth et al., 2002) with regional discrepancies, particularly with the simulated warmer poleward currents compared to studies without dynamic ocean component. Gibbs et al. (2002) suggested that poleward ocean-heat transport might have been underestimated in atmospheric GCMs that are not coupled to a dynamic ocean model thus leading to a polar cold bias compared to the reconstructed climate.

The 4 × CO_2 experiment (Figures 5-13A, 5-20A and 5-21A) was compared to climate-sensitive sediments for the Middle Permian (Guadalupian Epoch, ca. 272.3-259.8 Ma) that included coals, eolian sands, evaporites, oil source rocks, organic buildups, and phosphorites compiled from Ziegler et al. (1997; 1998) and bauxites from Boucot et al. (2013). The 4 × CO_2 experiment rendered results corresponding with climate-sensitive sediments established during the Middle Permian. Wet tropical water masses correlated with the formation of bauxites, organic build-ups, and oil source rocks off the eastern coast of the South China block. Wet temperate zones correlated well with formation of coals in the Southern Hemisphere. Northern Hemisphere coals are documented in Siberia, west of the newly formed Urals and on the North China block influenced by seasonal advection moisture that could support a wet environment. However, coals in the North China block were in a region for which the model suggested neither arid nor humid conditions; therefore, coal formation was not supported in the model, which might be related to mountain ranges not being resolved. Tropical and cool subtropical water masses were associated with organic build-ups, oil source rocks and some phosphorites within the Tethys region and off the west coast of Pangea in the Northern Hemisphere.

Tropical water masses corresponded well with Middle Permian simulations conducted by Winguth et al. (2002), and temperature profiles performed by Gibbs et al. (2002). Cool subtropical water masses were not well correlated with the geological record of phosphorites, which are considered indicative of ocean upwelling. The discrepancy is likely due to the low resolution of the model and the model's inability to resolve coastal processes. Dry subtropical water masses correlated well with evaporites and eolian sands with the exception of the inland sea between Siberia and Greenland where dry subtropical water masses were simulated, but evaporitic deposits were not established until the Late Permian. The discrepancy between the climate model and data was likely due to an insufficient freshwater flux in the region. Inland evaporite deposits and eolian sands show a relationship with arid regions in the biome study (see Chapter 6).

The climate pattern of the simulation with an atmospheric CO_2 concentration of 12.7 × CO_2 (Figures 5-13B, 5-20B, and 5-21B) was in general agreement with the reconstructed Late Permian (Lopingian ca. 259.8-252.17 Ma) climate-sensitive sediments from Ziegler et al. (1998) and Boucot et al. (2013) . The wet tropical water masses simulated in the12.7 × CO_2 experiment were primarily formed within the equatorial region with a notable increase near 40ºS in the Neo-Tethys Basin when compared with the 4 × CO_2 experiment. The expansion of regions depicted by the wet tropical zone is due to the increase in SST. Coal formation was documented as diminishing within the Neo-Tethys basin when compared with the Middle Permian geological record. This decrease is insinuated by the change from wet temperate to wet tropical water masses on the outer corners of the Neo-Tethys Basin with the 12.7 × CO_2 experiment. The wet temperate water masses are associated with the geological records of coal deposits along the high latitudes of the southeastern section and northwestern section of Pangea. Wet temperate conditions were more prevalent along the coastal regions due to increased rainfall and

runoff conditions. In the 12.7 × CO_2 experiment, tropical water masses expanded poleward in both hemispheres by 10º in latitude relative to the 4 × CO_2 experiment. Within the tropical zone, an annual averaged SST of ≥30ºC in the Paleo-Tethys Basin corresponded with an increased occurrence of bauxites on the South China block as well as Cimmerian block. Average simulated sea surface temperatures in the tropics are ~33ºC for 12.7 × CO_2 and ~30ºC for 4 × CO_2, both falling within the oxygen isotope temperature range of 21ºC to 36ºC predicted for the Late Permian by Sun et al. (2012). However, neither sensitivity experiment reaches the hypothesized temperatures of >38ºC suggested by Sun et al. (2012) for the Early Triassic. An increase in the evaporation rate for the northern Paleo-Tethys region accounted for the decrease in bauxite formation and the increase in evaporite formation, but these fluctuations were not recorded by a change in water masses. Simulated areas of upwelling (cool subtropical) exceeded the area of reconstructed climate-sensitive sediments, as geological evidence is scarce due to the subduction and erosion of Permian sedimentary deposits. Dry subtropical water masses located near the shore of Laurasia at 30ºN in the 12.7 × CO_2 experiment were in agreement with large Permian evaporite deposits. A decrease in precipitation in the southwestern region of Pangea (Figure 5-16) between 30-60ºS correlated well with the increased occurrence of evaporites and eolian sands between the Middle and Late Permian reconstructions.

5.8 Conclusion

Overall, the model simulations are in reasonable agreement with the climate-sensitive sediments available. The model simulations were particularly well matched with the distribution of coals. Difficulties with the predictions occurred near coastal regions and where smaller islands were not resolved within the model due to the coarse resolution.

The climate zones predicted by the sensitivity experiments were within the range of estimated paleo-oceanic temperatures for the Late Permian (Joachimski et al., 2012; Sun et al., 2012) but did not reach the extremes estimated for the Early Triassic as determined by oxygen isotopes.

Chapter 6

On the Distribution of Land Vegetation in Response to Climate Change near the Permian-Triassic Boundary

6.1 Introduction to Permian-Triassic vegetation

The Permian-Triassic mass extinction is characterized by a high loss of marine and terrestrial species with more than 90% of marine and 70% of the terrestrial species became extinct (Erwin, 1994; Erwin, 2006; Retallack, 1995). In the following sections, focus is given on the flora and fauna on Pangea that underwent a remarkable reorganization during this period. The climatic transition from a glaciated coldhouse during the Early Permian to an ice-free hothouse in the Late Permian produced significant changes in the ecosystem on land. Carboniferous plants were replaced by a more Mesophytic flora and gymnosperm pollen gave way to new, arid-resistant pollen (Erwin, 1994). Seasonal fluctuation of temperatures was likely reduced with a transition to warmer polar climate because of a reduced equator-to-pole gradient. However, even during the Late Permian, the interior of Pangea was likely characterized by a dry continental climate comparable to present-day central Asia (Kutzbach and Ziegler, 1993; Parrish, 1993). Temperature extremes in excess of 35ºC for a prolonged period, together with the arid conditions, may have led to C_3 plants becoming severely stressed (Sun et al., 2012) and enhanced the likelihood of widespread fires (Hudspith et al., 2014). The prevalence of mutant pollen tetrads during the latest Permian is construed as possible evidence of ozone destruction related to volcanic emissions (Visscher et al., 2004; Black et al., 2012). Nevertheless, reconstruction of the global climate of the Late Permian has been a challenge with limited details on the duration and timing of some of the extinction events (Erwin, 1994).

Previous late Paleozoic climate-biome model studies (Ziegler, 1990; Kutzbach and Ziegler, 1993; Rees et al., 1999; Rees et al., 2002) have focused on the Early Permian (Sakmarian) and Middle Permian (Wordian). Changes in terrestrial environment inferred from fossil flora (Rees et al., 1999; Rees et al., 2013) can be compared with comprehensive climate models to identify boundary conditions (e.g. radiative forcing, topography, etc.) and processes that contributed to climate change (Ziegler, 1990; Rees et al., 2002; Winguth et al., 2002). For example, the rise in greenhouse radiative forcing and the associated transition from the ice-house world into a hot-house world led to significant changes in the floral patterns, particularly in the high latitudes (Montanez et al., 2007).

A climate-based biome scheme that was developed by Walter (1985) for modern day floras is useful to infer climatic changes from variations of Permian phytogeographic pattern (Ziegler, 1990; Kutzbach and Ziegler, 1993). There is a general agreement with reconstructed biome and climate simulations for tropical regions and mid-latitudes, but a cold bias was simulated for polar regions (Kutzbach and Ziegler, 1993), particularly for Gondwanaland. This discrepancy may be partially linked to a lack of an interactive dynamical ocean as part of the climate model as well as the coarse resolution of the climate model.

Rees et al. (1999; 2002) expanded upon Ziegler's earlier work (1990; 1997) and combined the biome scheme with climate models for the Early to Middle Permian. Reconstructed maps based on climate-sensitive sediments and flora (Figure 6-1) were compared with output from the GENESIS climate model with two distinct prescribed atmospheric CO_2 concentrations (Rees et al. 2002) ; scenarios with a CO_2 radiative forcing equivalent to a four times and eight times preindustrial CO_2 concentration. The

better fit, when compared to the reconstructed biome patterns of the Wordian (ca. 265 Ma), was performed by the 8 × CO_2 scenario with a warmer polar climate.

The findings of Rees et al. (2002) have been supported by a more recent study of Montenegro et al. (2011) who inferred that the global vegetation patterns had not changed significantly between the Middle and Late Permian.

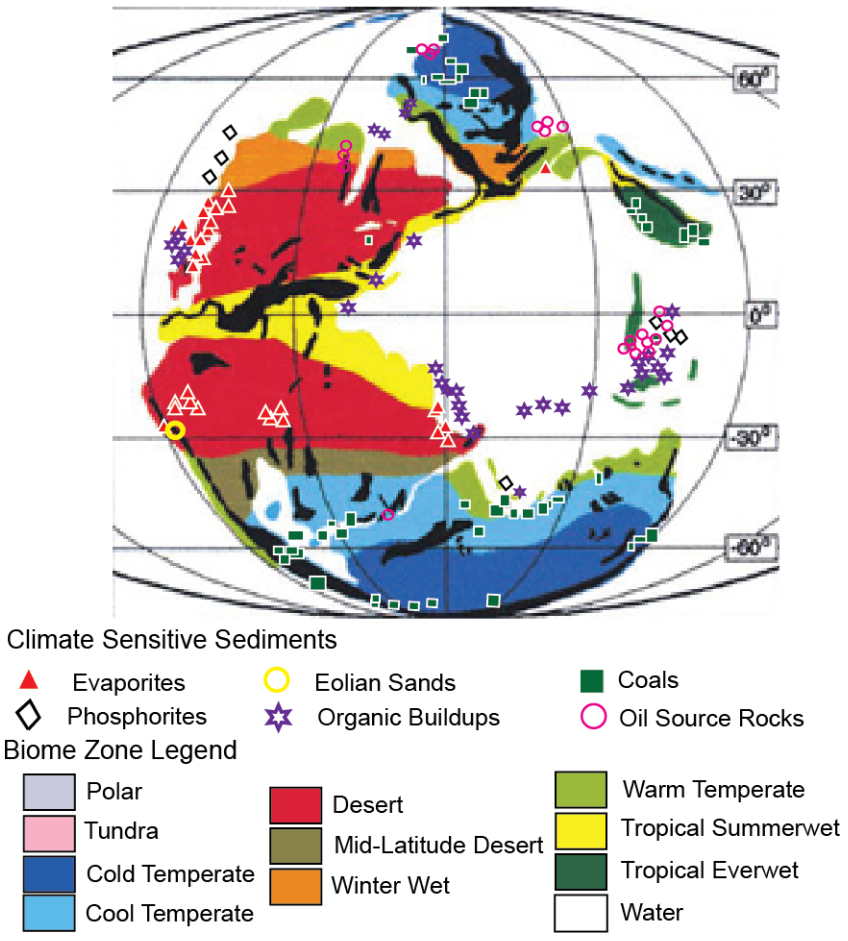

Figure 6-1 Wordian data-derived biomes from Rees et al. (1999) with Middle Permian climate-sensitive sediments from Ziegler et al. (1998) superimposed onto map.

6.2 Biome classification scheme

Ziegler (1990) adapted present-day climatically defined biomes originally developed by Walter (1985) and applied them towards different stages of the Permian. Walter's vegetation classification (Walter, 1985) divided the world into nine biome schemes based on annual precipitation and temperature patterns. These patterns were determined from a survey of approximately 8,000 meteorological stations and were tested using a digital database of ground-based stations along with a satellite-derived vegetation index (Lottes and Ziegler, 1994; Ziegler et al., 2003). Walter's precipitation schemes are broken down into five categories with the end members consisting of deserts receiving less than 250 mm of precipitation a year and the tropics getting more than 2000 mm of rain annually. Temperature ranges, soil and vegetation types are considered in order to distinguish regions into the nine different biomes. Ziegler (1990) expanded upon Walter's biome scheme by comparing present-day vegetation and soils with possible Permian counterparts in order to develop an idealized biome model of the Permian. The following biome classification scheme used in this study is adapted from Ziegler (1990) and Rees et al. (1999; 2002). A summary of climate zones selected for the biomes is listed below (see also Table 4):

Biome 1: Tropical Everwet: Regions of tropical rainforest where temperatures consistently exceed 20º (mean = 26º - 29ºC) and rainfall is heavy (> 20 mm per month). Conditions such as these tend to occur along the equator and are typically influenced by the ITCZ. Trade winds can also bring warm moist air up east-facing coasts expanding tropical zones (Ziegler, 1990; Barry and Chorley, 1982). Mapping the biome can be challenging as some of the plants typical of tropical zones can be found as high as 50º latitude. Multistoried trees dominate the tropics; however, lianas (woody vines) are a better indicator as 90% of the species are confined to the tropics (Ziegler, 1990).

Morphological features that are likely to be preserved would include leaves with drip-tips and thick cuticles as well as logs with large plank-buttresses. Soils have been described as ferralitic but peat soils may also form in sandy substrates where water levels are constant (Ziegler et al., 1987).

Biome 2: Summerwet: Regions are characterized by a variety of vegetation ranging from deciduous forest to savannas that typically occur along the margins of the ITCZ. This zone serves as a transitional zone between tropical and desert regions and is prone to dry seasons. Transitions between everwet and summerwet tend to be distinct possibly due to fire activity or heavy grazing in biome 2. Characteristic leaves tend to be large yet thin deciduous leaves and may have drought-resistant type leaves and thorns.

Biome 3: Desert: Evaporation consistently exceeds precipitation in these regions. In the present day, desert zones typically occur between 15º and 32ºN where the dry air of the descending branch of the Hadley circulation reaches the surface. Plants tend to be xerophytes (drought resistant) and succulents; however, preservation is poor in desert regions and these areas are usually identified by the presence of evaporite deposits or eolian sands.

Biome 4: Winterwet: Regions with this biome are unique as their development is related to the polar front and associated extratropical cyclones. In the modern world, winterwet biomes are referred to as Mediterranean climates and are limited to the western margins of continents along latitudes of 32º-38º North and South. Common vegetation includes sclerophyllous evergreen forests and schlerophyll shrubs that have characteristically small, leathery leaves. Annual plants, that germinate or die within a year or season, are common with short breeding periods correlating with rapid evolution (Raven, 1973). Preservation is limited in these regions with very little peat accumulation.

Biome 5: Warm Temperate: Rainfall in the region is typically well distributed through the year due to winter frontal systems as well as summer convective systems carrying precipitation inland. Warm temperate climates support evergreen forests containing both angiosperms and gymnosperms though the forests are not as productive as tropical rainforests due to cooler, seasonal temperatures. Soils are characteristically yellow or red podzols with locally developed peat swamps (Ziegler et al., 1987).

Biome 6: Cool Temperate: This biome is prone to hard frosts and cold winters. Angiosperm dominated forests will shed their leaves and for a short period during the spring, geophytes will thrive before the trees regain their foliage. The vegetational boundaries are gradational for biomes 5 to 7 over several hundred kilometers. Peat bogs may occasionally form in the region.

Biome 7: Mid-latitude Desert: Rainfall is scarce for this biome (< 20 mm a month) and vegetation includes various grasses with some shrubs. Soils are chernozems or sierozems with evaporites quite common to the regions despite cooler temperatures than those found in the desert biome. In present-day climate zones, this biome is only found in a coastal region in Argentina due to the strong westerlies that have released their moisture on the windward side of the Andes. The winds are heated adiabatically as they descend into Argentina. This seasonal response is common of narrow landmasses with an ocean-dominated climate that is exhibited by the above vegetative patterns.

Biome 8: Cold Temperate: This zone only occurs in the Northern Hemisphere in the present-day and is limited by a short one to four month growing season. Evergreen conifer forests are common. Taiga, widely spaced trees with ground cover consisting of mosses and lichens, is also prevalent in the region. Soils tend to be podzols and peat bogs are well developed.

Biome 9: Arctic/Tundra: The region does not contain trees due to the very short (one month) growing season. Tundra vegetation, including sedges, grasses, mosses, lichens and forbs can be found in the region with occasional shrubs.

Biome 10: Glacial: This biome does not contain vegetation but is considered well represented in the geological record by the formation of tillites.

6.3 Present-day biomes

Present-day observed climate zones were computed using two-meter surface air temperature and precipitation from the NCEP/DOE Reanalysis II (Kanamitsu et al., 2002). For arid regions, monthly precipitation was considered to be <20 mm per month, in agreement with Ziegler (1990) and Walter and Breckle (2002), whereas Rees et al. (1999; 2002) used a higher value of 40 mm per month based on perceived approximation necessary to stimulate biotic productivity. Walter (2002) suggested that desert regions must meet an annual requirement of no more than 250 mm of precipitation annually; therefore, using a limit of 20 mm per month was a better fit than that of 40 mm per month used previously by Rees et al. (1999; 2002). Temperature ranges were set to record the average for months over 10ºC as simulated in the experiments by Rees et al. (1999; 2002). In addition to the biome classifications listed in section 6.2, it was necessary to add another biome classification (biome class 10) to distinguish the difference between tundra (biome class 9) and regions with constant ice/snow cover as previously done by Ziegler (1990). Table 6-1 outlines temperature and precipitation limits set for the individual biomes used in the sensitivity experiments. Table 6-1 was modified from Ziegler (1990) where column one is derived from Ziegler (1990), column two from Walter (1985), column three from Ziegler et al. (1987), columns four and five from Rees et al. (2002), and column six re-created by Ziegler (1990) from Walter (1985) and Eyre (1968).

Table 6-1 Climatic parameters for present-day biomes modified from Ziegler (1998).

	Climatic Descriptor	Present-day Vegetation	Precipitation Systems	Temperature > 10ºC	Precipitation ≥ 20 mm	Latitude
1	Tropical Everwet	Evergreen tropical rain forest	Tropical diurnal near the coast or equatorial near the ITCZ	12	11-12	Up to 25º and 10º ± 7º
2	Summerwet	Tropical deciduous forests or savannas	Subtropical during summer monsoon or tropical during summer extension of ITCZ	12	4 -10	Up to 25º and 15º ± 5º
3	Desert	Subtropical desert vegetation	Winter rains limited; descending limb of Hadley cell	11-12	0-3	32º ± 4º
4	Winterwet	Sclerophyllous woody plants	Winter frontal	11	5-10	38º ± 5º
5	Warm Temperate	Temperate evergreen forests	Winter frontal, summer convective	11	11-12	46º ± 14º and 36º ± 2º
6	Cool Temperate	Broadleaf deciduous forests	Winter frontal, summer convective	5-6	5-10	58º and 36º ± 2º
7	Mid-latitude Desert	Steppe to desert with cold winters	None due to distance or because of rain shadows	3-10	0-5	51º ± 2º
8	Cold Temperate	Boreal coniferous forests (taiga)	Summer frontal	2-4	2-12	~ 58º to 66º
9	Arctic/Tundra	Tundra (treeless)	Some summer frontal	0-1	--	~ 60º to 70º
10	Polar/Glacial	Ice sheets	Polar air masses	12 mo. < 0º	--	+ 70º

Simulated present-day and Permian biomes used monthly temperature and precipitation ranges listed in Table 6-1. Biomes simulated with CCSM3 generally agree with those of the NCEP reanalysis. However, there is a noticeable northern high-latitude cold bias (Figure 6-2) of 4.6ºC to 7.4ºC (4.6K to 7.4K, Figure 6-3) between CCSM3 and the NCEP reanalysis (Collins et al., 2006). In addition, the excess precipitation near the equator simulated by CCSM3 (Figure 5-3) was possibly due to the warm sea surface temperatures caused by an over-estimation of tropical everwet conditions in the Indonesian Throughflow. Collins et al. (2006) noted that CCSM3 overestimates the sea

surface temperatures within 15º longitude of the western coast of Africa (between 30ºS and the equator) and South America (between 40ºS and the equator). This bias may explain why the tropical biome in Central South America is not well reproduced because CCSM3 appears to underestimate the precipitation in this region as a result of the northward shift in the ITCZ (see Figure 5-3).

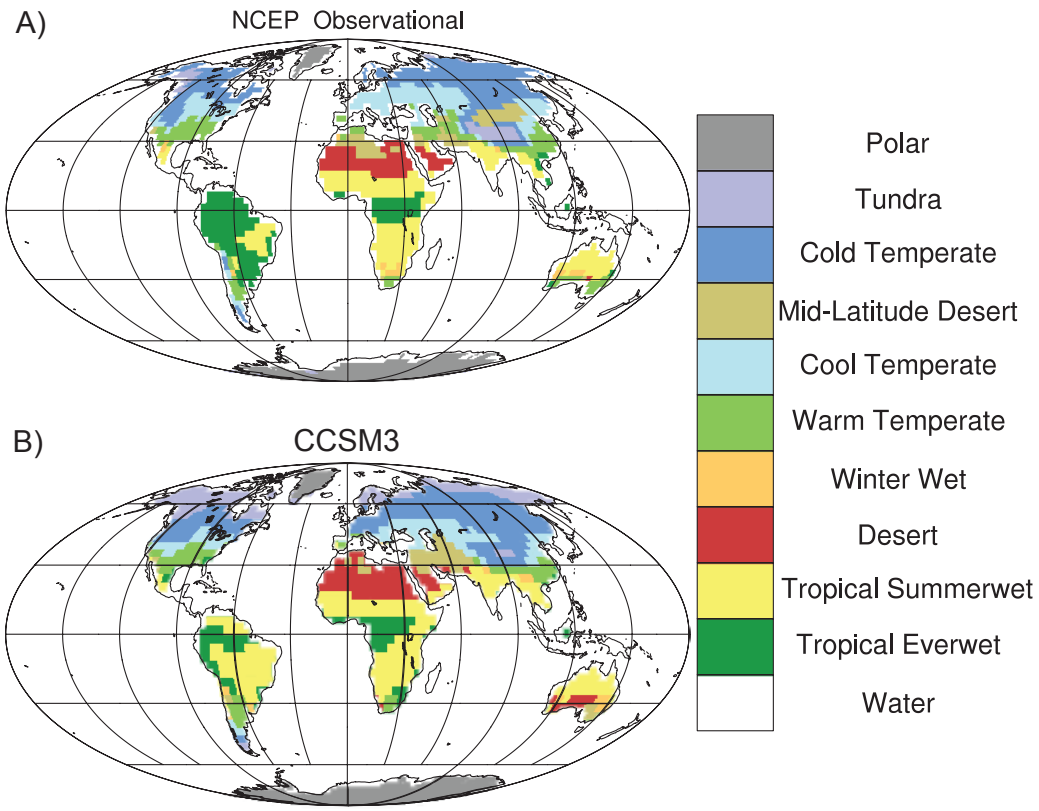

Figure 6-2 Comparison of present-day biome classifications for A) data from the National Center for Environmental Prediction interpolated on a 2.5 × 2.5 grid and B) CCSM3 simulation with ~3.75˚ × 3.75˚ horizontal resolution.

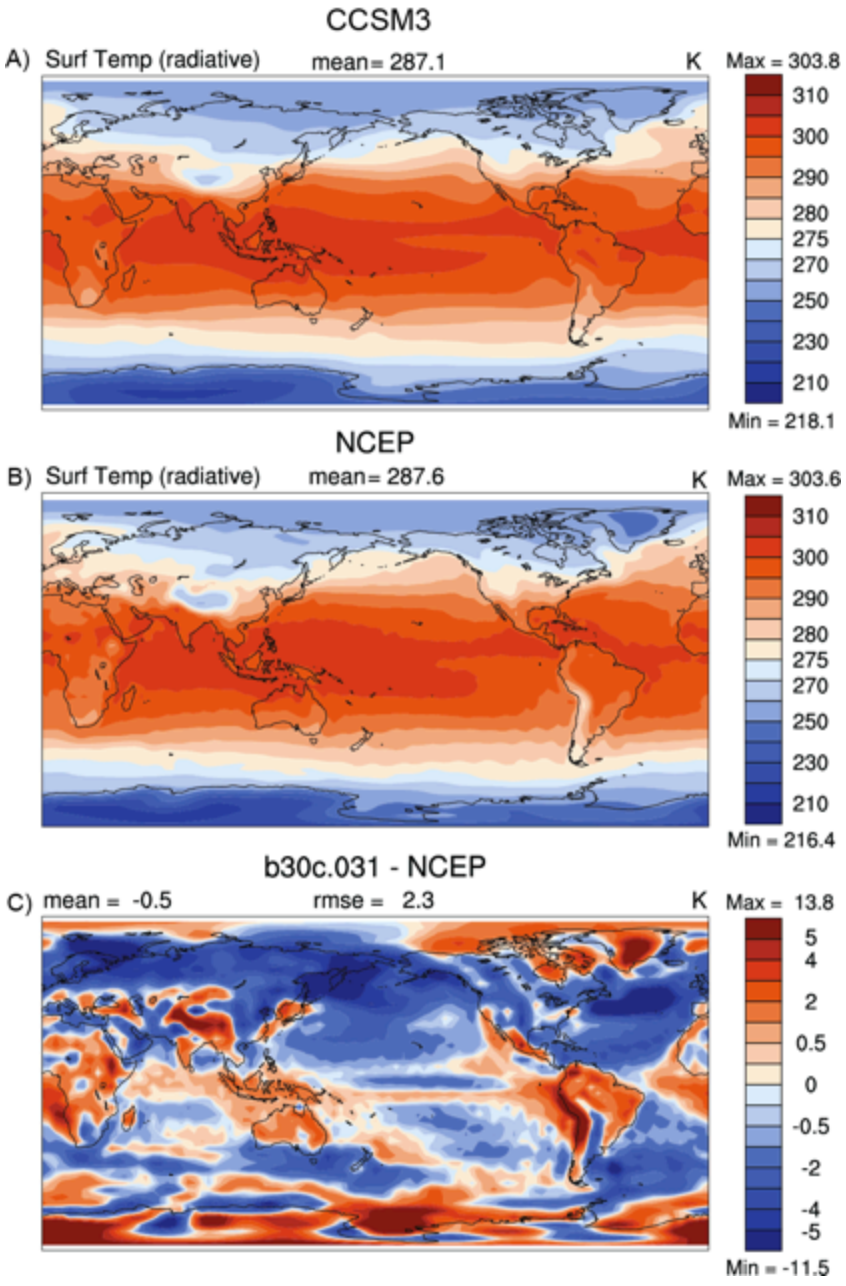

Figure 6-3 Comparison of present-day mean annual surface temperatures (K) for CCSM3 present-day simulation, B) NCEP, and C) difference between CCSM3 and NCEP.

6.4 Late Permian biomes

Experiments used for biome analysis were structured the same as those used for climate-sensitive sediments with two experiments differing in their atmospheric carbon dioxide concentrations, featuring a 4 × CO_2 experiment and a 12.7 × CO_2 experiment (see section 5.2). In addition to the comparison of climate-sensitive sediments found in the geological record, 2978 paleobotany records from the Middle Permian, Late Permian, and Early Triassic were analyzed with the biome maps. The Late Permian analysis of biome changes was modeled after methods used by Ziegler (1990) and Rees et al. (1999; 2002). Rees et al. (1999) integrated lithological and flora data from the Early and Middle Permian to determine the global climate during the Wordian (267-265 Ma). Terrestrial environments were classified into biomes based primarily on leaf morphologies and their geographical distribution. Rees et al. (2002) assigned floral genus to a coarser morphological category at the level of plant class or order based on Meyen (1987) and Taylor and Taylor (1993). Moreover, Walter's (1985) biome scheme was incorporated into Rees et al.'s (1999) sensitivity experiments. Table 6-2 contains a list of the morphological categories and their corresponding biome zones. Appendix D contains a list of the morphological categories and the genera used in the biome plots. In order to maintain consistency, the same genera as used by Rees et al. (2002) were applied in plotting the biomes for each epoch. Morphological characteristics correlating with biomes were adapted from Ziegler et al. (1990) and Rees et al. (2002). The floral data used in the phytogeographic maps in this study were obtained from the Fossilworks, formerly the Paleobiology Database (www.paleodb.org, Rees et al., 2014). The primary focus was on gymnosperms such as glossopterids (Gulbranson et al., 2012; Gulbranson et al., 2014), and gigantopterids (Glasspool et al., 2004), which tend to have fairly well defined geographical distributions and climatic signals (Rees et al., 1999).

Ziegler (1990) used the *Glossopteris* flora as an indicator of cool temperature conditions; however, its distribution appears to be limited to the southern hemisphere. Cordaites serve as a cool temperate marker for the northern hemisphere due to their interpreted deciduous nature and large, tongue-like leaves (Ziegler, 1990; Rees et al., 1999); however, the actual span of Cordaites included other biome zones (see Table 6-2). Both glossopterids and cordaites appeared to be able to withstand cold temperate conditions but these plants were not abundant. Gigantopterids are indicative of warm, tropical regions for both Ziegler (1990) and Rees et al. (1999) as they appear to be climbing vines similar to those found in modern-day tropical zones.

Table 6-2 Morphological categories and their corresponding biome zones, table adapted from Ziegler (1990) and Rees et al. (1999; 2002).

Morphological Category	Biome Zones	Additional information
Cordaite	1, 2, 4, 5, 6, 8	Most common in 5 and 6
Cycadophyte	1, 2, 4, 5	Rainforest to stressed environments
Fern	1, 2, 4, 5	
Fern 3	1, 2, 4, 5, 6	Often found with sphenopsids
Gigantopterid	1, 2, 5	Most common in 1
Ginkgophyte	2	Evolved to dominate high latitudes in the Mesozoic
Glossopterid	5, 6, 8	Most common in 6
Lycopsid	1, 2, 4, 5	Indicator of a warming climate
Peltasperm	1, 4, 5, 6	Most common in 5
Pinales	3, 7, 6	Typical of transitional to arid climates
Pteridosperm	1, 4, 6	Most common in 1
Sphenopsid	1, 2, 4, 5, 6, 8	Most common in 5 and 6

6.5 Results of biome classifications for the Permian

Comparison of other biome simulations for the Middle Permian (Wordian) with the inferred biome phytogeographic map suggests that the 4 × CO_2 experiment using the fully coupled CCSM3 revealed a more definitive reconstruction of past climatic conditions. Figure 6-4 illustrates the difference between GENESIS 2 and CCSM3 models, as well as the geological record. The CCSM3 experiment with an atmospheric CO_2 concentration of 4 × CO_2 is in general agreement with the Wordian (Middle Permian) data-derived biomes (Rees et al.(1999). The polar temperature bias between CCSM3 and reconstructed biomes is significantly lower compared to the GENESIS 2 simulation (Gibbs et al., 2002), likely because of the heat transport by warm poleward currents (Winguth et a., 2002) in a fully coupled climate simulation. It is noteworthy that this study used an even atmospheric CO_2 concentration, the quadrupling of the atmospheric is based on the preindustrial level of 280 ppmv of atmospheric CO_2 (1120 ppmv), whereas Gibbs et al. (2002) used the "present-day" reference CO_2 value 345 ppmv. Climate-sensitive sediment and flora data from the Late Permian did not correspond well with the higher latitude predicted biomes for the experiment with an atmospheric CO_2 concentration of 4 × CO_2 but were in better agreement with the simulation of 12.7 × CO_2. Temperate biome zones did migrate poleward and replaced polar and tundra biomes with an increase in atmospheric CO_2 radiative forcing, because they are sensitive to changes in temperature and precipitation patterns, as shown by the comparison of the 4 × CO_2 experiment with the 12.7 × CO_2 experiment (Figure 6-5). In the subtropics, an increase of desertification is simulated in the 12.7 × CO_2 experiment due to reduced precipitation and soil moisture (see also section 5; Figure 5-16). An increase in the tropical everwet biome was simulated by the 12.7 × CO_2 experiment because of a greater rate of precipitation along the equator on the supercontinent of Pangea (Figure 5-16).

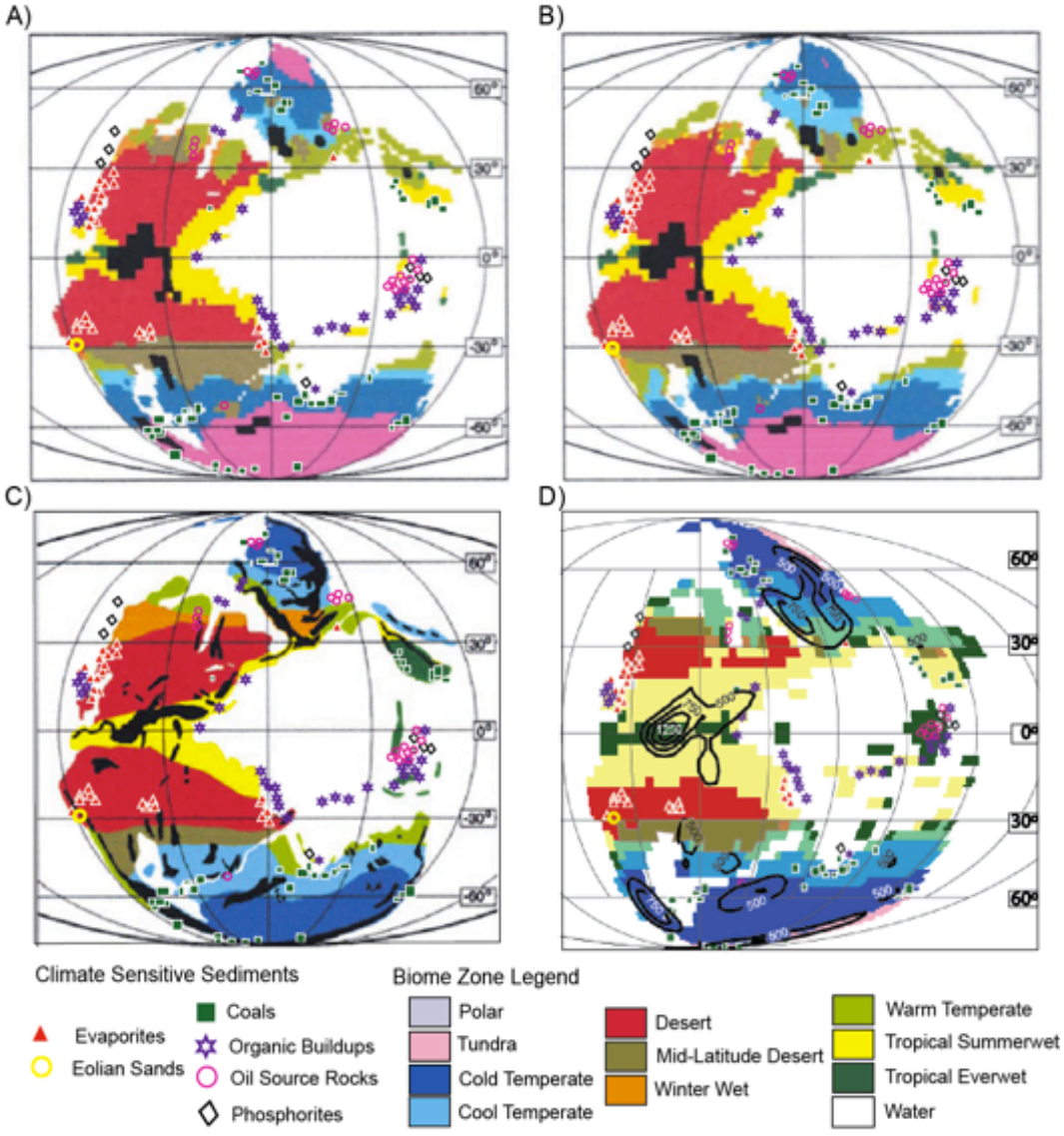

Figure 6-4 Wordian climate-sensitive sediment records from Ziegler et al. (1998) and Gibbs et al. (2002) placed on A) Permian biome zone reconstructions from Rees et al. (2002), B) the simulated biome of the 4 × CO_2 experiment from CCSM3 (this study), C) the 4 × CO_2 Wordian experiment, and D) 8 × CO_2 Wordian from GENESIS 2 (Rees et al., 2002).

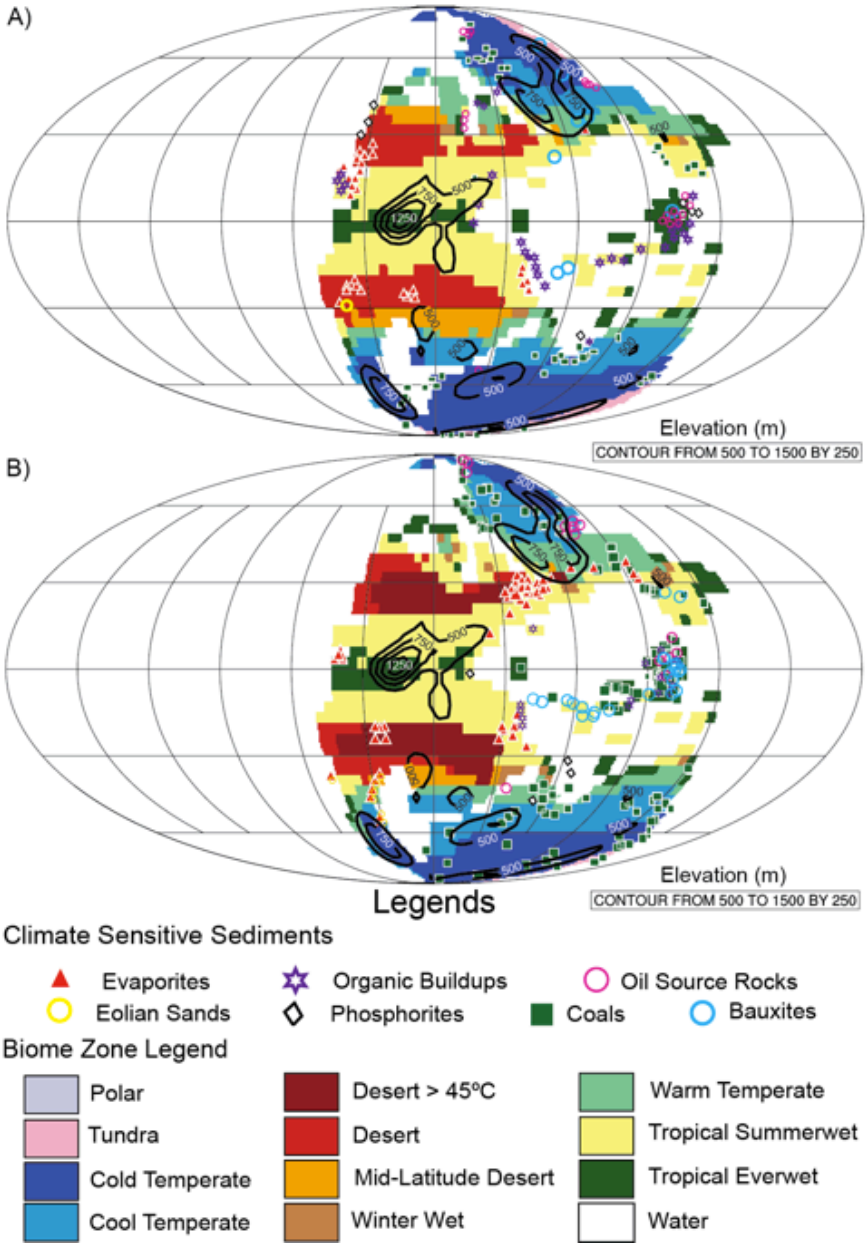

Figure 6-5 Biome zones for A) the 4 × CO_2 experiment with climate-sensitive sediments from the Middle Permian and B) 12.7 × CO_2 experiment with climate-sensitive sediments from the Late Permian.

The biome simulation for the experiment with an atmospheric CO_2 concentration of 12.7 × CO_2 is in general agreement with the lithological data from the Late Permian with the exception of some mid-latitude evaporites. These discrepancies are likely due to the coarse resolution of the model, which does not resolve smaller mountain ranges. Coals are primarily found in cool to cold temperate environments where moisture and swamps are abundant, as well as in tropical regions.

The Cathaysian group refers to plants that were typically found on individual paleocontinents that separated the Panthalassa from the Paleo-Tethys Ocean (Rees et al., 2002; Chumakov and Zharkov, 2003). The Cathaysian flora is represented with the morphological categories of cycadophytes, gigantopterids, and lycopsids. The paleocontinents were located within 30º of the equator with a majority of the landmasses within 20º latitude south of the equator. The climate within this zone included the tropical everwet and summerwet biome zones. Figure 6-6 represents the experiments with Cathaysian floral group superimposed onto the biome maps. Comparison of the Cathaysian flora was an exemplary match with the biomes projected for the Middle Permian by the 4 × CO_2 experiment (Figure 6-6 A), the Late Permian by the 12.7 × CO_2 experiment (Figure 6-6B), as well as the Early Triassic flora superimposed on the 12.7 × CO_2 experiment (Figure 6-6C). All three paleobotany-biome comparisons for the Cathaysian realm were 100% matched. In addition to the Cathaysian floras, the tropical everwet and summerwet biomes are represented by the morphological groups of cordaites, ferns, peltasperms, and sphenopsids. Many of these morphological categories also had genera within the warm temperate biome. Differences between the paleobotany data and the models reflect the fossils plotted outside of the normal climate for the morphological category.

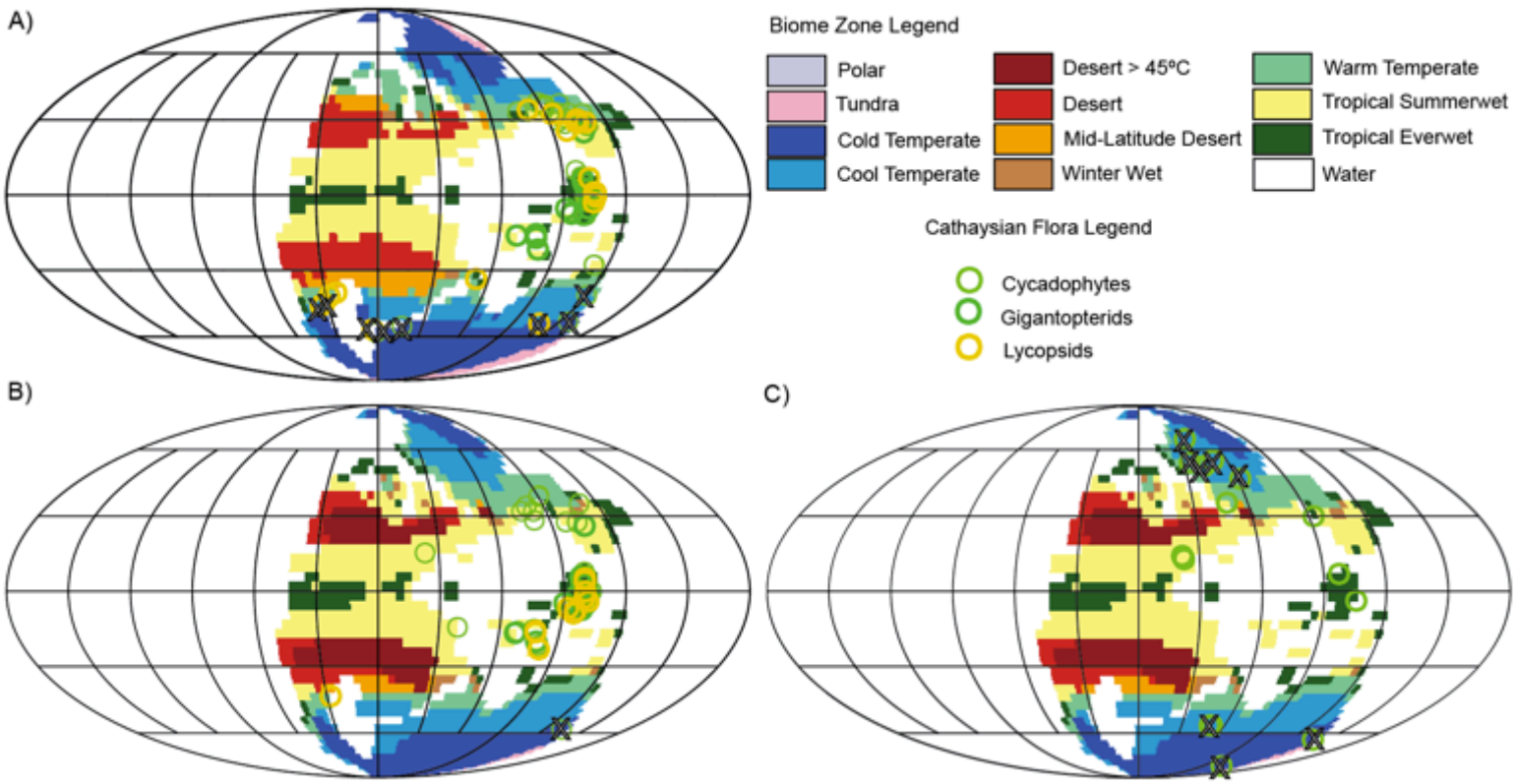

Figure 6-6 Reconstructed tropical flora in the Cathaysian realm for the A) 4 x CO_2 experiment with Middle Permian flora, B) 12.7 x CO_2 experiment with Late Permian flora, and C) 12.7 x CO_2 experiment with Early Triassic flora. “X” signifies the mismatch between the simulated biome with CCSM3 and reconstructed paleobotany (see also Figure 6-7).

The 4 x CO_2 Middle Permian simulation generally agreed with reconstructed biomes with a polar bias as discussed in the above section. In particular, the ferns, and lycopsids likely did not exist in the cool to cold temperate range (Figure 6-7). However, the cumulative percentage variance of missed biome zones comparable to the amount of data was insignificant for ferns type 1 (0.3%) and ferns type 3 (3.9%). Lycopsids had a larger variance of 16.0%. The biome zones in the 12.7 x CO_2 experiment had similar misaligned paleobotany data with biome zones within the southern hemisphere. Incompatible morphological categories included cordaites (2.7%), cycadophytes (2.9%), ferns type 1 (18.7%) and ferns type 3 (18.4%). Discrepancies between the simulations and the paleobotany data were isolated to coastal regions, which suggests that the inability of CCSM3 to resolve coastal regions due to the coarse resolution is a significant obstacle. The 12.7 × CO_2 experiment with an overlay of Early Triassic morphological data Figure 6-7C) had significant discrepancies with a variance of 70% for cycadophytes and 58.7% for ferns type 1; however, data for Early Triassic paleobotany from these genera are quite limited. Cordaites and fern 3 had an accurate placement whereas no existing records were available for gigantopterids, lycopsids, or pteridosperms.

Cool and cold temperate biomes were isolated to the higher latitudes poleward of 35º in all simulations. Tundra regions were small and were simulated near the North and South Pole for the 4 × CO_2 experiment (Figure 6-8A), whereas the tundra coverage elimited in the Northern Hemisphere and significantly reduced in the southern polar region for the 12.7 × CO_2 experiment (Figure 6-8B and Figure 6-8C). All of the regions represented by the tundra biome are located near mountain ranges (see Figure 6-5).The glossopterid morphological category is restricted to cool to cold temperate biomes within the southern hemisphere rendering it necessary to add an additional morphological category in order to analyze the northern hemisphere cool to cold temperate biomes.

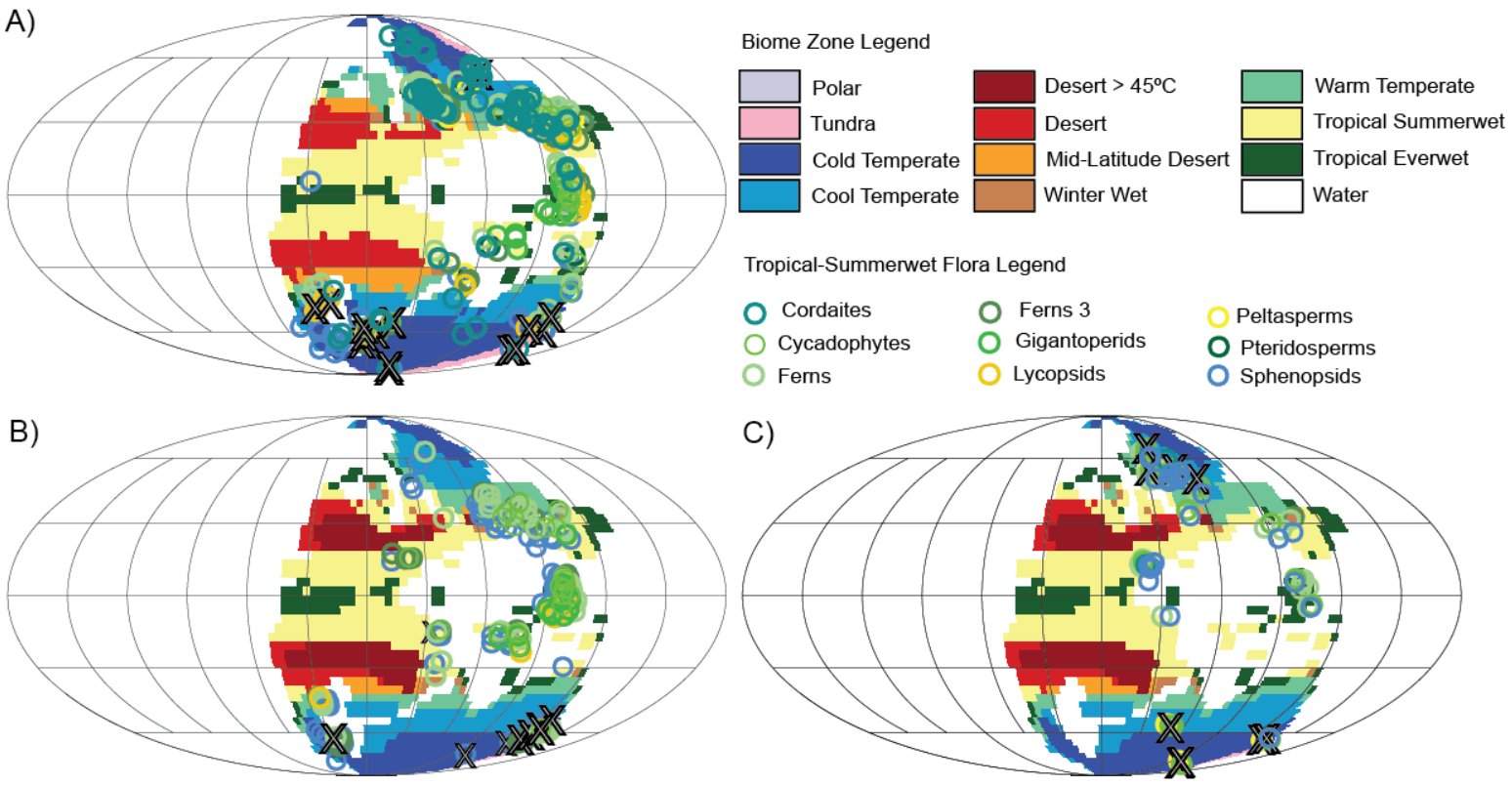

Figure 6-7 Simulated biome and reconstructed tropical everwet and summerwet flora for the A) 4 x CO_2 experiment with Middle Permian flora, B) 12.7 x CO_2 experiment with Late Permian flora, and C) 12.7 x CO_2 experiment with Early Triassic flora. "X" signifies the mismatch between the simulated biome with CCSM3 and reconstructed paleobotany.

The cordaites group was likely present in the cool and cold temperate biome zone but may also have represented tropical everwet, tropical summerwet, warm temperate and winterwet conditions. The Middle Permian simulation with glossopterid paleobotany data suggested an incompatibility with biome zones of 35.6% (Figure 6-8A) whereas simulation-data comparison with the Late Permian biomes improved with only 23.5% non-inclusion from the prescribed biome zone. Cordaites irregularities were insignificant with a 0.5% and 2.7% discrepancy with the simulated biomes from the Middle and Late Permian respectively. Though there were records in Paleodatabase for glossopterids for the Early Triassic, it is likely that these records are incorrectly dated as it is reputed that *Glossopteris* had become extinct at the end of the Permian. Nevertheless, Figure 6-8C contains paleodata obtained for cordaites and glossopterids with a 50.0% omission rate with projected biomes.

Fossil flora is rarely preserved in arid and desert conditions due to the harsh environment. The 4 x CO_2 experiment suggested that desert temperatures exceeded 30ºC on an annual basis (Figure 6-9A) and could surpass 40ºC during the summer months in both hemispheres (Figure 6-9B and Figure 6-9C). The 12.7 x CO_2 experiment depicted annual averaged surface temperatures >35ºC (Figure 6-10A) whereas summer temperatures exceeded 45ºC in both hemispheres. The desert and mid-latitude desert biomes were not compatible with paleobotany data for the Middle Permian (Figure 6-11A) or the Late Permian (Figure 6-11B) and no floral data was available for the Early Triassic (Figure 6-11C). Validation of biome zones inferred from climate simulations in desert regions are challenging because desert-like conditions with high temperature and low water availability cause fatal stress on the plants and thus these regions lack preserved fossil plants. In this study, the pinales morphological category was selected to reconstruct arid conditions as well as low-lying areas, but not necessarily desert climates.

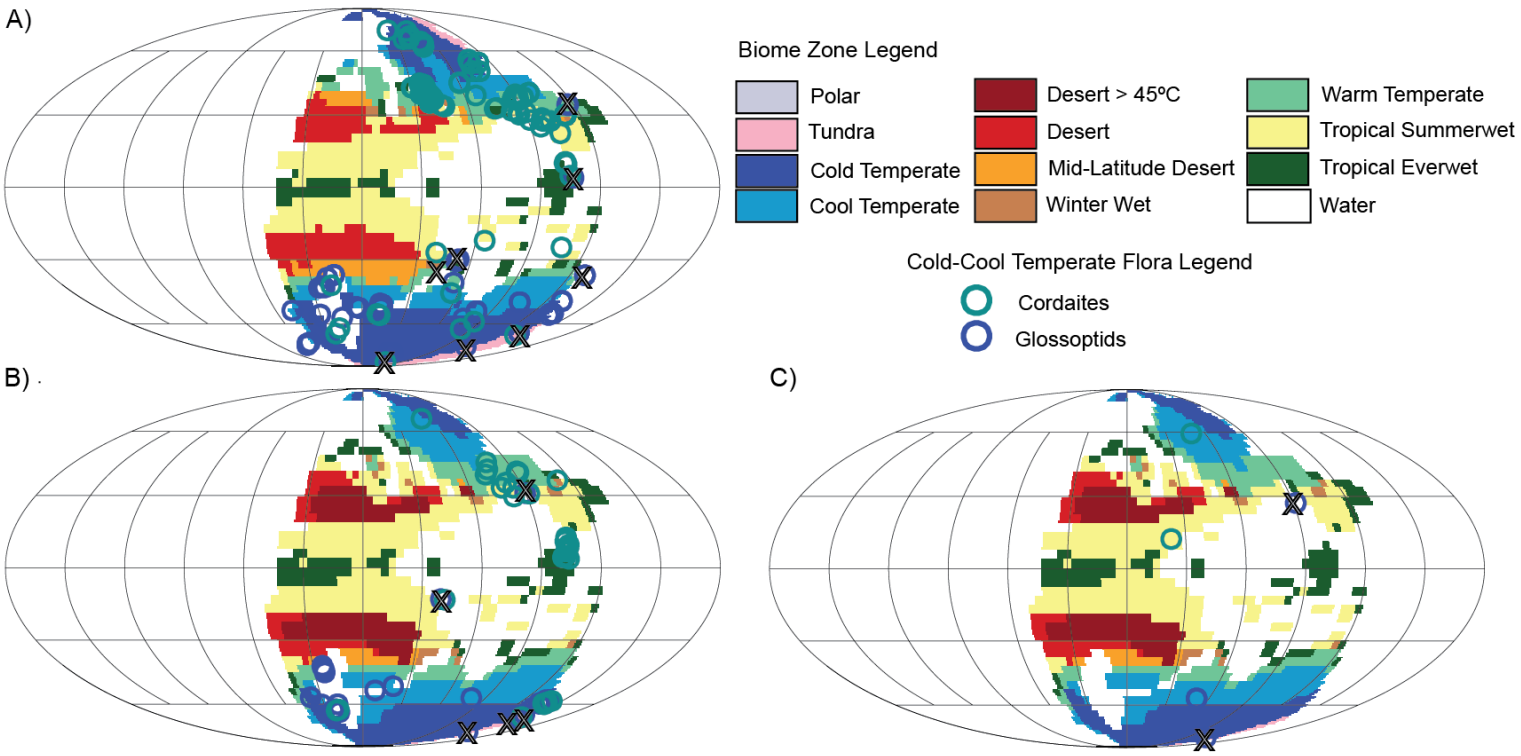

Figure 6-8 Reconstructed paleobotany for cold tolerant Permian flora for A) 4 x CO_2 experiment with Middle Permian flora, B) 12.7 x CO_2 experiment with Late Permian flora, and C) 12.7 x CO_2 experiment with Early Triassic flora. “X” signifies the mismatch between the simulated biome with CCSM3 and reconstructed paleobotany.

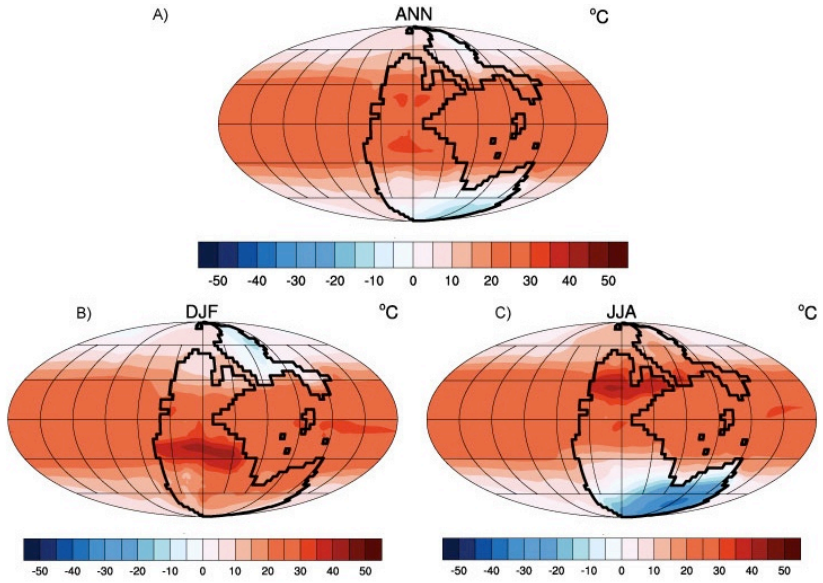

Figure 6-9 Surface temperatures (ºC) simulated in the 4 x CO_2 experiment for A) annual average, B) boreal winter, and C) boreal summer.

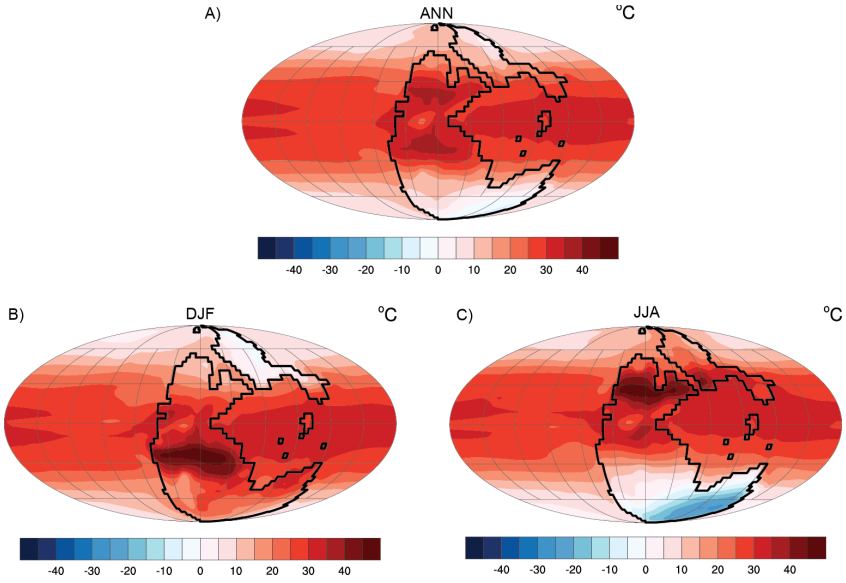

Figure 6-10 Surface temperatures (ºC) simulated in the 12.7 x CO_2 experiment for A) annual average, B) boreal winter, and C) boreal summer.

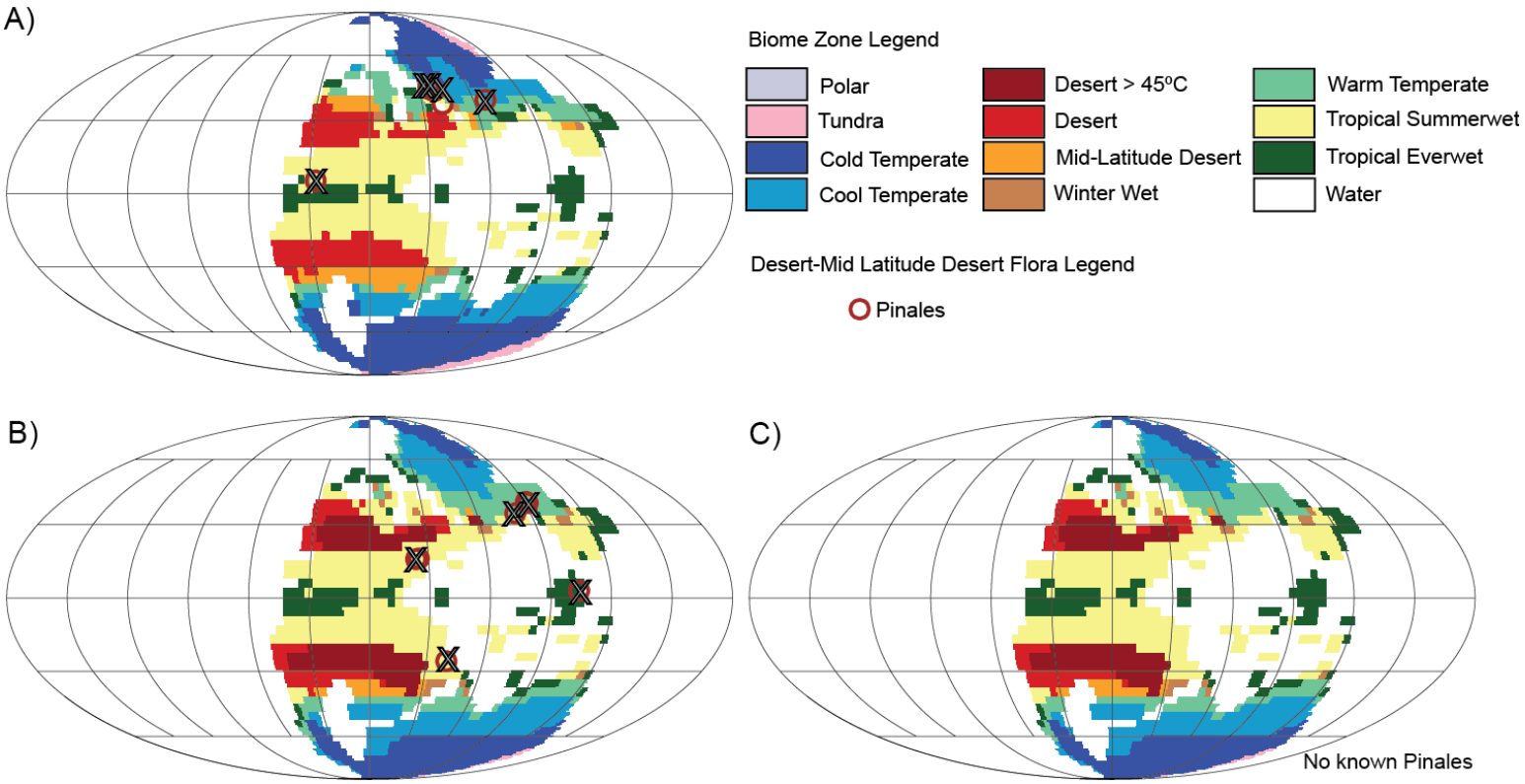

Figure 6-11 Reconstructed paleobotany for pinales flora (semi-desert biome) for A) 4 x CO_2 experiment with Middle Permian flora, B) 12.7 x CO_2 experiment with Late Permian flora, and C) 12.7 x CO_2 experiment with Early Triassic flora. “X” signifies the mismatch between the simulated biome with CCSM3 and reconstructed paleobotany.

6.6 Discussion

In this study, climate-sensitivity experiments have been compared with climate-sensitive sediments and paleobotany for a better understanding of the climatic transition from the Middle Permian to the Early Triassic. Previous studies identified a cold bias in the simulated polar regions of Gondwana for the Wordian (Gibbs et al., 2002; Rees et al., 1999; 2002), which has been reduced in this study by considering coupled atmosphere dynamics.

The CCSM3 4 × CO_2 simulation was in reasonable agreement with lithological and paleo-floral data from the Middle Permian and demonstrated a greater sensitivity to CO_2 radiative forcing in polar regions than previous Wordian simulations with GENESIS 2 (Rees et al., 1999: 2002) and CCSM1 (Kutzbach and Ziegler, 1993).

Similar to the 4 × CO_2 experiment, the 12.7 × CO_2 experiment simulated a cold bias compared to the reconstructed biome for southern Gondwana but to a lesser extent than the 4 × CO_2 experiment. The bias could also be related to uncertainty of the cloud optical thickness in polar regions (Kump and Pollard, 2008) and precipitation patterns in mountain ranges and resolution coastal areas. Therefore, future simulations on a higher resolution model may improve the precipitation pattern and biome projections.

The 12.7 × CO_2 experiment compared with the Early Triassic paleo-floral data was not a reasonable match with the available geological data. It has been estimated that the CO_2 concentrations may have been as high as 30 times the pre-industrial atmospheric concentrations (Kidder and Worsley, 2004). A comparison of the paleodata to the model simulation suggested an increase in atmospheric CO_2 is likely required in order to simulate the paleoconditions.

Vegetation changes at high latitudes can also significantly affect climate (Dutton and Barron, 1997; Otto-Bliesner and Upchurch, 1997; Liu et al., 2006). Vegetation

feedbacks should be considered in future simulations and perhaps a dynamic vegetation model would considerably improve projections.

One of the major challenges using paleo-floral data is the bias related to preservation and diagenesis. Fossils of plant matter are likely to be formed in humid regions with annual average temperatures of > 10ºC. Regions of extreme climates such as deserts and tundra and with little precipitation are not likely to sustain much plant life, and what does survive rarely becomes preserved in sediments. Errors in the interpretation of plant fossils (e.g. sampling error or miss-classification) can lead to significant oversights. An inaccuracy in interpretation may have occurred for the genus *Glossopteris*, as it is documented that *Glossopteris* became extinct during the latest Permian, yet there was a record of a few fossils from the cool-cold temperate plant marked as originating in the Late Triassic. Furthermore, *Glossopteris* was strictly a southern hemispheric plant, yet there is documentation of a few *Glossopteris* fossils existing in the northern hemisphere in North China.

6.7 Conclusion

The comparison between simulated and reconstructed biomes indicated reasonable agreement between two independent approaches. However, uncertainties in the biome scheme existed for the Middle Permian and the Late Permian. The bias between simulated and reconstructed biomes for the Early Triassic was significant, particularly in the polar regions, and therefore suggests that either the atmospheric CO_2 concentration levels were significantly higher than the 12. 7 × CO_2 preindustrial concentrations or a large influx of a different greenhouse gas, such as methane, contributed to the strong warming trend. This finding is in line with previous studies conducted by Kidder and Worsley (2004). The results of the simulations and fossil flora

data did confirm a significant change in environments in the interior of Pangea between the Middle and Late Permian as a rise in surface temperatures in the high latitudes and desert regions expanded in both hemispheres.

Difficulties with the comparisons also arose due to the inability to resolve the finer details of ocean coastal processes as well as small-scale steep mountain ranges. In the future, experiments conducted with a higher resolution model or perhaps a regional model would lead to a more complete and accurate understanding of the climates and climate change for the Late Paleozoic.

Chapter 7

Future Perspectives

7.1 Climate simulations to be used in future

Additional sensitivity experiments already completed utilizing different orbital cycles (Winguth and Winguth, 2013) and cloud optical properties (Winguth et al., 2012) can be analyzed with climate-sensitive sediment and paleobotany data. Further analysis of the sensitivity experiments should include the investigation of shifts in seasonal conditions as well as upwelling patterns. Oceanic temperature and salinity patterns of these simulations should be analyzed to determine if model conditions correspond with the lithology as well as the flora of the Late Permian as such results may clarify some of the intercontinental discrepancies. The additional sensitivity experiments would allow for greater detail and understanding of the climate change that occurred during the Permian-Triassic transition.

7.2 Orbital cycles

Gravitational effects of other planetary bodies can cause orbital perturbations that can periodically vary the distribution of incoming solar radiation on Earth (Crowley and North, 1991). The Milankovitch theory describes these orbital cycles in the Earth's movement that influence the climate. There are three main orbital perturbations described as eccentricity, obliquity and precession (Crowley and North, 1991). Eccentricity, which refers to the trajectory of the Earth around the sun that varies from a near circular to slightly elliptical ($e \approx 0.0$ to 0.06 maximum) orbit, has periods of approximately 100 ky and 400 ky (Crowley and North, 1991; Laskar et al., 2004). Of these cycles, the approximately 100,000 - year eccentricity cycle appears to have

affected the amount of insolation received by the northern hemisphere at the summer solstice as much as 8% during the last 100 ky cycle, therefore influencing the advancing and retreating of glaciers (Crowley and North, 1991). Obliquity describes the tilt of the Earth's axis as it varies between 22º and 25º with a period of approximately 41,000 years; these perturbations tend to amplify the seasonal changes in high latitudes with a minimum influence in the tropics. Precessional cycles record the change in distance between the earth and the sun during the seasons and have two components: axial precession, in which the torque of other celestial bodies on the earth's equatorial bulge can cause the axis of rotation to "wobble", and the elliptical precession.. These precessional cycles are approximately 23,000 years and 19,000 years. Precession changes the distance between the Earth and the Sun on a seasonal basis, thereby causing warm winters and cool summers in one hemisphere while across the equator the opposite occurs. The extremes of the precession cycles can influence the monsoonal intensity resulting in increased precipitation, runoff and weathering of the continents (Winguth and Winguth, 2013). Variation in climate can be attributed to changes in insolation due to the shift in Earth's orbital parameters, which in turn can disrupt seasonal monsoonal precipitation patterns greatly affecting biological activity.

7.3 Orbital Cycles during the Late Permian

Cyclic patterns related to orbital forcing have been determined by magnetic susceptibility data and are present in many of the PTB sediments, such as those in Shangsi, Southern China (Huang et al., 2011). Wavelet analyses performed by Rampino et al. (2000) indicate cyclic patterns in the Gartnerkofel core samples taken from the Carnic Alps in Austria. Additional evidence of increased monsoonal circulation has been inferred by the analysis of varve sediments from the Castile Formation that would have

been located in the western tropical region of Pangea (Anderson, 2010) during the Permian. The large continental landmass of Pangea would have incurred strong seasonal variability within the subtropics (Barron and Fawcett, 1995) and a high likelihood of a substantial increase in rainfall during the summer from megamonsoons (Kutzbach and Gallimore, 1989).

Winguth and Winguth (2013) investigated the response of the strength of the monsoonal circulation, and related changes in ocean circulation, productivity and dissolved oxygen distribution to changes in the Earth's orbital parameters for the end-Permian using a comprehensive climate system model. The study demonstrated the influence of orbitally-driven changes in regional incoming solar radiation on temperature (Figure 7-1), precipitation (Figure 7-2), and associated runoff. The pronounced changes in seasonal sea and air surface temperatures in the subtropics during the summer months resulted the differences in surface radiative forcing. An increase in monsoonal precipitation across subtropical Pangea was simulated with the P+ experiment in addition to enhanced evaporation, an increase in cloud cover and precipitation during the northern hemisphere's summer months (Winguth and Winguth 2013).

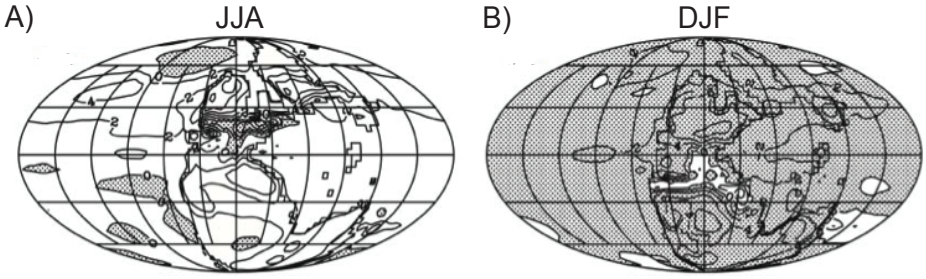

Figure 7-1 Seasonal surface air temperature differences between the maximum (P+) and minimum (P-) precessional cycles for A) austral winter months and B) boreal winter months (from Winguth and Winguth, 2013).

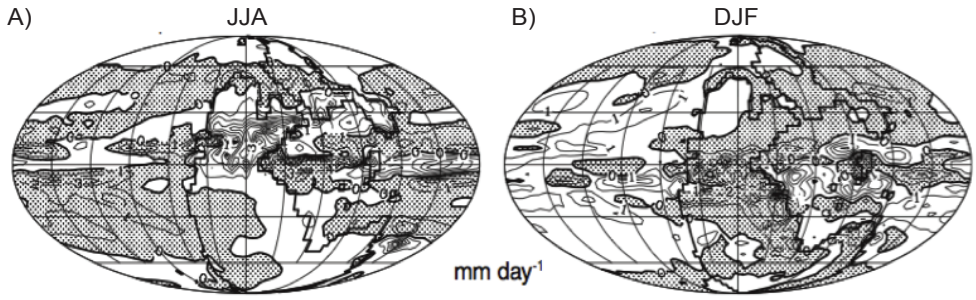

Figure 7-2 Seasonal precipitation differences (mm day^{-1}) between the maximum (P+) and minimum (P-) precessional cycles for the A) austral winter months and B) boreal winter months (after Winguth and Winguth, 2013).

Expanding upon previous sensitivity experiments performed by Winguth and Winguth (2013), analyses on water masses (see Chapter 5) and biomes (see Chapter 6) could be conducted to determine how precessional cycles may have influenced the climatic zones. For the precessional scenarios, eccentricity, obliquity and the vernal equinox settings were adjusted to reflect the precessional minima (P-) and precessional maxima (P+). The P– scheme is characterized by a reduced seasonal cycle with the vernal equinox set at 90º, which represents the prograde angle between the perihelion and the vernal equinox (Winguth and Winguth, 2013). The P+ scenario is characterized by an enhanced seasonal cycle and the precession of the equinox is set to 270º causing the Northern Hemisphere to be nearest the Sun during the summer solstice (Winguth and Winguth, 2013).

7.4 Cloud albedo

Clouds can have a significant impact on the climate by inhibiting incoming, shortwave solar radiation as well as by reflecting longwave radiation back towards the

Earth's surface. Aerosols in the atmosphere can serve as cloud condensation nuclei (CCN). Small particles and aerosols entering the atmosphere such as dust, gases, and salts can become CCN and enhance cloud cover and cloud optical thickness, effectively altering Earth's albedo and climate.

One of several contributing natural sources of CCN are sulfur compounds that are released into the air. Plankton and algae are capable of releasing dimethyl sulfate (DMS) that can escape into the atmosphere where it is altered to sulfate aerosols that act as CCN (Charlson et al., 1987). Additionally, SO_a and H_2S emissions from volcanoes and fumaroles increase the concentration of CCN in the atmosphere (Charlson et al., 1987). Size distribution and concentration of CCN can affect the size of cloud droplets, which would influence the production of precipitation as well as cloud cover (Charlson et al., 1987).

A reduction of oceanic productivity could thus lower the CCN concentrations (Kump and Pollard, 2008) by reduced DMS emissions from the ocean, therefore significantly reducing cloud optical thickness. Reduction of cloud optical thickness would permit more solar radiation to reach the Earth's surface. Increased atmospheric CO_2 concentrations coupled with additional incoming solar radiation would likely intensify surface temperatures causing stress among terrestrial fauna and flora. With the large marine mass extinction occurring during the Permian-Triassic transition, it is reasonable to assume that the decline in productivity would lead to a reduced dimethyl-sulfide (DMS) emission from the ocean and hence reduced SO_4 aerosols in the atmosphere (Charlson et al., 1987; Andreae, 1990; Kump and Pollard, 2008; Winguth et al., 2012). These assumptions are based on an anti-CLAW scenario. The CLAW hypothesis (Charlson et al., 1987) states that a feedback loop occurs when an increase of photosynthesis within the oceans leads to an increase in the breakdown of DMS first in the seawater and then

in the atmosphere which leads to increased sulfate aerosols. If photosynthesis decreases within the oceans, as in a collapse of the phytoplankton population due to a decrease in nutrient supplies, the decline in DMS production could lead to a decrease in CCN and a reduction of cloud albedo. Figure 7-3 illustrates the possible feedback loop that can ensue due to change in DMS emissions.

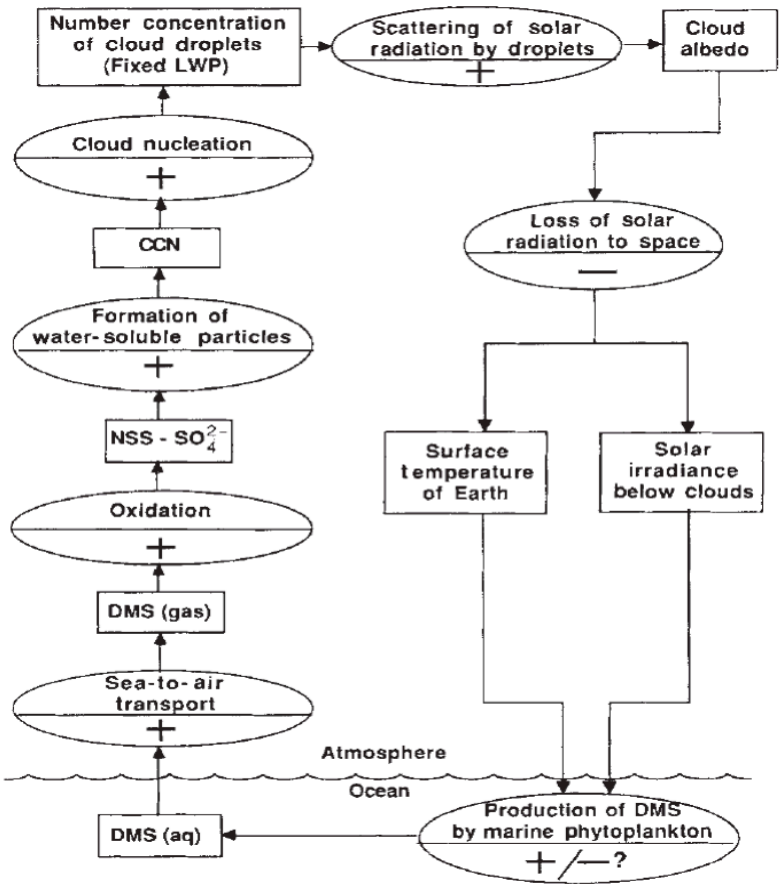

Figure 7-3 Diagram of a possible climate feedback loop (CLAW hypothesis) involving the production of DMS by marine phytoplankton, CCN, and cloud albedo. Positive and/or negative signs suggest the effect of the change of quantity that is reflected in the preceding rectangle on the succeeding rectangle (from Charlson et al., 1987).

To address reduction in CCN and associated polar warming, Winguth et al. (2012) reduced cold cloud particle concentration from 150 per cm^3 to 50 per cm^3, increasing the cloud radii by ~20% over the ocean and by 110% over the land. The reasoning for these changes is based on the assumption that cloud condensation nuclei were reduced at the PTB, because global productivity declined with a transition into a hothouse world (Winguth et al., 2012). Analysis of water masses (see Chapter 5) and biomes (see Chapter 6) should be conducted on the sensitivity experiments performed by Winguth et al. (2012) to determine possible impacts on the Late Permian climate.

Appendix A

Acronyms

AGCM	Atmospheric General Circulation Model
AMWG	Atmospheric Model Working Group
CAM	Community Atmosphere Model
CNN	Cloud condensation nuclei
CCSM	Community Climate System Model
CLM	Community Land Model
CSIM	Community Sea-Ice Model
DOE	Department of Energy
FB	Flat-bottom ocean floor experiment
GCM	General Circulation Model
GSSP	Global Boundary Stratotype Section and Point
IUGS	International Union of Geological Sciences
MOR	Mid-ocean ridge experiment
NC	North China block
NCAR	National Center for Atmospheric Research
NCEP	National Centers for Environmental Prediction
OCMIP	Ocean Carbon-cycle Model Intercomparison Project
OGCM	Ocean General Circulation Model
OMZ	Oxygen Minimum Zone
POC	Particulate organic carbon
PTB	Permian-Triassic Boundary
SC	South China block
UCAR	University Corporation for Atmospheric Research

Appendix B

Physical constants

Constant Name	Symbol	Constant	Unit
Acceleration of gravity	g	9.80616	$m\ s^{-1}$
Standard pressure	P_{std}	101325	Pa
Stefan-Boltzmann constant	σ	5.67×10^{-8}	$W\ m^{-2}\ K^{-4}$
Boltzmann constant	κ	1.38065×10^{-23}	$J\ K^{-1}\ molecule^{-1}$
Avogadro's number	N_A	6.02214×10^{26}	$molecule\ kmol^{-1}$
Universal gas constant	R_{gas}	$N_A\kappa$	$J\ K^{-1}\ kmol^{-1}$
Molecular weight of dry air	MW_{da}	28.966	$kg\ kmol^{-1}$
Dry air gas constant	R_{da}	R_{gas}/MW_{da}	$J\ K^{-1}\ kg^{-1}$
Molecular weight of water vapor	MW_{wv}	18.016	$kg\ kmol^{-1}$
Water vapor gas constant	R_{wv}	R_{gas}/MW_{wv}	$J\ K^{-1}\ kg^{-1}$
Von Karman constant	k	*0.4*	-
Freezing temperature of fresh water	T_f	273.16	K
Density of liquid water	ρ_{liq}	1000	$kg\ m^{-3}$
Density of ice	ρ_{ice}	917	$kg\ m^{-3}$
Specific heat capacity of dry air	C_p	1.00464×10^{3}	$J\ kg^{-1}\ K^{-1}$
Specific heat capacity of water	C_{liq}	4.188×10^{3}	$J\ kg^{-1}\ K^{-1}$
Specific heat capacity of ice	C_{ice}	2.11727×10^{3}	$J\ kg^{-1}\ K^{-1}$
Latent heat of vaporization	λ_{vap}	2.501×10^{6}	$J\ kg^{-1}$
Latent heat of fusion	L_f	3.337×10^{5}	$J\ kg^{-1}$
Latent heat of sublimation	λ_{sub}	$\lambda_{vap} + L_f$	$J\ kg^{-1}$
Thermal conductivity of water *	λ_{liq}	0.6	$W\ m^{-1}\ K^{-1}$
Thermal conductivity of ice*	λ_{ice}	2.29	$W\ m^{-1}\ K^{-1}$
Thermal conductivity of air*	λ_{air}	0.023	$W\ m^{-1}\ K^{-1}$
Radius of earth	R_e	6.37122×10^{6}	m

*Items are used in the Community Land Model only and are not shared among the other components. Table replicated from Table 1.4 in Oleson et al. (2004).

Appendix C

Atmospheric input to land model

Reference height	z_{atm}	m
Zonal wind at z_{atm}	u_{atm}	m s^{-1}
Meridional wind at z_{atm}	v_{atm}	m s^{-1}
Potential temperature	Θ_{atm}	K
Specific humidity at z_{atm}	q_{atm}	kg kg^{-1}
Pressure at z_{atm}	P_{atm}	Pa
Temperature at z_{atm}	T_{atm}	K
Incident longwave radiation	L_{atm}	W m^{-2}
Liquid precipitation	q_{rain}	mm s^{-1}
Solid precipitation	q_{sno}	mm s^{-1}
Incident direct beam visible solar radiation	$S_{atm}\downarrow_{vis}^{\mu}$	W m^{-2}
Incident direct beam near-infrared solar radiation	$S_{atm}\downarrow_{nir}^{\mu}$	W m^{-2}
Incident diffuse visible solar radiation	$S_{atm}\downarrow vis$	W m^{-2}
Incident diffuse near-infrared solar radiation	$S_{atm}\downarrow nir$	W m^{-2}

Table adapted from (Oleson et al., 2004). Reference heights for temperature, wind and specific humidity are required. Atmospheric model provides convective and large-scale liquid and solid precipitation, which are added to yield total liquid precipitation (q_{rain}) and solid precipitation (q_{sno}). Density of air (ρ_{atm}; kg m^{-3}) is also required; however, it is calculated directly from $\rho_{atm} = \frac{P_{atm} - 0.378\, e_{atm}}{R_{da} T_{atm}}$ where P_{atm} is atmospheric pressure (Pa), e_{atm} is atmospheric vapor pressure (Pa), Rda is the gas constant for dry air (J kg^{-1} K^{-1}), and T_{atm} is the atmospheric temperature (K). Atmospheric vapor pressure e_{atm} is derived from atmospheric specific humidity q_{atm} (kg kg^{-1}) as $e_{atm} = \frac{q_{atm} P_{atm}}{0.622 + 0.378 q_{atm}}$. The CO_2 and O_2 concentrations (Pa) are required but are calculated from prescribed partial pressures and the atmospheric pressure P_{atm} as ca = 355 $\times 10^{-6}$ P_{atm} as o_i = 0.209 P_{atm}.

Appendix D

Three dimensional primitive equations

Momentum equations:

$$\frac{\partial}{\partial t}u + \mathcal{L}(u) - \frac{uv\,tan\phi}{a} - fv = -\frac{1}{\rho_o a\cos\phi}\frac{\partial p}{\partial \lambda} + \mathcal{F}_{Hx}(u,v) + \mathcal{F}_V(u) \quad (1.1)$$

$$\frac{\partial}{\partial t}v + \mathcal{L}(v) - (u^2\tan\phi)/a + fu = -\frac{1}{\rho_o a}\frac{\partial p}{\partial \phi} + \mathcal{F}_{Hy}(u,v) + \mathcal{F}_V(v) \quad (1.2)$$

$$\mathcal{L}(\alpha) = \frac{1}{a\,\cos\phi}\left[\frac{\partial}{\partial\lambda}(u\alpha) + \frac{\partial}{\partial\phi}\,(\cos\phi)\;v\alpha\right] + \frac{\partial}{\partial z}(w\alpha) \quad (1.3)$$

$$\mathcal{F}_{Hx}(u,v) = A_M\left\{\nabla^2 u + \frac{u(1-tan^2\phi)}{a^2} - \frac{2sin\phi}{a^2cos^2\phi}\frac{\partial v}{\partial\lambda}\right\} \quad (1.4)$$

$$\mathcal{F}_{Hy}(u,v) = A_M\left\{\nabla^2 v + \frac{v(1-tan^2\phi)}{a^2} - \frac{2sin\phi}{a^2cos^2\phi}\frac{\partial u}{\partial\lambda}\right\} \quad (1.5)$$

$$\nabla^2\alpha = \frac{1}{a^2\,cos^2\,\phi}\frac{\partial^2\alpha}{\partial\lambda^2} + \frac{1}{a^2cos\phi}\frac{\partial}{\partial\phi}\left(cos\phi\frac{\partial\alpha}{\partial\phi}\right) \quad (1.6)$$

$$\mathcal{F}_V(\alpha) = \frac{\partial}{\partial z}\mu\frac{\partial}{\partial z}\alpha \quad (1.7)$$

Continuity equation:

$$\mathcal{L}(1) = 0 \quad (1.8)$$

Hydrostatic equation:

$$\frac{\partial p}{\partial z} = \rho g \quad (1.9)$$

Equation of state:

$$\rho = \rho(\Theta, S, p) \rightarrow \rho(\Theta, S, z) \quad (1.10)$$

Tracer transport:

$$\frac{\partial}{\partial t}\varphi + \mathcal{L}(\varphi) = \mathcal{D}_H(\varphi) + \mathcal{D}_V(\varphi) \quad (1.11)$$

$$\mathcal{D}_{\mathrm{II}}(\varphi) = A_{II}\nabla^2\varphi \quad (1.12)$$

$$\mathcal{D}_{\mathrm{V}}(\varphi) = \frac{\partial}{\partial z}\kappa\frac{\partial}{\partial z}\varphi\ ; \quad (1.13)$$

Where $\lambda, \phi, z = r - a$ are longitude, latitude, and depth relative to mean sea level $r = a$; g is the acceleration due to gravity, $f = 2\Omega sin\phi$ is the Coriolis parameter, and ρ_0 is the background density of seawater. Prognostic variables are the eastward and northward

velocity components (u, v), the vertical velocity ω, the pressure p, the density ρ, and the potential temperature Θ, and salinity S, as well as passive tracers, i.e., the idealized age tracer, and geochemical tracers described in the carbon cycle model (section 3.1.5). For 1.11, φ represents $\Theta, S,$ or a passive tracer. The pressure dependence of the equation of state is approximated to be a function of depth. A_H and A_M are the coefficients for horizontal diffusion and viscosity, respectively and are assumed spatially constant. κ and μ are the corresponding vertical mixing coefficients that typically depend on the local Richardson number (Pacanowski and Philander, 1981). The third terms on the left-hand side in equations 1.1 and 1.2 are metric terms due to the convective derivatives acting on the unit vectors in the λ, ϕ directions, the second and third terms in brackets in equations 1.4 and 1.5 ensure that no stresses are generated due to solid-body rotation (Williams, 1972). The forcing terms due to wind stress and heat, as well as fresh water fluxes, are applied as surface boundary conditions to the friction and diffusive terms $\mathcal{F}_V$ and $\mathcal{D}_V$. The bottom and lateral boundary conditions applied in POP are no-flux for tracers (zero tracer gradient normal to boundaries), and no-slip for velocities (both components are of velocity zero on bottom and lateral boundaries). The equations and definitions described above are from Smith and Gent (2004).

Appendix E

Genera by morphological grouping, adapted from Rees et al. (2002)

	Genus	Morphological group		Genus	Morphological group
1	*Cordaites*	Cordaite	36	*Baiera*	Ginkgophyte
2	*Crassinervia*	Cordaite	37	*Chiropteris*	Ginkgophyte
3	*Dorycordaites*	Cordaite	38	*Ginkgophyllum*	Ginkgophyte
4	*Glottophyllum*	Cordaite	39	*Glossopteris*	Ginkgophyte
5	*Lepeophyllum*	Cordaite	40	*Psygmophyllum*	Ginkgophyte
6	*Nephropsis*	Cordaite	41	*Rhipidopsis*	Ginkgophyte
7	*Noeggerathiopsis*	Cordaite	42	*Sphenobaiera*	Ginkgophyte
8	*Poacordaites*	Cordaite	43	*Gangamopteris*	Glossopterid
9	*Rufloria*	Cordaite	44	*Palaeovittaria*	Glossopterid
10	*Zamiopteris*	Cordaite	45	*Rhabdotaenia*	Glossopterid
11	*Nilssonia*	Cycadophyte	46	*Ribidgea*	Glossopterid
12	*Pseudoctenis*	Cycadophyte	47	*Vertebraria*	Glossopterid
13	*Pterophyllum*	Cycadophyte	48	*Gangamopteris*	Lycopsid
14	*Taeniopteris*	Cycadophyte	49	*Palaeovittaria*	Lycopsid
15	*Asterophyllites*	Fern	50	*Rhabdotaenia*	Lycopsid
16	*Cladophlebis*	Fern	51	*Ribidgea*	Lycopsid
17	*Danaeites*	Fern	52	*Vertebraria*	Lycopsid
18	*Dichotomopteris*	Fern	53	*Comia*	Peltasperm
19	*Fascipteris*	Fern	54	*Compsopteris*	Peltasperm
20	*Nemejcopteris*	Fern	55	*Dicroidium*	Peltasperm
21	*Neomariopteris*	Fern	56	*Lepidopteris*	Peltasperm
22	*Neoropteridium*	Fern	57	*Phylladoderma*	Peltasperm
23	*Oligocarpia*	Fern	58	*Buriadia*	Pinales
24	*Pecopteris*	Fern	59	*Culmitzschia*	Pinales
25	*Prynadeopteris*	Fern	60	*Ernestiodendron*	Pinales
26	*Todites*	Fern	61	*Gomphostrobus*	Pinales
27	*Botrychiopsis*	Fern 3	62	*Lebachia*	Pinales
28	*Plagiozamites*	Fern 3	63	*Paranocladus*	Pinales
29	*Sphenopteris*	Fern 3	64	*Walchia*	Pinales
30	*Tingia*	Fern 3	65	*Alethopteris*	Pteridosperm
31	*Cathaysiopteris*	Gigantopterid	66	*Angaropteridium*	Pteridosperm
32	*Emplectopteridium*	Gigantopterid	67	*Callipteridium*	Pteridosperm
33	*Emplectopteris*	Gigantopterid	68	*Callipteris*	Pteridosperm
34	*Gigantonoclea*	Gigantopterid	69	*Dicksonites*	Pteridosperm
35	*Gigantopterids*	Gigantopterid			

Table continued from previous page.

	Genus	Morphological group		*Genus*	Morphological group
70	*Linopteris*	Pteridosperm	77	*Annularia*	Sphenopsid
71	*Mixoneura*	Pteridosperm	78	*Annulina*	Sphenopsid
72	*Neoropteris*	Pteridosperm	79	*Asterotheca*	Sphenopsid
73	*Odontopteris*	Pteridosperm	80	*Calamites*	Sphenopsid
74	*Protoblechnum*	Pteridosperm	81	*Lobatannularia*	Sphenopsid
75	*Rhachiphyllym*	Pteridosperm	82	*Paracalamites*	Sphenopsid
76	*Sphenopteridium*	Pteridosperm	83	*Phylotheca*	Sphenopsid
			84	*Raniganjia*	Sphenopsid
			85	*Schizoneura*	Sphenopsid
			86	*Sphenophyllum*	Sphenopsid
			87	*Trizygia*	Sphenopsid

References

Algeo, T.J., Ellwood, B., Nguyen, T.K.T., Rowe, H., and Maynard, J.B., 2007, The Permian-Triassic boundary at Nhi Tao, Vietnam: Evidence for recurrent influx of sulfidic watermasses to a shallow-marine carbonate platform: Palaeogeography. Palaeoclimatology. Palaeoecology, v. 252, p. 304-327.

Algeo, T.J., Hinnov, L., Moser, J., Maynard, J.B., Elswick, E., Kuwahara, K., and Sano, H., 2010, Changes in productivity and redox conditions in the Panthalassic Ocean during the latest Permian: Geology, v. 38, no. 2, p. 187-190.

Algeo, T.J., Chen, Z.Q., Fraiser, M.L., and Twitchett, R.J., 2011, Terrestrial–marine teleconnections in the collapse and rebuilding of Early Triassic marine ecosystems: Palaeogeography, Palaeoclimatology, Palaeoecology, v. 308, no. 1-2, p. 1-11.

Anderson, L.A., and Sarmiento, J.L., 1994, Redfield ratios or remineralization determined by nutrient data analysis: Global Biogeochemical Cycles, v. 8, p. 65-80.

Anderson, R.Y., 2010, Earth as diode: monsoon source of the orbital 100 ka climate cycle: Climate of the Past Discussions, v. 6, p. 1421-1452.

Andreae, M.O., 1990, Ocean-atmosphere interactions in the global biogeochemical sulfur cycle: Marine Chemistry, v. 30, p. 1-29.

Antonov, J.I., Seidov, D., Boyer, T.P., et al., editors, 2010, World Ocean Atlas 2009, Volume 2: Salinity: Washington, D.C., U.S. Government Printing Office, 184 p.

Barron, e.J., and Fawcett, P.J., 1995, The climate of Pangea: a review of climate model simulations of the Permian. *in* Scholle, P.A., Peryt, T.M. and Ulmer-Scholle, D.S., eds., The Permian of Northern Pangea: Paleogeography, Paleoclijates, Stratigraphy: New York, I. Springer-Verlag, p.37-52.

Barry, R.G., and Chorley, R.J., 1982, Atmosphere, weather, and climate: London, Methuen, 407 p.

Basu, A.R., Petaev, M.I., Poreda, R.J., Jacobsen, S.B., and Becker, L., 2003, Chondritic meteorite fragments associated with the Permian-Triassic boundary in Antarctica: Science, v. 302, p. 1388-1392.

Battail, B., 2000, A comparison of Late Permian Gondwanan and Laurasian amniote faunas: Journal of African Earth Sciences, v. 31, no. 1, p. 165-174.

Battail, B., 1997, Les genres Dicynodon et Lystrosaurus (Therapsida, Dicynodontia) en Eurasie: Une mise au point: Geobios, v. 30, Supplement 1, no. 0, p. 39-48.

Baud, A., Cirilli, S., and Marcoux, J., 1997, Biotic response to mass extinction: The lowermost Triassic microbialites: Facies, v. 36, p. 238-242.

Becker, L., Poreda, R.J., Basu, A.R., Pope, K.O., Harrison, T.M., Nicholson, C., and Iasky, R., 2004, Bedout: a possible end-Permian impact crater offshore of Northwestern Australia: Science, v. 304, no. 5676, p. 1469-1477.

Berner, R.A., 2002, Examination of hypotheses for the Permo–Triassic boundary extinction by carbon cycle modeling: Proceedings of the National Academy of Sciences, v. 99, no. 7, p. 4172-4177.

Berner, R.A., and Barron, E.J., 1984, Comments on the BLAG model; Factors affecting atmospheric CO 2 and temperature over the past 100 million years: American Journal of Science, v. 284, no. 10, p. 1183-1192.

Bitz, C.M., and Lipscomb, W.H., 1999, An energy-conserving thermodynamic model of sea ice: Journal of Geophysical Research: Oceans, v. 104, no. C7, p. 15669-15677.

Black, B.A., Elkins-Tanton, L.T., Rowe, C.M., and Peate, I.U., 2012, Magnitude and consequence of volatile release from the Siberian Traps: Earth and Planetary Science Letters, v. 317-318, p. 363-373.

Boucot, A.J., Xu, C., and Scotese, C.R., 2013, Phanerozoic paleoclimate: An atlas of lithologic indicators of climate: Tulsa, OK, Society For Sedimentary Geology 11.

Boville, B.A., and Bretherton, C.S., 2003, Heating and kinetic energy dissipation in the NCAR Community Atmosphere Model: Journal of Climate, v. 16, no. 23, p. 3877.

Boville, B.A., Rasch, P.J., Hack, J.J., and McCaa, J.R., 2006, Representation of clouds and precipitation processes in the Community Atmosphere Model Version 3 (CAM3): Journal of Climate, v. 19, no. 11, p. 2184-2198.

Brandner, R., 1987, Ozeanographische und klimatische Veränderungen an der Perm-Trias-Grenze in der westlichen Tethys: Heidelberger Geowissenschaftliche Abhandlugen, v. 8, p. 44-45.

Breecker, D.O., Sharp, Z.D., and McFadden, L.D., 2010, Atmospheric CO_2 concentrations during ancient greenhouse climates were similar to those predicted

for A.D. 2100: Proceedings of the National Academy of Sciences, v. 107, no. 2, p. 576-580.

Briegleb, B.P., Bitz, C.M., Hunke, E.C., Lipscomb, W.H., Holland, M.M., Schramm, J.L., and Moritz, R.E., 2004, Scientific description of the sea ice component in the Community Climate System Model, Version 3: NCAR/TN-463+STR, 70 p.

Bryan, F.O., Danbasoglu, G., Nakashiki, N., Yoshida, Y., Kim, D.-., Tsutsui, J., and Doney, S.C., 2006, Response of the North Atlantic thermohaline circulation and ventilation to increasing carbon dioxide in CCSM3: Journal of Climate, v. 19, p. 2382-2397.

Caldeira, K., and Kasting, J.F., 1992, The life span of the biosphere revisited: Nature, v. 360, no. 6406, p. 721-723.

Campbell, I.H., Czamanske, G.K., Fedorenko, V.A., Hill, R.I., and Stepanov, V., 1992, Synchronism of the Siberian traps and the Permian-Triassic boundary: Science, v. 258, no. 5089, p. 1760-1763.

Cao, C., 2009, Biogeochemical evidence for euxinic oceans and ecological disturbance presaging the end-Permian mass extinction event: Earth and Planetary Science Letters, v. 281, no. 3-4, p. 188-201.

Castle, J.W., 2009, Hypothesis for the role of toxin producing algae in Phanerozoic mass extinctions based on evidence from the geologic record and modern environments: Environmental Geosciences, AAPG DEG, v. 16, no. 1, p. 1-22.

Charlson, R.J., Lovelock, J.E., Andreae, M.O., and Warren, S.G., 1987, Oceanic phytoplankton, atmospheric sulphur, cloud albedo and climate: Nature, v. 326, no. 16, p. 655-661.

Chumakov, N.M., and Zharkov, M.A., 2003, Climate during the Permian-Triassic biosphere reorganizations. Article 2. Climate of the Late Permian and Early Triassic: general inferences: Stratigraphy and Geological Correlation, v. 11, no. 4, p. 361-375.

Clapham, M.E., and Payne, J.L., 2011, Acidification, anoxia, and extinction: A multiple logistic regression analysis of extinction selectivity during the Middle and Late Permian: Geology, v. 39, no. 11, p. 1059-1062.

Collins, W.D., Bitz, C.M., Blackmon, M.L., et al., 2006, The Community Climate System Model Version 3 (CCSM3): Journal of Climate, v. 19, p. 2122-2143.

Collins, W.D., Bitz, C.M., Blackmon, M.L., et al., 2004, Description of the NCAR Community Atmosphere Model (CAM3): NCAR/TN-464+STR, 1 p.

Crowley, T.J., and North, G.R., 1991, Paleoclimatology: New York; Oxford England, Oxford University Press; Clarendon Press 18, 339 p.

Doney, S.C., Lindsay, K., Fung, I., and John, J., 2006, Variability in a stable, 1000-yr global coupled climate-carbon cycle simulation: Journal of Climate, v. 19, p. 3033-3054.

Dutton, J.F., and Barron, E.J., 1997, Miocene to present vegetation changes, a possible piece of the Cenozoic puzzle: Geology, v. 25, p. 39-41.

England, M.H., 1995, The age of water and ventilation timescales in a global ocean model: Journal of Physical Oceanography, v. 25, p. 2756-2777.

Erwin, D.H., 1993, The great Paleozoic crisis : life and death in the Permian: New York City, Columbia University Press, 327 p.

Erwin, D.H., 2006, Extinction: How life on Earth nearly ended 250 million years ago: Princeton, New Jersey, Princeton University Press, 296 p.

Erwin, D.H., 1994, The Permo-Triassic extinction: Nature, v. 367, p. 231-236.

Eyre, S.R., 1968, Vegetation and soils, a world picture: Chicago, Aldine Pub. Co., 324 p.

Flato, G., Marotzke, J., Abiodun, B., et al., 2013, Evaluation of climate models. *in* Stocker, T.F., Qin, D., Plattner, G.-., et al., eds., Climate change 2013: The physical science basis. Contribution of working group I to the fifth assessment report of the Intergovernmental Panel on Climate Change: Cambridge, United Kingdom and New York, NY, USA, Cambridge University Press, p.741-866.

Forsyth, D., and Uyeda, S., 1975, On the relative importance of the driving forces of plate motion: Geophysical Journal of the Royal Astronomical Society, v. 43, p. 163-200.

Fraiser, M.L., 2011, Paleoecology of secondary tierers from Western Pangean tropical marine environments during the aftermath of the end-Permian mass extinction: Palaeogeography Palaeoclimatology Palaeoecology, v. 208, p. 181-189.

Fraiser, M.L., Twitchett, R.J., Frederickson, J.A., Metcalfe, B., and Bottjer, D.J., 2011, Gastropod evidence against the Early Triassic Lilliput effect: COMMENT: Geology, v. 39, no. 1, p. e232-e232.

Garcia, H.E., Locarnini, R.A., Boyer, T.P., Antonov, J.I., Baranova, O.K., Zweng, M.M., and Johnson, D.R., 2010, World Ocean Atlas 2009, Volume 3: Dissolved oxygen, apparent oxygen utilization, and oxygen saturation: Washington, D.C., U.S. Government Printing Office, 344 p.

Gibbs, M.T., Rees, P.M., Kutzbach, J.E., Ziegler, A.M., Behling, P.J., and Rowley, D.B., 2002, Simulations of Permian climate and comparisons with climate-sensitive sediments: The Journal of Geology, v. 110, p. 33-55.

Gille, S.T., Metzger, E.J., and Tokmakian, R., 2004, Seafloor topography and ocean circulations. Oceanography: Oceanography, Special Issue--Bathymetry from Space, v. 17, no. 1, p. 47-54.

Glasspool, I.J., Hilton, J., Collinson, M.E., Wang, S., and Li-Cheng-Sen, 2004, Foliar physiognomy in Cathaysian gigantopterids and the potential to track Palaeozoic climates using an extinct plant group: Palaeogeography, Palaeoclimatology, Palaeoecology, v. 205, no. 1–2, p. 69-110.

Golonka, J., 2007, Phanerozoic paleoenvironment and paleolithofacies maps. Late Paleozoic: Geologia, v. 33, no. 2, p. 145-209.

Gorjan, P., Kaiho, K., Kakegawa, T., Niitsuma, S., Chen, Z.Q., Kajiwara, Y., and Nicora, A., 2007, Paleoredox, biotic and sulfur-isotopic changes associated with the end-

Permian mass extinction in the western Tethys: Chemical Geology, v. 244, no. 3–4, p. 483-492.

Grice, K., Cao, C., Love, G.D., et al., 2005, Photic zone euxinia during the Permian-Triassic superanoxic event: Science, v. 307, p. 706-709.

Grunt, T.A., 1995, Biogeography of Permian sea basins: Paleontologicheskii Zhurnal, v. 4, p. 10-25.

Grunt, T.A., and Shi, G.R., 1997, A hierarchical framework of Permian global marine biogeography: Proceeds from the 30th International Geological Congress, v. 12, p. 2-17.

Gulbranson, E.L., Isbell, J.L., Taylor, E.L., Ryberg, P.E., Taylor, T.N., and Flaig, P.P., 2012, Permian polar forests: deciduousness and environmental variation: Geobiology, v. 10, no. 6, p. 479-495.

Gulbranson, E.L., Ryberg, P.E., Decombeix, A., Taylor, E.L., Taylor, T.N., and Isbell, J.L., 2014, Leaf habit of Late Permian Glossopteris trees from high-palaeolatitude forests: Journal of the Geological Society, v. 171, no. 4, p. 493-507.

Helland-Hansen, B., 1916, Nogen hydrografiske metoder form: p. 357-359.

Horacek, M., Povoden, E., Richoz, S., and Brandner, R., 2010, High-resolution carbon isotope changes, litho- and magnetostratigraphy across Permian-Triassic Boundary sections in the Dolomites, N-Italy. New constraints for global correlation: Palaeogeography, Palaeoclimatology, Palaeoecology, v. 290, no. 1, p. 58-64.

Hotinski, R.M., Bice, K.L., Kump, L.R., Najjar, R.G., and Arthur, M.A., 2001, Ocean stagnation and end-Permian anoxia: Geology, v. 29, no. 1, p. 7-10.

Huang, C., Tong, J., Hinnov, L., and Chen, Z.Q., 2011, Did the great dying of life take 700 k.y.? Evidence from global astronomical correlation of the Permian-Triassic boundary interval: Geology, v. 39, p. 779-782.

Hudspith, V.A., Rimmer, S.M., and Belcher, C.M., 2014, Latest Permian chars may derive from wildfires, not coal combustion: Geology, v. 42, no. 10, p. 879-882.

Isozaki, Y., 1997, Permo-Triassic boundary superanoxia and stratified superocean: from lost deep sea: Science, v. 276, no. 5310, p. 235-238.

Jayne, S.R., St. Laurent, L.C., and Gille, S.T., 2003, Connections between ocean bottom topography and Earth's climate: Oceanography, Special Issue--Bathymetry from Space, v. 17, no. 1, p. 65-74.

Joachimski, M.M., Lai, X., Shen, S., et al., 2012, Climate warming in the latest Permian and the Permian–Triassic mass extinction: Geology, v. 40, no. 3, p. 195-198.

Kaiho, K., Kajiwara, Y., Chen, Z., and Gorjan, P., 2006, A sulfur isotope event at the end of the Permian,: Chemical Geology, v. 235, p. 33-47.

Kaiho, K., Kajiwara, Y., Nakano, T., et al., 2001, End-Permian catastrophe by a bolide impact: evidence of a gigantic release of sulfur from the mantle: Geology, v. 29, no. 9, p. 815-818.

Kajiwara, Y., 1994, Development of a largely anoxic stratified ocean and its temporary massive mixing at the Permian/Triassic boundary supported by the sulfur isotopic record: Palaeogeography, Palaeoclimatology, Palaeoecology, v. 111, no. 3-4, p. 367-379.

Kamo, S.L., Czamanske, G.K., Amelin, Y., Fedorenko, V.A., Davis, D.W., and Trofimov, V.R., 2003, Rapid eruption of Siberian flood-volcanic rocks and evidence for coincidence with the Permian–Triassic boundary and mass extinction at 251 Ma: Earth and Planetary Science Letters, v. 214, no. 1–2, p. 75-91.

Kanamitsu, M., Ebisuzaki, W., Woollen, J., Yang, S., Hnilo, J.J., Fiorino, M., and Potter, G.L., 2002, NCEP–DOE AMIP-II Reanalysis (R-2): Bulletin of the American Meteorological Society, v. 83, no. 11, p. 1631-1643.

Kato, Y., Nakao, K., and Isozaki, Y., 2002, Geochemistry of Late Permian to Early Triassic pelagic cherts from southwest Japan: implications for an oceanic redox change, v. 182, p. 15-34.

Katsman, C.A., 2006, Impacts of Localized Mixing and Topography on the Stationary Abyssal Circulation: Journal of Physical Oceanography, v. 36, p. 1660-1671.

Keeling, C.D., Piper, S.C., Bacastow, R.B., Wahlen, M., and Meijer, H.A., 2005, Atmospheric CO_2 and $^{13}CO_2$ exchange with the terrestrial biosphere and oceans from 1978 to 2000: Observations and carbon cycle implications. *in* Ehleringer, J.R., Cerling, T.E. and Dearing, M.D., eds., A history of atmospheric CO_2 and its effects on plants, animals, and ecosystems: New York, Springer Verlag 177, p.83-113.

Kidder, D.L., and Worsley, T.R., 2012, A human-induced hothouse climate?: GSA Today, v. 22, no. 2, p. 4-11.

Kidder, D.L., and Worsley, T.R., 2010, Phanerozoic large igneous provinces (LIPs), HEATT (haline euxinic acidic thermal transgression) episodes, and mass extinctions: Palaeogeography, Palaeoclimatology, Palaeoecology, v. 295, p. 162-191.

Kidder, D.L., and Worsley, T.R., 2004, Causes and consequences of extreme Permo-Triassic warming to globally equable climate and relation to the Permo-Triassic extinction and recovery: Palaeogeography Palaeoclimatology Palaeoecology, v. 203, p. 207-237.

Kiehl, J.T., 2007, Modeling the climates of the Late Paleozoic. *in* Williams, M., Haywood, A.M., Gregory, F.J. and Schmidt, D.N., eds., Deep-time perspectives on climate change: marrying the signal form computer models and biological proxies: MPG Books, Bodmin, UK, The Micropalaeontological Society, Special Editions, Geological Society of London, p.157-237.

Kiehl, J.T., and Dickinson, R.E., 1987, A study of the radiative effects of enhanced atmospheric CO_2 and CH_4 on early Earth surface temperatures: Journal of Geophysical Research: Atmospheres, v. 92, no. D3, p. 2991-2998.

Kiehl, J.T., and Shields, C.A., 2005, Climate simulation of the latest Permian: Implications for mass extinction: Geology, v. 33, no. 9, p. 757-760.

Knoll, A.H., Bambach, R.K., Canfield, D.E., and Grotzinger, J.P., 1996, Comparative Earth history and Late Permian mass extinction: Science, v. 273, no. 5274, p. 452-457.

Knoll, A.H., Bambach, R.K., Payne, J.L., Pruss, S., and Fischer, W.W., 2007, Paleophysiology and end-Permian mass extinction: Earth and Planetary Science Letters, v. 256, no. 3–4, p. 295-313.

Korte, C., and Kozur, H.W., 2010, Carbon-isotope stratigraphy across the Permian–Triassic boundary: A review: Journal of Asian Earth Sciences, v. 39, no. 4, p. 215-235.

Kozur, H., 1996, The conodonts *Hindeodus, Isarcicella* and *Sweetohindeodus* in the uppermost Permian and lowermost Triassic: Geologia Croatia, v. 49, no. 1, p. 81-115.

Kump, L.R., Pavlov, A., and Arthur, M.A., 2005, Massive release of hydrogen sulfide to the surface ocean and atmosphere during intervals of oceanic anoxia: Geology, v. 33, no. 5, p. 397-400.

Kump, L.R., and Pollard, D., 2008, Amplification of Cretaceous warmth by biological cloud feedbacks: Science, v. 320, p. 19.

Kutzbach, J.E., and Gallimore, R.G., 1989, Pangaean climates: megamonsoons of the megacontinent: Journal of Geophysical Research, v. 94, p. 3341-3358.

Kutzbach, J.E., Guetter, P.J., and Washington, W.M., 1990, Simulated circulation of an idealized ocean for Pangaean time: Paleoceanography, v. 5, p. 299-317.

Kutzbach, J.E., and Ziegler, A.M., 1993, Simulation of Late Permian climate and biomes with an atmosphere-ocean model: comparisons with observations: Philosophical Transactions: Biological Sciences, v. 341, no. 1297, p. 327-340.

Lai, X., 1998, A discussion on Permian-Triassic conodont studies: Albertiana, no. 20, p. 25-30.

Laskar, J., Robutel, P., Joutel, F., Gastineau, M., Correia, A.C.M., and Levrad, B., 2004, A long-term numerical solution for the insolation quantities of the Earth: Astronomy and Astrophysics, v. 428, no. 1, p. 261-285.

Lawver, L.A., and Scotese, C.R., 1987, A revised reconstruction of Gondwana, American Geophysical Union, 17 p.

Li, X., Taylor, G.T., Astor, Y., and Scranton, M.I., 2008, Relationship of sulfur speciation to hydrographic conditions and chemoautotrophic production in the Cariaco Basin: Marine Chemistry, v. 112, no. 1–2, p. 53-64.

Lin, S., 2004, A “vertically Lagrangian” finite-volume dynamical core for global models: Monthly Weather Review, v. 132, no. 10, p. 2293-2307.

Lin, S., and Rood, R.B., 1996, Multidimensional flux-form semi-Lagrangian transport schemes: Monthly Weather Review, v. 124, no. 9, p. 2046-2070.

Liu, Z., Notaro, M., Kutzbach, J., and Liu, N., 2006, Assessing global vegetation-climate feedbacks from observations: Journal of Climate, v. 19, no. 5, p. 787-814.

Locarnini, R.A., Mishonov, A.V., Antonov, J.I., et al., editors, 2010, World Ocean Atlas 2009, Volume 1: Temperature: Washington, D.C., U.S. Government Printing Office, 184 p.

Lottes, A.L., and Rowley, D.B., 1990, Reconstruction of the Laurasian and Gondwanan segments of Permian Pangea. *in* McKerrow, W.S. and Scotese, C.R., eds., Paleozoic paleogeography and biogeography: London, Geological Society of London Memoirs 12, p.383-395.

Lottes, A.L., and Ziegler, A.M., 1994, World peat occurrence and the seasonality of climate and vegetation: Palaeogeography, Palaeoclimatology, Palaeoecology, v. 106, no. 1-4, p. 23-37.

Manabe, S., and Stouffer, R.J., 1980, Sensitivity of a global climate model to an increase of CO2 concentration in the atmosphere: Journal of Geophysical Research: Oceans, v. 85, no. C10, p. 5529-5554.

Meehl, G.A., Arblaster, J.M., and Lawrence, D.M., 2006, Monsoon regimes in the CCSM3: Journal of Climate, v. 19, p. 2482-2494.

Meng, Q., and Zhang, G., 1999, Timing of collision of the North and South China blocks: Controversy and reconciliation: Geology, v. 27, no. 2, p. 123-126.

Meyen, S.V., 1987, Fundamentals of palaeobotany: London, Chapman & Hall, 432 p.

Meyer, K.M., Kump, L.R., and Ridgwell, A., 2008, Biogeochemical controls on photic-zone euxinia during the end-Permian mass extinction: Geology, v. 36, no. 9, p. 747-750.

Millero, F.J., 2006, Chemical oceanography: Boca Raton, FL, CRC Press, 496 p.

Montañez, I.P., Tabor, N.J., Niemeier, D., et al., 2007, CO2-forced climate and vegetation instability during Late Paleozoic deglaciation: Science (New York, N.Y.), v. 315, no. 5808, p. 87-91.

Montenegro, A., Spence, P., Meissner, K.J., Eby, M., Melchin, M.J., and Johnston, S.T., 2011, Climate simulations of the Permian-Triassic boundary: Ocean acidification and the extinction event: Paleoceanography, v. 26, no. 3207, p. 1-19.

Najjar, R., and Orr, J., 1998, Design of OCMIP-2 simulations of chlorofluorocarbons, the solubility pump and common biogeochemistry: http://www.ipsl.jussieu.fr/OCMIP/phase2/simulations/design.ps (3/18 2011).

Najjar, R.G., Jin, X., Louanchi, F., et al., 2007, Impact of circulation on export production, dissolved organic matter and dissolved oxygen in the ocean: Results from Phase II of the Ocean Carbon-cycle Model Intercomparison Project (OCMIP-2): Global Biogeochemical Cycles, v. 21, p. 1-22.

Najjar, R.G., and Orr, J.C., 1999, Biotic-HOWTO: http://www.ipsl.jussieu.fr/OCMIP/ (3/18 2011).

National Research Council, 2011, Understanding Earth's deep past: Lessons for our climate future: Washington DC, The National Academies Press, 212 p.

Newton, R.J., Pevitt, E.L., Wignall, P.B., and Bottrell, S.H., 2004, Large shifts in the isotopic composition of seawater sulphate across the Permo-Triassic boundary in northern Italy: Earth and Planetary Science Letters, v. 218, p. 331-345.

Nie, S., Rowley, D.B., and Ziegler, A.M., 1990, Constraints on the locations of Asian microcontinents in Palaeo-Tethys during the Late Palaeozoic: Geological Society, London, Memoirs, v. 12, no. 1, p. 397-409.

Oleson, K.W., Bitz, C.M., Blackmon, M.L., et al., 2004, Technical description of the Community Land Model (CLM): NCAR/TN-461+STR, 1 p.

Osen, A.K., Winguth, A.M.E., Winguth, C., and Scotese, C.R., 2013, Sensitivity of Late Permian climate to bathymetric features and implications for the mass extinction: Global and Planetary Change, v. 105, p. 171-179.

Otto-Bliesner, B., and Upchurch, G.R., 1997, Vegetation-induced warming of high-latitude regions during the Late Cretaceous period: Nature, v. 385, no. 6619, p. 804-807.

Pacanowski, R.C., and Philander, S.G.H., 1981, Parameterization of vertical mixing in numerical models of the tropical oceans: Journal of Physical Oceanography, v. 11, p. 1443-1451.

Parrish, J.T., 1993, Climate of the supercontinent Pangea: Journal of Geology, v. 101, p. 215-233.

Payne, J.L., Lehrmann, D.J., Wei, J., and Knoll, A.H., 2006, The Pattern and Timing of Biotic Recovery from the End-Permian Extinction on the Great Bank of Guizhou, Guizhou Province, China: Palaios, v. 21, no. 1, p. 63-85.

Payne, J.L., Lehrmann, D.J., Follett, D., et al., 2007, Erosional truncation of uppermost Permian shallow-marine carbonates and implications of Permian-Triassic boundary events: GSA Bulletin, v. 119, no. 7/8, p. 771-784.

Payne, J.L., and Clapham, M.E., 2012, End-Permian mass extinction in the oceans: An ancient analog for the twenty-first century?: Annual Review of Earth and Planetary Sciences, v. 40, no. 1, p. 89-111.

Rampino, M.R., Prokoph, A., and Adler, A., 2000, Tempo of the end-Permian event: High-resolution cyclostratigraphy at the Permian-Triassic boundary: Geology, v. 28, no. 7, p. 643-646.

Raven, P.H., 1973, The evolution of Mediterranean floras. *in* Di Castri, F. and Mooney, H.A., eds., Mediterranean Type Ecosystems. Ecological Studies: New York, Springer-Verlag 7, p.213-224.

Rees, A.M., Sims, H.J., Stein, B.E., et al., 2014, Taxonomic occurrences recorded in Fossilworks, the evolution of terrestrial ecosystems database, the Paleobiology Database, and the Paleogeographic Atlas Project database, DB Paleobiology Database, http://paleodb.org.

Rees, P.M., Gibbs, M.T., Ziegler, A.M., Kutzbach, J.E., and Behling, P.J., 1999, Permian climates: Evaluating model predictions using global paleobotanical data: Geology, v. 27, no. 10, p. 891-894.

Rees, P.M., Ziegler, A.M., Gibbs, M.T., Kutzbach, J.E., Behling, P.J., and Rowley, D.B., 2002, Permian Phytogeographic Patterns and Climate Data/Model Comparisons: Journal of Geology, v. 110, no. 1, p. 827-830.

Reichow, M.K., Pringle, M.S., Al'Mukhamedov, A.I., et al., 2009, The time and extent of the eruption of the Siberial Traps large igneous provice: Implications for the end-Permian environmental crisis: Earth and Planetary Science Letters, v. 277, p. 9-20.

Reichow, M.K., Saunders, A.D., White, R.V., Pringle, M.S., Al'Mukhamedov, A.I., Medvedev, A.I., and Kirda, N.P., 2002, 40Ar/39Ar dates from the west Siberian basin: Siberian flood basalt province doubled: Science, v. 296, no. 5574, p. 1846-1849.

Renne, P.R., and Basu, A.R., 1991, Rapid eruption of the Siberian traps flood basalts at the Permo-Triassic boundary: Science, v. 253, no. 5016, p. 176-179.

Renne, P.R., Black, M.T., Zichao, Z., Richards, M.A., and Basu, A.R., 1995, Synchrony and causal relations between Permian-Triassic boundary crises and Siberian flood volcanism: Science (New York, N.Y.), v. 269, no. 5229, p. 1413-1416.

Retallack, G.J., Sheldon, N.D., Carr, P.F., et al., 2011, Multiple Early Triassic greenhouse crises impeded recovery from late Permian mass extinction: Palaeogeography, Palaeoclimatology, Palaeoecology, v. 308, p. 233-251.

Retallack, G.J., 1995, Permian-Triassic life crisis on land: Science, v. 267, p. 77-80.

Riccardi, A.L., Arthur, M.A., and Kump, L.R., 2006, Sulfur isotopic evidence for chemocline upward excursions during the end-Permian mass extinction: Geochimica et Cosmochimica Acta, v. 70, no. 23, p. 5740-5752.

Roscher, M., Stordal, F., and Svensen, H., 2011, The effect of global warming and global cooling on the distribution of the latest Permian climate zones: Palaeogeography, Palaeoclimatology, Palaeoecology, v. 309, no. 3–4, p. 186-200.

Royer, D.L., 2006, CO_2-forced climate thresholds during the Phanerozoic: Geochimica et Cosmochimica Acta, v. 70, p. 5665-5675.

Schramm, J.L., Bitz, C.M., Briegleb, B.P., Holland, M.M., Hunke, E.C., Lipscomb, W.H., and Moritz, D., 2004, Community Sea Ice Model (CSIM) user's guide version 5.0: Boulder, CO, National Center for Atmospheric Research, 184 p.

Schubert, J.K., and Bottjer, D.J., 1995, Aftermath of the Permian-Triassic mass extinction event: Paleoecology of Lower Triassic carbonates in the western USA: PALAEO, v. 116, p. 1-39.

Scotese, C.R., 2014. Atlas of Permo-Triassic paleogeographic maps, (mollweide projection), PALEOMAP Atlas for ArcGIS, v. 3-4, PALEOMAP Project, Evanston, IL.

Scotese, C.R., and Langford, R.P., 1995, Pangea and the paleogeography of the Permian. *in* Scholle, P.A., Peryt, T.M. and Ulmer-Scholle, D.S., eds., The Permian of Northern Pangea, volume 1, Paleogeography, Paleoclimates, and Stratigraphy: Berlin, Springer, p.3-19.

Scotese, C.R., and Rowley, D.B., 1985, The orthoganality of subduction: an empirical rule?: Tectonophysics, v. 116, p. 173-187.

Semtner, A.J., 1986, Finite-difference formulation of a world ocean model. *in* O'Brien, J., ed., Advanced Physical Oceanographic Numerical Modelling: Netherlands, Springer 186, p.187-202.

Şengör, A.M.C., and Atayman, S., 2009, The Permian Extinction and the Tethys: An exercise in global geology: Geological Society of America Special Papers, v. 448, p. 1-85.

Şengör, A.M.C., and Natal'in, B.A., 1996, Palaeotectonics of Asia: Fragments of a synthesis. *in* Yin, A. and Harrison, M., eds., The tectonic evolution of Asia, Rubey Colloquium: Cambridge, Cambridge University Press, p.486-640.

Smith, A.G., and Hallam, A., 1970, The fit of the southern continents: Nature (London), v. 225, p. 139-144.

Smith, R., and Gent, P., 2004, Reference manual for the Parallel Ocean Program (POP) ocean component of the Community Climate System Model (CCSM2.0 and 3.0), Los Alamos National Laboratory and National Center for Atmospheric Research, 75 p.

Smith, R., Jones, P., Briegleb, B., et al., 2010, The Parallel Ocean Program (POP) reference manual: Ocean component of the Community Climate System Model (CCSM) and Community Earth System Model (CESM): Boulder, CO, University Corporation for Atmospheric Research, 140 p.

Solomon, S., Qin, D., and Manning, M., 2007, Technical Summary. *in* Boonpragob, K., Giorgi, F. and Jallow, B.P., eds., Climate Change 2007: The physical science basis:

contribution of Working Group I to the Fourth Assessment Report of the Intergovernmental Panel on Climate Change: New York, Cambridge University Press, p.19-91.

St. Laurent, L., and Garrett, C., 2002, The role of internal tides in mixing the deep ocean: Journal of Physical Oceanography, v. 32, p. 2882-2899.

Stein, C.A., and Stein, S., 1992, A model for the global variation in oceanic depth and heat flow with lithospheric age: Nature, v. 359, p. 123-129.

Sun, Y., Joachimski, M.M., Wignall, P.B., et al., 2012, Lethally hot temperatures during the Early Triassic Greenhouse: Science, v. 338, p. 366-370.

Svensen, H., Planke, S., Plozov, A.G., Schmidbauer, N., Corfu, F., Podladchikov, Y.Y., and Jamtveit, B., 2009, Siberia gas venting and the end-Permian environmental crisis: Earth and Planetary Science Letters, v. 277, p. 490-500.

Tabor, N.J., and Poulsen, C.J., 2008, Palaeoclimate across the Late Pennsylvanian–Early Permian tropical palaeolatitudes: A review of climate indicators, their distribution, and relation to palaeophysiographic climate factors: Palaeogeography, Palaeoclimatology, Palaeoecology, v. 268, no. 3–4, p. 293-310.

Taylor, T.N., and Taylor, E.L., 1993, The biology and evolution of fossil plants: Englewood Cliffs, N.J., Prentice-Hall, 982 p.

Thiele, G., and Sarmiento, J., 1990, Tracer dating and ocean ventilation: Journal of Geophysical Research, v. 95, p. 9377-9391.

Thurnherr, A.M., Ledwell, J.R., Lavelle, J.W., and Mullineaux, L.S., 2011, Topography and circulation near the crest of the East Pacific Rise between 9º and 10ºN: Deep-Sea Research, v. 58, p. 365-376.

Tohver, E., Lana, C., Cawood, P.A., et al., 2012, Geochronological constraints on the age of a Permo-Triassic impact event: U-Pb and $^{40}Ar/^{39}Ar$ results for the 40km Araguainha structure of central Brazil: Geochimica et Cosmochimica Acta, v. 86, p. 214-227.

Twitchett, R.J., 1999, Palaeoenvironments and faunal recovery after the end-Permian mass extinction: Palaeogeography, Palaeoclimatology, Palaeoecology, v. 154, no. 1–2, p. 27-37.

Twitchett, R.J., 2007, The Lilliput effect in the aftermath of the end-Permian extinction event: Palaeogeography, Palaeoclimatology, Palaeoecology, v. 252, p. 132-144.

Twitchett, R.J., Looy, C.V., Morante, R., Visscher, H., and Wignall, P.B., 2001, Rapid and synchronous collapse of marine and terrestrial ecosystems during the end-Permian biotic crisis: Geology, v. 29, no. 4, p. 351-354.

Tyson, R.V., and Pearson, T.H., 1991, Modern and ancient continental shelf anoxia: an overview, v. 58, p. 1-24.

Urbanek, A., 1993, Biotic crises in the history of Upper Silurian graptoloids: A paleobiological model: Historical Biology, v. 7, p. 29-50.

Vaughan, A.P.M., 2007, Climate and geology – a Phanerozoic perspective. *in* Williams, M., Haywood, A.M., Gregory, F.J. and Schmidt, D.N., eds., Deep-time perspectives

on climate change: marrying the signal from computer models and biological proxies: London, Geological Society of London, p.5-59.

Vertenstein, M., Craig, T., Henderson, T., Murphy, S., Carr, G.R., and Norton, N., 2004, CCSM3.0 User's Guide, 69 p.

Visscher, H., Looy, C.V., Collinson, M.E., Brinkhuis, H., van Konijnenburg-van Cittert, J.H.A., Kürschner, W.M., and Sephton, M.A., 2004, Environmental mutagenesis during the end-Permian ecological crisis: Proceedings of the National Academy of Sciences of the United States of America, v. 101, no. 35, p. 12952-12956.

Walter, H., 1985, Vegetation of the Earth and ecological systems of the geo-biosphere: Berlin, Springer-Verlag, 318 p.

Walter, H., and Breckle, S.W., 2002, Walter's vegetation of the earth: the ecological systems of the geo-biosphere: Berlin; New York, Springer, 527 p.

Wang, K., Geldsetzer, H.H.J., and Krouse, H.R., 1994, Permian-Triassic extinction: Organic {delta}13C evidence from British Columbia, Canada: Geology, v. 22, no. 7, p. 580.

Wang, R., Zhang, S., Brassell, S., et al., 2012, Molecular carbon isotope variations in core samples taken at the Permian–Triassic boundary layers in southern China: International Journal of Earth Sciences, v. 101, no. 5, p. 1397-1406.

Wanninkhof, R., 1992, Relationship between wind speed and gas exchange over the ocean: Geophysical Research, v. 97, p. 7373-7382.

Wignall, P.B., 2001, Large igneous provinces and mass extinctions: Earth-Science Review, v. 53, p. 1-33.

Wignall, P.B., and Hallam, A., 1992, Anoxia as a cause of the Permian/Triassic extinction: Facies evidence from northern Italy and the western United States: Palaeogeography, Palaeoclimatology, Palaeoecology, v. 93, p. 21-460.

Wignall, P.B., and Twitchett, R.J., 1996, Ocean anoxia and the end Permian mass extinction: Science, New Series, v. 272, no. 5265, p. 1155-1158.

Wignall, P.B., Bond, D.P.G., Kuwahara, K., Kakuwa, Y., Newton, R.J., and Poulton, S.W., 2010, An 80 million year oceanic redox history from Permian to Jurassic pelagic sediments of the Mino-Tamba terrane, SW Japan, and the origin of four mass extinctions, v. 71, p. 109-123.

Wignall, P.B., and Newton, R., 2003, Contrasting deep-water records from the Upper Permian and Lower Triassic of South Tibet and British Columbia: Evidence for a diachronous mass extinction: Palaios, v. 18, no. 2, p. 153-167.

Williams, G.P., 1972, Friction term formulations and convective instability in a shallow atmosphere: Journal of the Atmospheric Sciences, v. 29, p. 870-876.

Winguth, A., and Winguth, C., 2013, Precession-driven monsoon variability at the Permian-Triassic boundary--Implications for anoxia and the mass extinction: Global and Planetary Change, v. 105, p. 160-170.

Winguth, A.M.E., Heinze, C., Kutzbach, J.E., et al., 2002, Simulated warm polar currents during the Middle Permian: Paleoceanography, v. 17, no. 4, p. 9:1-9:18.

Winguth, A.M.E., and Maier-Reimer, E., 2005, Causes of marine productivity and oxygen changes associated with the Permian-Triassic boundary: A reevaluation with ocean general circulation models: Marine Geology, v. 217, p. 283-304.

Winguth, A.M.E., Osen, A.K., Shields, C.A., and Winguth, C., 2012, Hothouse climate at the End-Permian and implications for future climate change and mass extinction, *in* : Charlotte, N.C., Geological Society of America, p. 63.

Winguth, C., and Winguth, A.M.E., 2012, Simulating Permian–Triassic oceanic anoxia distribution: Implications for species extinction and recovery: Geology, v. 40, no. 2, p. 127-130.

Yang, H., Chen, Z.Q., Wang, Y., Tong, J., Song, H., and Chen, J., 2011, Composition and structure of microbialite ecosystems following the end-Permian mass extinction in South China: Palaeogeography, Palaeoclimatology, Palaeoecology, v. 308, no. 1-2, p. 111-128.

Yeager, S.G., Shields, C.A., Large, W.G., and Hack, J.J., 2006, The low-resolution CCSM3: Journal of Climate, v. 19, p. 2545-2566.

Yin, H., Tong, J., and Zhang, K., 2005, A Review on the Global Stratotype Section and Point of the Permian-Triassic Boundary: Acta Geologica Sinica - English Edition, v. 79, no. 6, p. 715-728.

Yin, H., Zhang, K., Tong, J., Yang, Z., and Wu, S., 2001, The Global Stratotype Section and Point (GSSP) of the Permian-Triassic Boundary: Episodes, v. 24, no. 2, p. 102-114.

Zhang, G.J., and McFarlane, N.A., 1995, Sensitivity of climate simulations to the parameterization of cumulus convection in the Canadian Climate Centre general ciruculation model: Atmosphere-Ocean, v. 33, p. 407-446.

Zhang, R., Follows, M.J., Grotzinger, J.P., and Marshall, J., 2001, Could the Late Permian deep ocean have been anoxic?: Paleoceanography, v. 16, no. 3, p. 317-329.

Zhang, X., He, J., Zhang, J., Polyakov, I., Gerdes, R., Inoue, J., and Wu, P., 2013, Enhanced poleward moisture transport and amplified northern high-latitude wetting trend, v. 3, no. 1, p. 47-51.

Zhao, X., Coe, R.S., Gilder, S.A., and Frost, G.M., 1996, Palaeomagnetic constraints on the palaeogeography of China: Implications for Gondwanaland: Australian Journal of Earth Sciences, v. 43, no. 6, p. 643-772.

Ziegler, A.M., 1990, Pytogeographic patterns and continental configurations during the Permian Period. *in* McKerrow, W.S. and Scotese, C.R., eds., Palaeozoic Palaeogeography and Biogeography: Bath, UK, Geological Society of London 12, p.363-379.

Ziegler, A.M., Gibbs, M.T., and Hulver, M.L., 1998, Mini-atlas of oceanic water masses in the Permian period: Proceedings of the Royal Society of Victoria, v. 110, no. 1/2, p. 323-343.

Ziegler, A.M., Hulver, M.L., and Rowley, D.B., 1997, Permian world topography and climate. *in* Martini, I.P., ed., Late glacial and postglacial environmental changes:

Quaternary, Carboniferous-Permian and Proterozoic: Oxford, Oxford University Press, p.111-146.

Ziegler, A.M., Raymond, A.L., Gierlowski, T.C., Horrell, M.A., Rowley, D.B., and Lottes, A.L., 1987, Coal, climate and terrestrial productivity: the present and early Cretaceous compared: Geological Society of London, Special Publications, v. 32, no. 1, p. 25-49.

Ziegler, A.M., Eshel, G., Rees, P.M., Rothfus, T.A., Rowley, D.B., and Sunderlin, D., 2003, Tracing the tropics across land and sea: Permian to present: Lethaia, v. 36, no. 3, p. 227.

Biographical Information

Angela Osen graduated Magna Cum Laude from the University of Texas at Arlington with a major in Geology and a minor in Biology. Motivated by her undergraduate research experience supported by Professor Arne Winguth and NSF grant EAR 0745817, she has persued her Ph.D. studies in paleoclimate and climate modeling. She has received several honors and scholarships including the Outstanding Mineralogy Student Award, Don Reaser Field Camp Scholarship, LSAMP Bridge to Doctorate Fellowship, and numerous travel grants. While attending UTA, Angela has served as Vice President of Sigma Gamma Epsion (National Honor Society for Earth Sciences) student chapter, as well as Treasurer and Social Media coordinator for the student chapter of the American Association of Petroleum Geologists (AAPG). Angela is currently an active member of the Geological Society of America, the American Geophysical Union, Phi Kappa Phi, and is also a crew member of the Arlington Archosaur Site. After receiving her Ph.D. in December of 2014, Angela intends on continuing her research and strives to teach in a university setting